Unravelling the role of RIM proteins in synaptic transmission: RIM1α tunes Ca^{2+} channel subtype contribution to neurotransmitter release

Dissertation

zur Erlangung des Doktorgrades (PhD)

der Medizinischen Fakultät

der Rheinischen Friedrich-Wilhelms-Universität

Bonn

Sara Ferrando Colomer

aus Canals, Spanien

2019

Angefertigt mit der Genehmigung

der Medizinischen Fakultät der Universität Bonn

1. Gutachter: Prof. Dr. med. Dirk Dietrich
2. Gutachter: Prof. Dr. María Luz Montesinos Gutiérrez

Tag der Mündlichen Prüfung: 12. April 2019

Aus der Klinik und Poliklinik für Neurochirurgie

Direktor: Prof. Dr. med. Hartmut Vatter

To the people who I loved, love and will love

INDEX

List of abbreviations

Agatx	ω-agatoxin IVA
AM	acetoxymethyl
AMPAR	AMPA receptor
AP	action potential
AZ	active zone
$[Ca^{2+}]_e$	extracellular Ca^{2+} concentration
$[Ca^{2+}]_i$	intracellular Ca^{2+} concentration
CCD	charge-coupled device
cDKO	conditional double knockout
Cdk5	cyclin-dependent kinase 5
Cgtx	ω-conotoxin GVIA
CNQX	6-cyano-7-nitroquinoxaline-2,3-dione
CNS	central nervous system
D-APV	D-2-amino-5-phosphonopentanoic acid
ΔF	peak fluorescence
DIV	day in vitro
DMSO	dimethyl sulfoxide
DG	dentate gyrus
EC	entorhinal cortex
EPP	end-plate potential
EPSC	excitatory postsynaptic current
F	fluorescence
fEPSP	field excitatory postsynaptic potential
HBC	2-hydroxypropyl-β-cylcodextrin
HEPES ACSF	HEPES-buffered artificial cerebrospinal fluid
HVA	high-voltage activated
i_{Ca}	individual Ca^{2+} channel current

I_{Ca}	total Ca^{2+} entry
IEI	inter-event interval
IPSC	inhibitory postsynaptic current
KO	knockout
LTP	long-term plasticity
LVA	low-voltage activated
m	quantal content
mACSF	modified artificial cerebrospinal fluid
mEPSC	miniature excitatory postsynaptic current
mIPSC	miniature inhibitory postsynaptic current
mPSP	miniature postsynaptic potential
n	number of releasable vesicles
NMDAR	NMDA receptor
NMJ	neuromuscular junction
pEPSP	population excitatory postsynaptic potential
PPF	paired-pulse facilitation
P_r	synaptic release probability
PSP	postsynaptic potential
pSpike	population spike
P_{ves}	vesicular release probability
q	quantal amplitude or quantal size
R_a	access resistance
RIM	Rab3-interacting molecule
RIM-BP	RIM-binding protein
RRP	readily-releasable pool
sACSF	standard artificial cerebrospinal fluid
Sc-CA1	Schaffer collaterals to CA1 synapses
SD	standard deviation
STP	short-term plasticity
SV	synaptic vesicle
Syt1	Synaptotagmin-1
Syt7	Synaptotagmin-7

τ	time constant of decay
TTX	tetrodotoxin
VGCC	voltage-gated Ca^{2+} channel
WT	wild-type
4-AP	4-Aminopyridine

1 Introduction

1.1 Synaptic computation

Hypothesized by Santiago Ramón y Cajal in 1888 (Ramón y Cajal, 1888) and confirmed in the 1950s with the development of the electron microscope (Palay and Palade, 1955), it is established that neurons are individual entities creating the complexity of the brain. In the nervous system, neurons communicate to each other via synapses. Two main modalities of neural communication co-exist: electrical and chemical. Electrical synapses are direct connections between neural cells by gap junctions, whereas chemical synapses convey information between two adjacent neurons by the release of chemicals, called neurotransmitters. Electrical synapses, also called gap junctions, are important for glial cells communication as well as synchronization and rhythmicity in neural circuits. Nevertheless, the most prominent route of communication between neurons is chemical synaptic transmission.

In a typical chemical synapse, synaptic transmission implies the transmission of information from the presynaptic neuron to the postsynaptic cell, through the synaptic cleft (Figure 1.1). Briefly, chemical synaptic transmission can be explained in five steps:

1. An action potential (AP) in the presynaptic neuron reaches the axon terminal.
2. At the presynaptic nerve terminal, voltage-gated Ca^{2+} channels (VGCC) open.
3. Ca^{2+} binds to Ca^{2+} sensors located at the synaptic vesicles (SV). The SVs, which contain neurotransmitter molecules, fuse with the plasma membrane, releasing the chemicals.
4. Those neurotransmitters bind to specific receptors located at the postsynaptic cell.
5. The binding to the receptors opens ion channels causing the postsynaptic potential.

The ability of a synapse in generating the postsynaptic potential is called synaptic strength. Synapses are able to constantly tune the synaptic strength. They are dynamic computational devices that not only transmit AP-encoded information, but also transform the information encoded by the presynaptic neurons into different and adaptable patterns of neurotransmitter release (Liaw and Berger, 1996). The ability to process and integrate information and consequently modify synaptic strength, is known as synaptic plasticity. Synaptic plasticity can occur either following the basic flow of synaptic transmission, i.e. feedforward, or in a feedback manner, from the postsynaptic cell to the presynaptic neuron.

The feedforward synaptic plasticity is a particularly interesting form of plasticity as its induction depends exclusively on the presynaptic activity, thus representing the purest form of presynaptic computation, without postsynaptic influence. It has been shown that the presynaptic Rab3-interacting molecule (RIM) proteins are involved in this type of synaptic plasticity. At the presynaptic nerve terminal, synaptic strength is modified by rearrangements in the functional state of the active zone (AZ), a specialized area of the plasma membrane responsible for the Ca^{2+}-dependent neurotransmitter release. Every neuron at each of its presynaptic terminals can modified the temporal pattern of train of APs depending on the context of presynaptic activity, which directly influences the probability of transmitter release. Modifications of the presynaptic release probability tune the synaptic strength during feedforward plasticity.

The predominance of chemical synaptic transmission together with the fact that one single neuron shows specific synapse dynamics across its up to thousands of axon terminals, provide the neural networks with an enormous computational power (Abbott and Regehr, 2004). This great flexibility at synaptic level is the backbone of learning and memory (Mayford et al., 2012).

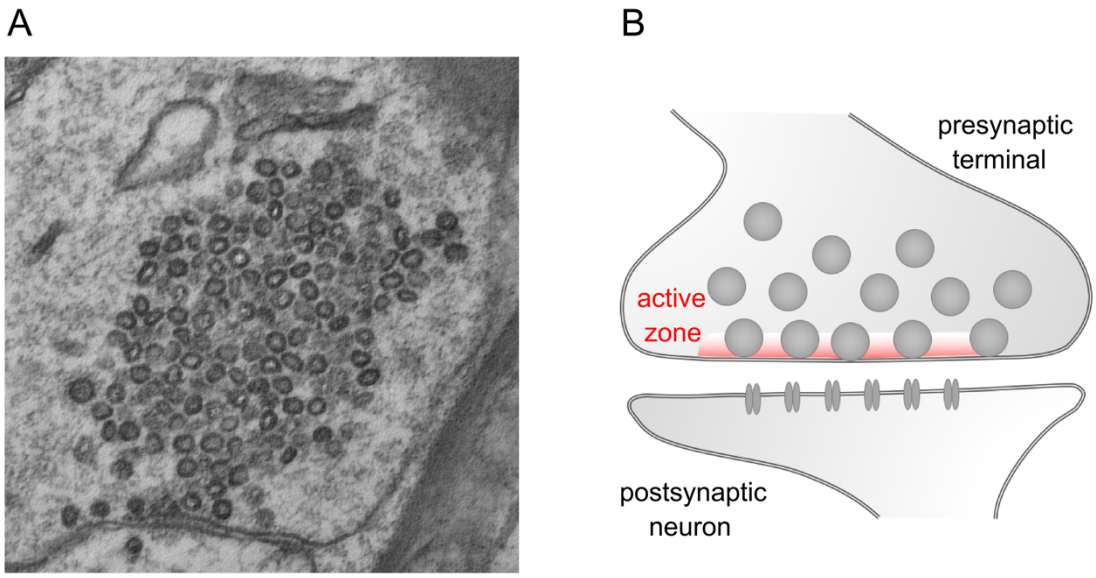

Figure 1.1 Structure of a chemical synapse. (A) Electron micrograph of a presynaptic terminal onto a postsynaptic neuron (Milovanovic and De Camilli, 2017). (B) Schematic drawing of a synapse illustrating the presynaptic neuron, the active zone, specialized area of the plasma membrane responsible for synaptic vesicle exocytosis, and the postsynaptic cell.

1.2 Presynaptic mechanisms of synaptic transmission

Based on the modernist principle of “form follows function”, which states that the shape of an object relates to its purpose, we study the functional aspects of synaptic transmission first, focusing on the physiology of neurotransmitter release and later, exploring the structure of the AZ in detail.

Speed, efficiency, and flexibility are hallmarks of synaptic transmission. Those characteristics are, in part, due to the high degree of temporal and spatial coordination of Ca^{2+}-triggering SV exocytosis at the presynaptic terminal.

1.2.1 Quantal nature of synaptic transmission

Studying neurotransmitter release at the neuromuscular junction (NMJ) of frogs, Bernard Katz and his collaborators proposed the fundamental quantal nature of chemical synaptic transmission (Castillo and Katz, 1954). This theory states that postsynaptic potentials (PSP) are built from the presynaptic exocytosis of one vesicle or an integral number of SVs. The postsynaptic potential originated in response to

the release of neurotransmitters from a single vesicle is called miniature PSP (mPSP). In the absence of an AP, Katz and colleagues observed the smallest postsynaptic signal possible and concluded that it was due to the release of the cargo of one single vesicle. Consequently, one SV was defined as one quantum and the postsynaptic response to the release of a quantum the so-called quantal amplitude or quantal size (*q*).

In contrast to the spontaneous and random release of individual quanta, an AP mediates the simultaneous release of several quanta. This is called fast, synchronous, or evoked vesicle release. Shortly after an AP, there is a transient increase in the release probability for each quantum, triggering the release of several SVs at the same time. The average number of vesicles released after an AP is named the quantal content (*m*). As described in Katz's quantal model, *m* depends on the release probability of each individual vesicle, known as vesicular release probability (P_{ves}), and the number of releasable vesicles (*n*).

$$m = P_{ves} * n \quad (1)$$

Therefore, the probability of *n* quanta being released after an AP is given by a binomial distribution and can be expressed as the synaptic release probability (P_r). During spontaneous release, when P_{ves} is extremely low, neurotransmitter release is described by a Poisson distribution, signifying the underlying random processes; in other words, the release of one SV is independent of the time since the last vesicle release.

Applying quantal analysis to the study of the central nervous system (CNS) synapses is delicate. Initially, Katz defined the parameter *n* as the number of fusion competent vesicles, assuming that one release site, being this a presynaptic bouton or an AZ, contains only a single SV. It was thought that release caused by a single presynaptic AP was limited to one vesicle, phenomenon known as univesicular release. Nevertheless, recently it has been shown that at certain central synapses, such as the hippocampal Schaffer collaterals, several vesicles per AZ are ready to be released after an AP, known as multivesicular release (Christie and Jahr, 2006, Ricci-Tersenghi et al., 2006). Therefore, it is difficult to settle an agreement for the definition of *n*. Additionally, Katz's model assumed P_{ves} to be constant which was

disproved, even if a release site refers to a single quantum or to a single AZ. Rather, the P_{ves} depends on the location of the SVs relative to the VGCC, the magnitude of the Ca^{2+} influx after an AP, and the intrinsic properties of the Ca^{2+} sensors (Körber and Kuner, 2016).

Despite the difficulties defining the quantal parameters, knowing *q*, *m*, or the frequency with which miniature events occur, is instrumental in understanding mechanisms regulating synaptic strength. For instance, alterations in *m* parallel to alterations in the spontaneous frequency are indicators of presynaptic alterations; meanwhile changes in *q*, usually relate to postsynaptic modifications.

1.2.2 Presynaptic Ca^{2+} mediates synaptic transmission

Ten years after the postulation of the "quantal hypothesis", a new hypothesis emerged at Katz's laboratory, the "Ca^{2+} hypothesis". By substituting Ca^{2+} for Mg^{2+} in the extracellular recording medium, Katz and Miledi revealed the direct action of Ca^{2+}-triggered vesicle release at the NMJ (Katz and Miledi, 1965). Ca^{2+} acts as an intracellular messenger during synaptic transmission. Understanding the intracellular Ca^{2+} dynamics in the presynaptic bouton is crucial for the later explanation of the mathematical approach which we have developed to analyze the role of RIM proteins in regulating neurotransmitter release.

After the postulation of the Ca^{2+} hypothesis by Katz, two colleagues of his, Dodge and Rahamimoff described the quantitative relationship between the extracellular Ca^{2+} concentration ($[Ca^{2+}]_e$) and neurotransmitter release. Plotting the postsynaptic potential amplitudes against the $[Ca^{2+}]_e$ displayed a steeply nonlinear relationship. Neurotransmitter release depends on the 4^{th} power of the $[Ca^{2+}]_e$. This implicates the binding of about four Ca^{2+} ions in a cooperative manner to a specific Ca^{2+} sensor leading to the release of a single SV (Dodge and Rahamimoff, 1967).

$$\mathrm{EPP} = \mathrm{k}[\mathrm{CaX}]^{\mathrm{n}} = \mathrm{k}\left(\frac{\mathrm{W}[\mathrm{Ca}^{2+}]_{\mathrm{e}}}{1 + \frac{[\mathrm{Ca}^{2+}]_{\mathrm{e}}}{\mathrm{K}_1}}\right)^{\mathrm{n}} \qquad (2)$$

The Dodge-Rahamimoff equation describes the power relationship between neurotransmitter release, and the $[Ca^{2+}]_e$. The amplitude of the postsynaptic

response, in this case, an end-plate potential (EPP) is proportional to the number of Ca^{2+} binding sites occupied by Ca^{2+}. In the formula (2), *k* is a proportionality constant, *W* is a constant, *K* is the affinity for Ca^{2+} binding to the Ca^{2+} sensor at release site, and *n*, the number of Ca^{2+} ion binding sites that must be occupied to trigger release. The relationship between transmitter release and $[Ca^{2+}]_e$ represents a dose-response curve. This equation partly reflects physiological conditions, as it is only valid at low levels of $[Ca^{2+}]_e$ and assumes no saturation of the postsynaptic receptors. The highly nonlinear relationship between $[Ca^{2+}]_e$ and transmitter release has also been confirmed at fast CNS synapses (Borst and Sakmann, 1996) and on cultured hippocampal neurons (Reid et al., 1998).

Llinás and Nicholson experimentally confirmed the Ca^{2+} hypothesis by detecting a transient increase in the presynaptic intracellular calcium concentration ($[Ca^{2+}]_i$) after an AP using the Ca^{2+}-sensitive photoprotein aequorin (Llinas and Nicholson, 1975). During the 1980s it was shown that the total calcium entry (I_{Ca}) at the presynaptic terminal is built up by the sum of individual calcium channel currents (i_{Ca}). The size of each i_{Ca} depends on the Ca^{2+} channel gating properties, which are not directly affected by the Ca^{2+} entry (Carbone and Lux, 1987), and on the Ca^{2+} driving force. Synaptic strength is steeply dependent on $[Ca^{2+}]_e$ and I_{Ca}. The relationship between these two parameters is described by a function for a bimolecular reaction scheme describing the Ca^{2+} channel pore occupancy by the $[Ca^{2+}]_e$ (Carbone and Lux, 1987, Mintz et al., 1995).

During resting conditions, the $[Ca^{2+}]_i$ at the terminal is maintained around 100 nM. Upon the arrival of an AP, the stochastic opening of VGCCs elicits a rapid increase in the $[Ca^{2+}]_i$, creating a Ca^{2+} microdomain of 10-100 µM (Llinas et al., 1992, Schneggenburger and Neher, 2000). The Ca^{2+} microdomains are produced by an overlap of Ca^{2+} concentration domains created by several open VGCCs located at short distances (Borst and Sakmann, 1996, Mintz et al., 1995). In other words, several VGCCs act synergistically at individual release sites. The $[Ca^{2+}]_i$ at the microdomain scales largely proportional with the I_{Ca} (Erdmann et al., 2012). $[Ca^{2+}]_i$ increases very rapidly within tens of microseconds (200-500 µs), and dissipates again within microseconds, due to endogenous Ca^{2+} buffering and passive diffusion,

allowing fast termination of the transmitter release. The short time lag between the I_{Ca} and the transmitter release, known as synaptic delay, suggests that only vesicles located near the Ca^{2+} source will undergo fusion. The coupling between Ca^{2+} source and Ca^{2+} sensor is a key factor determining the speed and efficacy of synaptic transmission.

Due to the nature of the Ca^{2+} signal at the presynaptic terminal, Ca^{2+} sensors triggering neurotransmitter release must have specific characteristics. They have to be located within the Ca^{2+} microdomain, present low affinity for Ca^{2+} and must have fast kinetics, to account for the speed of transmitter release, as well as high cooperativity. In 1992, Synaptotagmin-1 (Syt1) was identified as the major Ca^{2+} sensor for fast neurotransmitter release at the central synapse (Brose et al., 1992, Geppert et al., 1994). Synaptotagmins constitute a family of transmembrane proteins associated with SVs. They consist of two cytoplasmic Ca^{2+} binding domains: C_2A and C_2B, which bind several Ca^{2+} ions with an intrinsic low affinity. The binding of Ca^{2+} to both C_2 domains is crucial for a properly evoked synaptic transmission (Fernandez-Chacon et al., 2001, Mackler et al., 2002). Moreover, Syt1 mediates Ca^{2+}-dependent SV exocytosis by binding directly to the fusion machinery. Therefore, Syt1 serves as an essential player for the synchronization of Ca^{2+} entry and release during fast synaptic transmission (Südhof, 2013). Although Syt1 is the principal Ca^{2+}-sensor for synchronous transmitter release, other synaptotagmins, as Syt2 and Syt9, also mediate fast synaptic transmission at central synapses (Xu et al., 2007).

The high cooperativity of the Ca^{2+} sensors during an AP makes synaptic strength extremely sensitive to modulation by changes in the $[Ca^{2+}]_i$. Small changes in the I_{Ca}, for instance, a reduction by the usage of specific VGCC blockers, will have a larger impact on the synaptic strength, as we can anticipate from the simple power-law-description of the Ca^{2+}-dependence of release, being approximated by $(I_{Ca})^n$.

1.2.3 Synaptic plasticity

As aforementioned, the ability of the synapses to modify synaptic strength in response to activity is known as synaptic plasticity. The activity-dependent changes

in synaptic strength increase greatly the computational power of the neuronal networks. Two directions for synaptic plasticity are possible: facilitation, an increase in synaptic strength, or depression, a reduction of synaptic strength. Depending on how long the effect lasts, synaptic plasticity can be divided into short-term (from milliseconds to seconds) and long-term plasticity (from minutes to hours).

Short-term plasticity (STP) is thought to be primarily a presynaptic phenomenon. Changes in the synaptic strength are explained by changes in the P_{ves}. One of the most studied paradigms of short-term plasticity is the paired-pulse stimulation. During the paired-pulse protocol, two closely spaced APs are elicited, resulting in an alteration of the synaptic strength after the second stimulus. Synapses with an initial low P_r undergo large facilitation, where synapses with high P_r show small facilitation, or even, depression (Thomson, 2000). Classical studies explained short-term facilitation by an increase in the residual $[Ca^{2+}]_i$ during the second pulse due to buffering saturation during the first one, which would increase P_{ves}, and therefore, synaptic strength (Katz and Miledi, 1968). However, there are no experiments to date proving this hypothesis. However, Synaptotagmin-7 (Syt7), a Ca^{2+} sensor with high Ca^{2+} affinity and slow kinetics, has been shown to mediate synaptic facilitation without affecting fast neurotransmitter release (Jackman et al., 2016). Syt7 would be activated by Ca^{2+} entering during the first pulse, increasing P_{ves} and leading increased SV fusion in response to the second pulse.

In addition to STP, many synapses show long-term use-dependent changes in synaptic strength, i.e. long-term plasticity (LTP). The induction and expression of LTP operates mainly on the postsynaptic side by an alteration in the AMPA receptors (AMPAR) number or function, induced by NMDA receptors (NMDAR) activation. However, LTP can also be induced presynaptically by an increase in the amount of transmitter release (Nicoll and Schmitz, 2005). The long-lasting increase in synaptic strength is considered the substrate for memory and learning (Bliss and Collingridge, 1993).

In order to maintain the basal synaptic properties, synapses express another type of plasticity, homeostatic synaptic plasticity (Turrigiano and Nelson, 2004). Homeostatic modulation involves modification of ion channels and neurotransmitter

receptors expression on the postsynaptic side, as well as changes in neurotransmitter release on the presynaptic side, via retrograde signalling.

1.2.4 Scenario for synaptic transmission: the presynaptic active zone

The physiological properties of presynaptic neurotransmitter release imply that the process of synaptic transmission is tightly controlled. Ergo, if “form follows function”, neurotransmitter release must take place in a highly organized structure which allows its exceptional fast and precise regulation.

The presynaptic AZ is the site where SV release occurs. In electronmicrographs the AZ appears as an electron-dense complex containing several different proteins that are highly enriched: RIMs, RIM-binding proteins (RIM-BP), Munc-13s, ELKS, and α-liprins. Other proteins, such as Bassoon and Piccolo, are associated with AZ proteins and have a more peripheral function, guiding vesicles to the core of the AZ (Figure 1.2) (Südhof, 2012).

The spatial organization of the AZ accounts for its main purpose: the transformation of the AP into neurotransmitter release. Prior to vesicle fusion, SVs must undergo docking, a process that physically attaches the vesicles to the AZ, and priming, the process which renders docked SVs fusion competent. The number of docked vesicles defines the size of the readily releasable pool (RRP). The RRP comprises the SVs available for immediate release after an AP. Munc13s and RIMs act in docking and priming SVs at the AZ (Augustin et al., 1999, Deng et al., 2011). Moreover, RIM proteins, together with RIM-BPs, are involved in the recruitment of VGCCs to the AZ in close proximity to docked SVs (Acuna et al., 2015, Kaeser et al., 2011). Therefore, a protein complex, with RIM proteins as the main component, localizes VGCCs, SVs, and priming factors at the release sites, allowing fast evoked neurotransmitter release.

ELKS proteins, which bind to Bassoon, Piccolo, RIM, and α-liprins, play an important role in priming (Held et al., 2016), and anchoring of VGCC to the release site (Dong et al., 2018). Liprins-α bind to RIMs (Schoch et al., 2002), ELKS, and to receptor phosphotyrosine phosphatases (Serra-Pages et al., 1998), linking synaptic cell adhesion to the main AZ protein complex. Apart from this central protein matrix, the

AZ contains a high concentration of VGCCs. Each docked SV is likely to be surrounded by several channels.

A quantitative ultrastructural analysis of hippocampal excitatory synapses provided interesting data about the geometry of the presynaptic nerve terminal. At the hippocampal Schaffer collateral synapse, a model CNS synapse, most of the presynaptic boutons possess only one AZ. The average size of the AZ, if we considered it as a circular disk, is 0.2 µm of diameter. Each AZ typically contains 5 to 7 SVs in a fusion-ready state, most of them presumably belonging to the RRP, but more than 200 vesicles are present in the whole presynaptic bouton (Schikorski and Stevens, 1997).

Viewed together, the highly organized presynaptic AZ architecture accounts for its main purpose: the fast and precise Ca^{2+} signal to mediate quantal synaptic transmission and synaptic plasticity mechanisms.

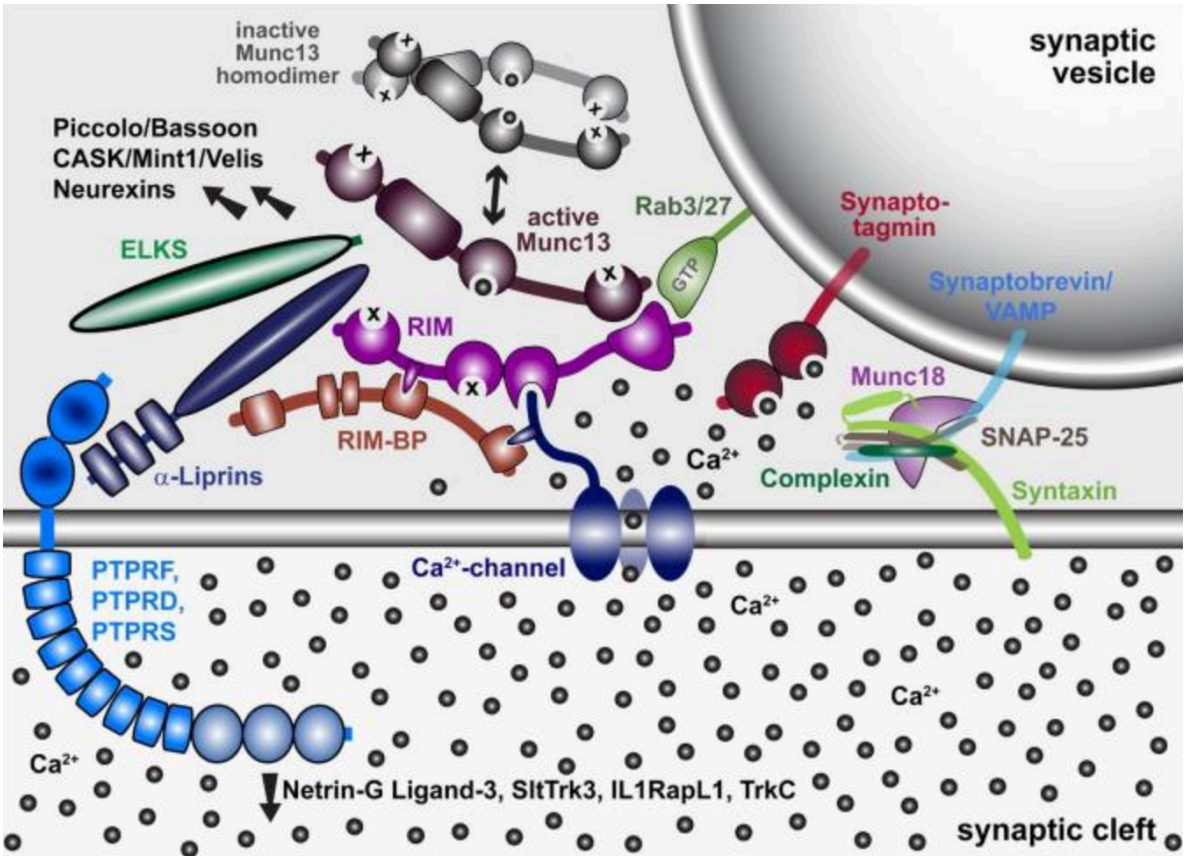

Figure 1.2 The presynaptic active zone. Molecular model of the active zone protein complex and its relation to the synaptic vesicle fusion machinery, VGCCs and synaptic cell-adhesion molecules (Südhof, 2012).

1.3 Voltage-gated Ca^{2+} channels

VGCCs convert electrical signals into intracellular signals, initiating many physiological processes, such as neurotransmitter release. VGCCs at the presynaptic terminal are tightly coupled to SVs, where the Ca^{2+} sensors are located. The synaptic strength is dependent on the type and the density of the VGCCs as well as on their distance to the docked SVs. Type, density, and location of VGCCs tunes directly the P_{ves} (Eggermann et al., 2011, Meinrenken et al., 2002).

1.3.1 Presynaptic Ca^{2+} channel subtypes: Structure and function

VGCCs are multi-subunit complexes of a principal pore-forming α_1 subunit, associated with an $\alpha_2\delta$ subunit, an intracellular β subunit and, in some cases, a transmembrane γ subunit. The main subunit α_1 contains four domains, each of which contains six transmembrane segments (S1-S6). The S1-S4 segments of each domain act as voltage sensors (Dunlap et al., 1995).

VGCCs have been classified in three families based on the α_1 subunit. Two families of high-voltage activated (HVA) Ca^{2+} channels, the Ca_v1 and the Ca_v2, and one family of low-voltage activated (LVA) Ca^{2+} channels, Ca_v3. The Ca_v1 or L-type channels are expressed in dendritic spines, where they contribute to synaptic input integration (Bean, 1989), and can be blocked by dihydropyridines (Reuter, 1983). The Ca_v2 family initiates synaptic transmission (Catterall, 2000), i.e. it is responsible for the Ca^{2+} entry at presynaptic terminals triggering transmitter release. It is subdivided into $Ca_v2.1$ or P/Q-type, $Ca_v2.2$ or N-type, and $Ca_v2.3$ or R-type channels. The Ca_v2 channels are regulated by a direct interaction with G proteins and SNARE proteins, which themselves are regulated by protein phosphorylation pathways, and also by direct binding of Ca^{2+}/calmodulin (Hille, 1994, Lee et al., 1999). They activate and inactivate rapidly, accounting for the speed of synaptic transmission (Augustine et al., 1985). The $Ca_v2.1$ or P/Q-type channels are sensitive to the funnel web spider (*Agelenopsis aperta*) toxin ω-agatoxin IVA (Agatx) (Mintz et al., 1992). The $Ca_v2.2$ or N-type channels are blocked by the cone snail (*Conus geographus*) peptide ω-conotoxin GVIA (Cgtx) (Kamiya et al., 1988). The Ca_v3 or T-type Ca^{2+} channels get activated at more negative membrane potentials, and are

present in neurons, where they are considered to drive rhythmicity generation (Choi et al., 2015).

1.3.2 VGCCs mediating neurotransmitter release: P/Q-type and N-type

Using pharmacology, two types of VGCCs have been identified to mediate neurotransmitter release at mammalian CNS synapses, P/Q-type and N-type. Inhibitory synaptic transmission tends to rely more on P/Q-type channels, whereas at glutamatergic excitatory synapses, transmitter release is mediated jointly by P/Q- and N-types (Takahashi and Momiyama, 1993).

Excitatory postsynaptic responses evoked in hippocampal CA1 pyramidal cells by stimulating the Schaffer collaterals can be dramatically suppressed by Agatx, but only partially blocked by Cgtx. Hence, at the Schaffer collateral synapses, both $Ca_v2.1$ and $Ca_v2.2$ channels are involved in the regulation of transmitter release, but the former plays a more prominent role (Horne and Kemp, 1991, Luebke et al., 1993, Takahashi and Momiyama, 1993, Wheeler et al., 1994). Other studies also revealed a simultaneous control of synaptic transmission by P/Q-type and N-type channels at the hippocampal CA3-CA1 synapse, though with similar contributions for both Ca_v2 channels. They proposed a colocalization of $Ca_v2.1$ and $Ca_v2.2$ channels at a single presynaptic terminal. By determining the relationship between transmitter release and I_{Ca}, they attributed the same efficacy triggering release to both types of Ca^{2+} channels, with a power number around 3 (Qian and Noebels, 2000, Wu and Saggau, 1994). Those results were confirmed in hippocampal neuronal cultures (Reid et al., 1998), and at the cerebellar excitatory synapse between granule cells and Purkinje cells (Mintz et al., 1995).

The information about the spatial arrangement of VGCCs at the presynaptic boutons remains scarce. It is known that VGCCs are confined to presynaptic terminals, shown by colocalization studies with scaffolding AZ proteins, such as RIM (Holderith et al., 2012). At central “simple synapses”, synapses with a single AZ, such as the Schaffer collateral terminals, VGCCs are organized in clusters, each cluster containing only few Ca^{2+} channels (Scimemi and Diamond, 2012). The number of VGCC clusters per AZ seems to be closely correlated with the number of functional

releasing sites, in other words, with the number of docked SVs (Miki et al., 2017). The colocalization of VGCCs and SVs is possible thanks to a direct protein interaction, via a specific domain called synprint, to SNARE proteins, and to the SV-associated protein, synaptotagmin (Mochida et al., 2008). Furthermore, VGCCs are anchored at the presynaptic boutons due to their direct binding to AZ proteins, such as RIMs or RIM-BPs (Hibino et al., 2002, Kaeser et al., 2011). Those molecular interactions define coupling distances of 10 to 100 nm between the Ca^{2+} source and the Ca^{2+} sensor.

During development, the type and localization of VGCCs can undergo modifications: a tightening of the coupling distance, from a microdomain to a nanodomain structure, together with a downregulation of N-type channels (Kusch et al., 2018).

The amplitude and the time course of the Ca^{2+} influx through $Ca_V2.1$ and $Ca_V2.2$ are similar (Wu et al., 1999), but they can be regulated differently, allowing a very specific regulation of presynaptic transmitter release.

Given the importance of the Ca^{2+} signalling regulating neurotransmitter release, the VGCC subtypes level as well as their arrangement at the presynaptic bouton are expected to have a great impact on controlling synaptic strength and thus, shaping neural coding.

1.4 RIM protein family

The first RIM protein identified was RIM1α, as a potential effector protein for Rab3, a GTPase anchored to the membrane of SVs (Wang et al., 1997). RIM1α is the founding member of the RIM protein family. The RIM family is expressed by four different genes in the mammalian genome (*Rims1-4*), which encode for seven proteins: four large RIM isoforms, RIM1α/β and RIM2α/β, and three small RIM isoforms, RIM2γ, RIM3γ, and RIM4γ (Kaeser et al., 2008, Wang and Südhof, 2002, Wang et al., 2000). The α-RIMs are composed of the full complement of RIM domains: a N-terminus, composed of a Zn^{2+} finger domain surrounded by an helical sequence, a central PDZ domain, and two C-terminal C_2 domains, called C_2A and C_2B. Between both C_2 domains, there is a conserved proline-rich sequence, that can

bind to SH3-domains. β-RIMs are identical to α-RIMs but lack the Rab3-binding part of the N-terminal Zn^{2+} finger in RIM1β and the whole Zn^{2+} finger domain in RIM2β. The γ isoforms consist only of the C-terminal C_2B domain and a specific N-terminal sequence. The C_2 domains of RIM proteins are considered atypical because they do not bind to Ca^{2+} (Figure 1.3 A). The RIM protein family is primarily expressed in the brain, and was first described to play a potential role in exocytosis (Wang et al., 1997).

1.4.1 Large RIM isoforms: RIM1α/β and RIM2α/β

α/β-RIMs are scaffolding proteins located at the matrix of the presynaptic AZ. Studies in *C.elegans* and mice proposed an active role for the large RIM proteins regulating presynaptic vesicle exocytosis (Gracheva et al., 2008, Wang et al., 1997). Through multiple molecular interactions with other AZ proteins as well as proteins located on the SVs, α/β-RIMs may control several aspects of neurotransmitter release.

RIM1 and RIM2 proteins are highly homologous, present similar expression patterns, and are exceptionally polymorphic due to extensive alternative splicing. Nevertheless, RIM1 isoforms are the most abundant RIM proteins (Wang et al., 1997). Studies on cultured hippocampal neurons and at the Calyx of Held synapse, a large CNS model synapse, showed a redundancy of both RIM1 and RIM2 in their presynaptic function (Han et al., 2015, Kaeser et al., 2012). Both isoforms encoded by *Rims1*, RIM1α and RIM1β, display overlapping expression patterns, while their redundant effect on synaptic transmission concerns only a few basic processes, most likely due to their different N-terminal domain (Kaeser et al., 2008).

1.4.1.1 Biochemical interactions of α/β-RIMs and their physiological implications

Due to their multidomain structure, the large RIM proteins can engage in multiple protein-protein interactions which are most likely crucial for their function regulating neurotransmitter release.

The helical sequence of the N-terminal domain present in the α-RIMs but absent in the RIM1β isoform, binds to the GTP-binding protein Rab3, which is associated to

the SVs, thus, linking RIM to SVs. The N-terminal Zn^{2+} finger binds to the C_2A domain of Munc13. The binding of RIM to Munc13, disrupts the Munc13 homodimer, thus activating Munc13 (Deng et al., 2011). Munc13 itself mediates SVs priming by changing the conformation of syntaxin, a member of the fusion release machinery. Likely, RIM's function during the priming process consists in the activation of Munc13. Noteworthy is the fact that in RIM1α deficient mice, Munc13-1 expression levels are reduced by approximately 60% (Schoch et al., 2002). Taken together, RIM forms a tripartite complex with Rab3 and Munc13 via the N-terminal domain, which is involved in priming, i.e. maintaining SVs in a release-ready state, which potentially impacts synaptic plasticity. Located at the large linker sequence between the Zn^{2+} finger and the PDZ domain, there is a phosphorylation site, the S413, which its PKA-dependent phosphorylation induces its binding to 14-3-3 adaptor proteins (Simsek-Duran et al., 2004). The central PDZ domain binds directly to the C-terminal of another AZ protein, ELKS, which itself binds to Bassoon, Piccolo, and α-liprins, assuring a tight macromolecular complex at the AZ, and its connection with more distal areas of the presynaptic bouton. Furthermore, the central PDZ domain binds directly to the C-terminal of the P/Q-type and N-type VGCCs. This interaction tethers VGCCs to SVs, which is essential for localizing Ca^{2+} entry at the AZ (Han et al., 2011, Kaeser et al., 2011). The proline-rich motif, located between the two C_2 domains, binds to the SH3 domains of the RIM-BPs (Hibino et al., 2002). At the same time, RIM-BPs interact directly with L-type, N-type, and P/Q-type VGCCs (Hibino et al., 2002). The simultaneous binding of RIM-BP to VGCCs, constitutes an alternative link between RIM proteins and Ca^{2+} channels. The direct and indirect interactions of RIMs with VGCCs are important for maintaining sufficient and localized Ca^{2+} entry to trigger fast SV release. Additionally, the RIM C_2B-domain, present in all RIM isoforms, binds to the β subunit of the VGCCs, exerting a suppression in their inactivation (Kiyonaka et al., 2007, Uriu et al., 2010). Liprins-α, which bind to receptors at the presynaptic membrane, also bind to the C_2B-domain of RIM proteins (Schoch et al., 2002). Recently, the C_2B-domain of RIM proteins has also been shown to interact with the phospholipid PIP_2 (De Jong et al., 2018). Apart from the interactions of RIM with other molecules, crystallography analysis has documented

a possible dimerization between two RIM proteins via the C_2B-domain (Guan et al., 2007) (Figure 1.3 B).

Other molecular interactions of RIM proteins have been observed *in vitro*, but remain to be demonstrated *in vivo*, such as an interaction with the SNARE protein, SNAP-25, or with Syt1 (Coppola et al., 2001).

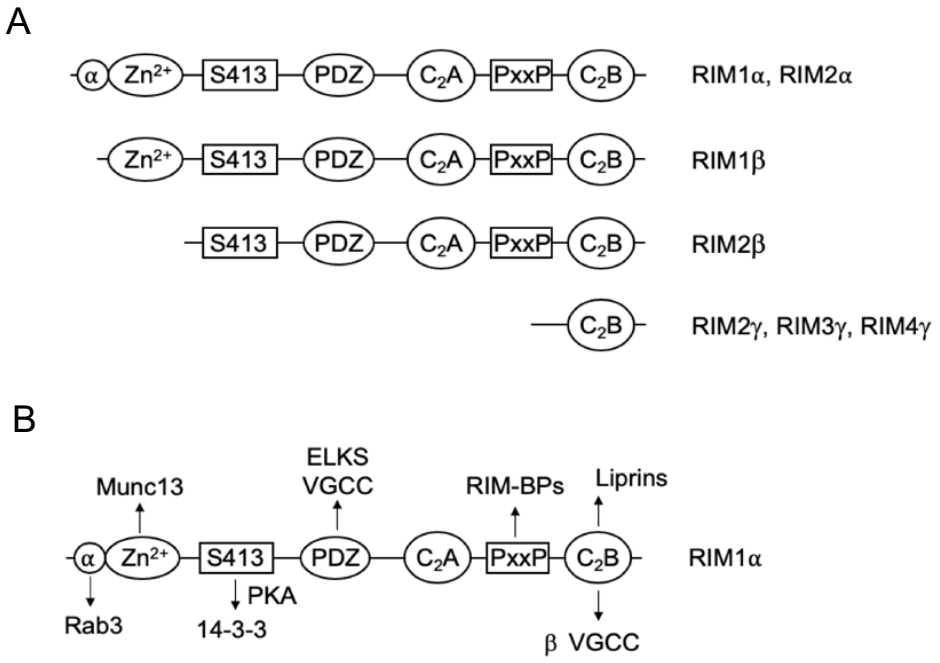

Figure 1.3 RIM protein family organization and protein interaction of RIM1α. (A) Domain structure of the RIM isoforms generated from the four RIM genes. (B) RIM1α isoform showing its biochemical interactions by the different domains.

The localization, structure, and protein interactions of RIM1 and RIM2 isoforms put them at the core of the presynaptic AZ modulating different aspects of the neurotransmitter release. RIM proteins may play an essential role in regulating synaptic strength at the presynaptic level, synaptic plasticity, and information processing at neuronal circuits.

1.4.1.2 α/β-RIMs function in transmitter release and synaptic plasticity

As we deduce from their molecular interactions, the large RIM isoforms, and therefore, RIM1α, regulate several facets of the presynaptic neurotransmitter

release. The constitutive and conditional genetic ablation of the different RIM isoforms, knockout (KO), in animal models, has facilitated the study of the RIM function in synaptic transmission. The ablation of RIM isoforms demonstrated a role for RIM proteins coregulating Ca^{2+} channel transmitter release coupling, and the RRP size. Several studies revealed a strong reduction of the synaptic transmitter output, without altering the ultrastructure of the presynapse (Calakos et al., 2004, Han et al., 2011, Kaeser et al., 2011, Schoch et al., 2002). The loss of RIM1/2 isoforms produced a decreased presynaptic I_{Ca} in cultured hippocampal neurons (Kaeser et al., 2011), at cerebellar granule cells (Kintscher et al., 2013), and at the Calyx of Held (Han et al., 2011), probably due to a decreased VGCC density at the release site. Quantitative immunofluorescence showed a 40% decrease in P/Q-type VGCC level in conditional double RIM1/2 knockout (cDKO) synapses (Kaeser et al., 2011). At the Calyx of Held, the amplitude of the $[Ca^{2+}]_i$ transient at the Ca^{2+} sensor, estimated using release kinetics and Ca^{2+} uncaging data, was slightly decreased (Han et al., 2011). This result is consistent with a weaker coupling between Ca^{2+} channels and Ca^{2+} sensor in RIM1/2 cDKO synapses, obtained by the analysis of Ca^{2+} chelators effect on transmitter release (Kaeser et al., 2011). The Ca^{2+} dependence of SV release was suggested to be normal at RIM1α KO autaptic neurons (Calakos et al., 2004). In contrast, Ca^{2+} responsiveness of release was decreased at RIM1/2 cDKO synapses, which indicated an unchanged Ca^{2+} cooperativity (Kaeser et al., 2011). This suggests that the large RIM isoforms enable fast and synchronous triggering of transmitter release. At several synapse types investigated, a reduction in the size of the RRP, was shown, implying an impairment in priming (Calakos et al., 2004, Fernandez-Busnadiego et al., 2013, Han et al., 2011, Kaeser et al., 2011). The ablation of RIM1α increased the paired-pulse facilitation (PPF), a form of short-term synaptic plasticity, at the hippocampal CA3-CA1 synapses, indicating a decrease P_r (Schoch et al., 2002). P_{ves} was also decreased at the RIM deficient Calyx of Held synapse, but in a much lesser extent (Han et al., 2011).

RIM proteins play different roles at different excitatory synapse types. As shown above, at the hippocampal Schaffer collateral synapses, RIM proteins are essential for basic neurotransmitter release and short-term plasticity. However, the induction

of NMDAR-dependent LTP present at those synapses does not required RIM (Schoch et al., 2002), although is essential for the maintenance of the LTP (Huang et al., 2005). At the hippocampal mossy fibers of RIM deficient mice PKA-dependent presynaptic LTP was completely abolished (Castillo et al., 2002). In addition to the involvement of RIM proteins in short-term and long-term synaptic plasticity, RIM has been found to mediate presynaptic homeostatic plasticity by the modulation of the RRP at the Drosophila NMJ (Müller et al., 2012).

The large RIM isoforms control the Ca^{2+}-mediated SV exocytosis and the size of the RRP, via their multiple interactions at the AZ, which impact synaptic strength and synaptic plasticity. Those abnormalities in basic transmitter release and synaptic plasticity are reflected in memory and learning deficits in RIM1α KO mice (Powell et al., 2004).

1.4.2 Small RIM isoforms: RIM3γ and RIM4γ

Albeit much is known about the large RIM isoforms, the small isoforms are the “great unknown” of the RIM protein family. As previously mentioned, RIM3 and RIM4, are composed only of the RIM-specific C-terminal C_2B domain and varying N sequences. As the α and β isoforms, γ-RIMs are also mainly expressed in the brain, where they present a broader subcellular expression pattern. γ-RIMs are components of the presynaptic and postsynaptic cytomatrix, and can also be found in dendrites and in the soma (Alvarez-Baron et al., 2013). The first studies investigating the physiological functions of the γ isoforms, suggested that, as α/β-RIMs, they bind to VGCCs modulating their opening by suppressing their inactivation, and sustaining presynaptic Ca^{2+} influx (Uriu et al., 2010). Furthermore, RIM3 and RIM4 seem to be important for the development of normal neuronal arborization of the dendritic tree (Alvarez-Baron et al., 2013). Newly generated constitutive RIM4 KO mice show a strong motor phenotype, which could be reproduced by the specific loss of RIM4 at the Purkinje cells (unpublished data). From those data, we can hypothesize a wider role for the γ-RIMs compared to α-RIMs. The function of RIM3 and RIM4 putatively varies depending on the brain region and subcellular compartment in which they are expressed.

1.5 Hippocampal Schaffer collaterals as a model of central synapses

With his wondrous drawings in 1899 Santiago Ramón y Cajal revealed the elegant anatomy and circuitry of the hippocampus (Figure 1.4 B). This fascinating brain structure has awakened the interest of scientists since distant times. Already in the 16th century, the hippocampus was first described and named after its resemblance with the seahorse. Nowadays, the hippocampus is one of the most investigated structures in the brain and its role in consolidation of information and spatial memory is well stablished (Martin and Clark, 2007).

For several reasons, we have selected the hippocampal Schaffer collateral synapses, the synapse between the axon collaterals given off by CA3 pyramidal neurons and the CA1 pyramidal cells, as a model synapse. First, the Schaffer collaterals represent a typical ubiquitous small central synaptic terminal, where Ca^{2+}-dependent transmitter release is mediated by P/Q- type and N-type VCGGs (Horne and Kemp, 1991, Luebke et al., 1993, Takahashi and Momiyama, 1993, Wheeler et al., 1994). Second, the highly organized laminar arrangement of neurons in the hippocampus makes it an ideal structure for field potential recordings (Johnston and Wu, 1995). Third, the Schaffer collateral synapses are facilitating synapses which can convey short- and long-term changes of synaptic strength. Last but not least, there is a large body of previous reports on this synapse, ensuring comparability with other findings in the field.

1.5.1 Anatomy of the hippocampal formation

The brain contains two hippocampi, one in each medial temporal lobe (Figure 1.4 A). The hippocampus belongs functionally to the limbic system. It is one of several regions of a functional system called the hippocampal formation. Other regions of the hippocampal formation are the dentate gyrus (DG), the subiculum, and the entorhinal cortex (EC). The hippocampus proper has three subdivisions: CA3, CA2, and CA1; CA stands for the term "*cornu ammonis*" or "Ammon's horn". Moreover, the hippocampus proper presents a depth-wise laminar organization shaped by several layers. The stratum oriens is the deepest layer and contains the basal dendrites of the pyramidal neurons. The stratum pyramidale is formed by the cell

bodies of the excitatory pyramidal cells and few interneurons. The stratum radiatum is located above the stratum pyramidale and contains many subtypes of interneurons as well as the Schaffer collateral axons, which are the projection forward from CA3 to CA1. The most superficial layer of the hippocampus is the stratum lacunosum-moleculare, where CA1 neuronal dendrites receive direct input from the EC.

The hippocampal formation presents a unique set of unidirectional, excitatory pathways. The main input of the hippocampus comes from the EC, which projects to the DG, to CA3, and to CA1, via the perforant path. The principal cells of the DG, the granule cells, project to the CA3 pyramidal cells via mossy fibers projections. The pyramidal cells of the CA3 region project via the Schaffer collateral axons to the CA1 pyramidal cells as their major input. CA1 pyramidal neurons project to the subiculum, and together, with the subiculum, connect to the deep layer of the EC, closing the hippocampal processing loop (Andersen et al., 2007).

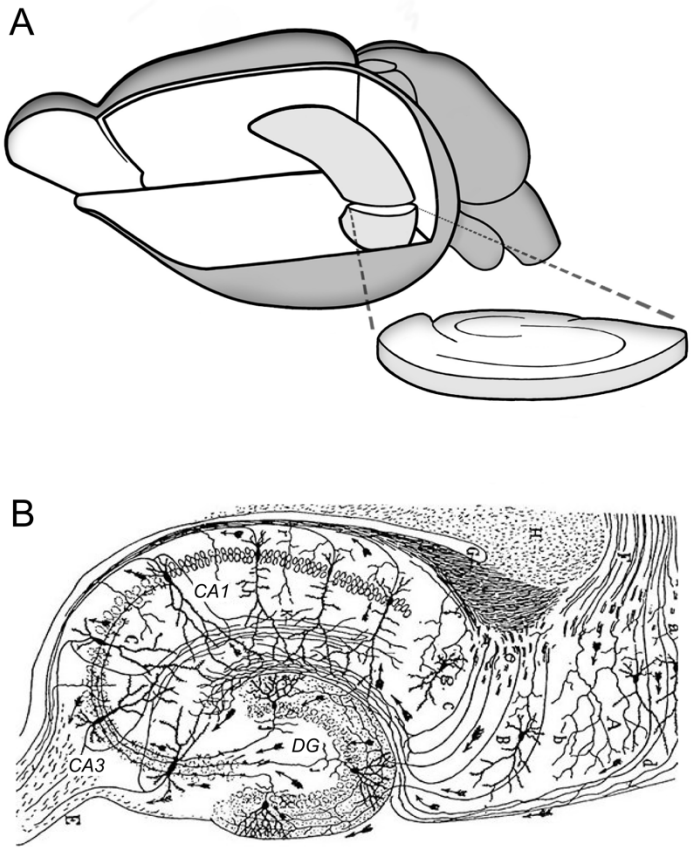

Figure 1.4 Anatomy of the hippocampal formation. (A) Schematic view of the mice brain. Hippocampal formation after cortical surface removal, and horizontal hippocampal slice. (B) Classical drawing of the hippocampal formation by Ramón y Cajal, modified from (Ramón y Cajal, 1899), illustrating the dentate gyrus (DG), and the proper hippocampal areas CA3 and CA1.

1.5.2 Function of the hippocampal formation

Albert Einstein once said, “The measurement of intelligence is the ability to change”. No other brain structure, but the hippocampus, mirrors better the meaning of those words. The hippocampus is able to process information and change it, by means of synaptic strength tuning, and structural plasticity. It can undergo different types of synaptic plasticity, as LTP, which is defined as the cellular bases of the memory (Bliss and Collingridge, 1993). Furthermore, the hippocampus has been identified to play a role in memory formation by providing the brain with a spatiotemporal framework in which multimodal sensory information can be processed together (Knierim, 2015).

1.6 Aim of the study

Presynaptic terminals perform computational tasks by converting trains of APs into adaptable patterns of transmitter release. The composition and state of the AZ determines release probability and availability of SVs for release which is important for the temporal pattern of transmitter release (STP) and the electrical impact on the postsynaptic neurons. At the AZ, VGCCs are located near SVs allowing for fast neurotransmitter release. Among the AZ proteins, the large RIM isoform, RIM1α is a candidate to play a crucial role in synaptic computation; thus, RIM1α is necessary for synaptic plasticity as well as for maintaining presynaptic VGCC density and docked SVs. The ablation of RIM1α leads to a strong reduction of synaptic output and impaired short-term synaptic plasticity. Further studies are warranted to elucidate if these alterations are caused by a lack of docked SVs or by a decrease in the $[Ca^{2+}]_i$ operating the Ca^{2+} sensor, which would impact temporal release properties and thus, synaptic computation.

The main goal of this project was to increase knowledge about the role of three members of the RIM protein family, RIM1α, RIM3, and RIM4 as modulators of fast synaptic transmission, and their possible function in synaptic computation. By the selective deletion of the individual RIM isoforms together with electrophysiological recordings, and Ca^{2+} imaging, we aimed to analyze the functional role of RIM1α in controlling the Ca^{2+} signal mediating neurotransmitter release, and to examine the potential role of RIM3 and RIM4 in synaptic transmission, and the underlying mechanisms.

To pursue our main goal, we addressed the following aims:

Aim 1: Determine if ablation of RIM1α, RIM3, and RIM4 alters the number of functional synapses by quantifying the mean frequency of miniature excitatory postsynaptic currents (mEPSC).

Aim 2: Explore the nature of the AP-evoked Ca^{2+} microdomain at the presynaptic release machinery. We performed a mathematical approach based on field potential recordings which allowed us to precisely investigate the AP-evoked Ca^{2+} signal at the AZ. We quantitatively estimated Ca^{2+} binding parameters of the release

machinery, such as apparent Ca^{2+} affinity and cooperativity, relative release probability, and relative contribution of different types of presynaptic VGCCs to transmitter release.

Aim 3: Examine the effect of RIM1α, RIM3, and RIM4 deletion on short-term synaptic plasticity.

Aim 4: Assess the role of RIM1α in regulating the presynaptic Ca^{2+} entry at the Schaffer collaterals.

Performing those experiments helped us getting a better understanding of the role of three members of the RIM protein family, RIM1α, RIM3, and RIM4, in the regulation of the presynaptic release machinery and therefore, in regulating neurotransmitter release. We investigated the Ca^{2+} signal built up at the AZ by quantifying Ca^{2+} binding parameters, relative P_{ves}, and the contribution of the different VGCC subtypes to synaptic transmission. In summary, we expected to shed new light on the function of RIM1α, RIM3, and RIM4 regarding basic neurotransmitter release, the relationship of this function to synaptic plasticity, and its possible implication in presynaptic computation.

2 Materials and methods

2.1 Animals

2.1.1 Species

To investigate the role of RIM proteins in synaptic transmission, experiments were performed on male and female RIM1$\alpha^{+/+}$, RIM1$\alpha^{-/-}$ (RIM1α KO) (Schoch et al., 2002), RIM3$\gamma^{+/+}$, RIM3$\gamma^{-/-}$ (RIM3 KO) (Picher et al., 2017), RIM4$\gamma^{+/+}$, RIM4$\gamma^{-/-}$ (RIM4 KO) (unpublished), Et(iCre)-tdTomato-cDKO (see 2.4.3.4), and C57BL/6 mice, with an age range of six to eight weeks. KO mice, for RIM3 and RIM4, were newly generated in collaboration with Prof. Dr. Susanne Schoch-McGovern (unpublished data). RIM1α KO mice are viable, fertile and do not show an overt phenotype (Schoch et al., 2002). We found that both, RIM3 KO and RIM4 KO animals, are also viable and fertile, but the latter one displays a strong motor phenotype (unpublished data). All procedures were performed in accordance with the guidelines of the Bonn University Medical School Care Committee. Mice were kept in an animal facility, with water and food provided *ad libitum*, and under the control of an alternating 12-hour light or dark cycle.

2.1.2 Slice preparation

For the preparation of acute brain slices, mice were anesthetized using Isoflurane (Abbot, Chicago, IL, USA) and decapitated with a small rodent guillotine (DCAPS, World Precision Instruments, Sarasota, FL, USA). The brain was rapidly removed and transferred to ice-cold, high sucrose, oxygenated bicarbonate modified artificial cerebrospinal fluid (mACSF) (see 2.2.1). Straightaway, it was dissected on a cooled, mACSF filled metal dish. First, the forebrain and the cerebellum were cut off along the coronal plane. Then, the two hemispheres were separated along the longitudinal fissure. Finally, a slight piece of the cortex was removed along the rostral-caudal

axis. Both hemispheres were glued to the vibratome tissue holder by the cortex side. Either 300 (for field potential recordings in the submerged chamber, patch clamp recordings, and Ca2+ imaging) or 500 µm (for field potential recordings in the interface chamber) thick horizontal hippocampal slices were prepared with a vibratome (Microm, HM650V, Thermo Fisher Scientific, Waltham, MA, USA) (Figure 2.1) Afterward, the slices were incubated in mACSF for 30 minutes at 35 °C in a water bath (WNB 22, Memmert GmbH and Co. KG, Schwabach, Germany). Subsequently, the brain slices were stored at room temperature (22-24 °C) in oxygenated bicarbonate standard artificial cerebrospinal fluid (sACSF) (see 2.2.1).

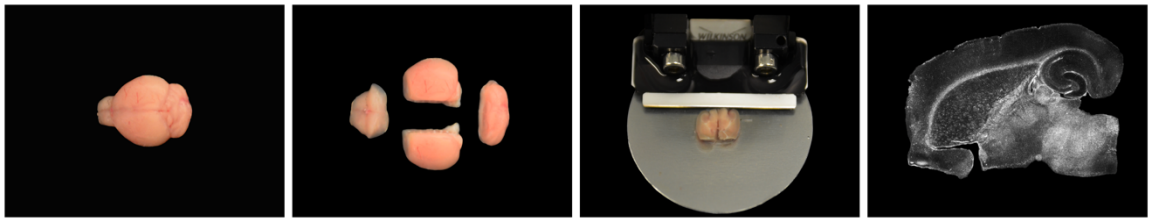

Figure 2.1 Horizontal hippocampal slicing procedure. The sequence of steps during slicing the brain in order to obtain horizontal hippocampal slices: removal of the brain from the skull, separation of both hemispheres and coronal cut of the forebrain and the cerebellum, and slicing along the rostral-caudal axis.

2.2 Solutions

2.2.1 Incubation/perfusion solutions

During slice preparation, the slices were stored in mACSF containing (in mM): 87 NaCl, 2.5 KCl, 1.25 NaH_2PO_4, 7 $MgCl_2$, 0.5 $CaCl_2$, 25 $NaHCO_3$, 25 glucose, and 75 sucrose (pH 7.4) (95% O_2, 5% CO_2). Afterward, they were stored with sACSF containing (in mM): 124 NaCl, 3 KCl, 1.25 NaH_2PO_4, 2 $MgCl_2$, 2 $CaCl_2$, 26 $NaHCO_3$, and 10 glucose (pH 7.4) (95% O_2, 5% CO_2).

For recordings of field excitatory postsynaptic potentials (fEPSP), patch-clamp recordings, and Ca^{2+} imaging, slices were transferred to a submerged chamber and continuously perfused (1-2 ml/min) with sACSF at room temperature, except for when the $[Ca^{2+}]_e$ was altered (see below).

For fEPSPs recordings at physiological temperature, slices were alternatively transferred to a Haas-type interface chamber and perfused (2-3 ml/min) with

oxygenated bicarbonate ACSF at 35 °C (35 °C ACSF) containing (in mM): 125 NaCl, 3 KCl, 1.25 NaH_2PO_4, 2 $MgCl_2$, 2 $CaCl_2$, 20.3 $NaHCO_3$, and 12 glucose (pH 7.4) (95% O_2, 5% CO_2), unless the $[Ca^{2+}]_e$ was modified (see below).

In order to prepare extracellular solutions containing different Ca^{2+} concentrations, for Ca^{2+} concentrations lower than 4 mM, the Mg^{2+} concentration of the ACSF was adjusted to maintain the total concentration of these two divalent cations at 4 mM. For extracellular solutions containing 4 mM Ca^{2+}, the concentration of Mg^{2+} was lowered to 0.1 mM and 25 µM D-2-amino-5-phosphonopentanoic acid (D-APV) was added to limit the activation of NMDAR.

We used a HEPES-buffered artificial cerebrospinal fluid (HEPES ACSF) to reliably avoid any precipitation of Ca^{2+} when using $[Ca^{2+}]_e$ of 10 and 20 mM. Ten mM Ca^{2+} HEPES ACSF contained (in mM): 133 NaCl, 3 KCl, 1 $MgCl_2$, 10 $CaCl_2$, 8 glucose, 7 HEPES, and 0.025 D-APV (pH 7.4, NaOH). Twenty mM Ca^{2+} HEPES ACSF contained (in mM): 120 NaCl, 3 KCl, 1 $MgCl_2$, 20 $CaCl_2$, 5 glucose, 6 HEPES, 0.025 D-APV (pH 7.4, NaOH) (Erdmann et al., 2012).

For recordings in cultured hippocampal neurons, the extracellular solution contained (in mM): 140 NaCl, 5 KCl, 2 $MgCl_2$, 2 $CaCl_2$, 10 glucose, and 10 HEPES (pH 7.4, NaOH).

2.2.2 Patch-clamp recording solutions

For evoked excitatory postsynaptic currents (EPSC) and mEPSCs recordings in hippocampal slices, the recording pipette solution contained (in mM): 130 K-Gluconate, 4 NaCl, 5 KCl, 0.5 $MgCl_2$, 4 Na_2ATP, 10 HEPES, and 0.1 EGTA (pH 7.3, KOH).

For NMDAR-mediated EPSCs recordings in hippocampal cultured cells, the pipette solution contained (in mM): 95 Cs-methanesulfonate, 4 NaCl, 2 MgATP, 0.4 NaGTP, 10 phosphocreatine-Na, 10 HEPES, 5 EGTA, 5 QX-314 chloride, and 25 tetraethylammonium (TEA) (pH 7.3, CsOH).

For evoked inhibitory postsynaptic currents (IPSC) and miniature inhibitory postsynaptic currents (mIPSC) recordings in cultured hippocampal cells, the pipette

solution contained (in mM): 90 K-Gluconate, 4 NaCl, 45 KCl, 0.5 $MgCl_2$, 4 Na_2ATP, 10 HEPES, 0.1 EGTA, and 5 QX-314 chloride (pH 7.3, KOH).

2.2.3 Ca^{2+} imaging solutions

For imaging of intraterminal Ca^{2+} transients, 50 µg cell-permeant Mg^{2+} Green (Mg-Green) acetoxymethyl (AM) dye (Thermo Fisher Scientific, Waltham, MA, USA) were dissolved in 50 µl of dimethyl sulfoxide (DMSO; SIGMA, St. Louis, Missouri, USA) containing 25% pluronic F-127 (SIGMA, St. Louis, MO, USA) (the stock solution was prepared with 250 mg of pluronic F-127 dissolved in 1 ml of DMSO). The solution was vortexed for 30 seconds and sonicated for five minutes. 450 µl of sACSF were added to this solution. The labeling solution, which contains Mg-Green AM, DMSO/pluronic and sACSF, was vortexed, sonicated, filtered, and kept on ice.

2.3 Chemicals and reagents

Chemical	**Target**	**Pharmacology**	**Supplier**	**Working concentration**
ω-Conotoxin GVIA	N-type Ca^{2+} channel	blocker	BACHEM	1µM
ω-Agatoxin IVA	P/Q-type Ca^{2+} channel	blocker	BACHEM	0.1µM, 1µM
SNX-482	R-type Ca^{2+} channel	blocker	Abcam	1µM
Nickel	T- and R-type Ca^{2+} channel	blocker	SIGMA	100µM
Verapamil	T- and L-type Ca^{2+} channel	blocker	SIGMA	10µM
Nimodipine	L-type Ca^{2+} channel	blocker	SIGMA	10µM

Cobalt	$Ca^{2+}{}_v$ channel	blocker	Fluka	2mM
SR 95531 hydrobromide (gabazine)	$GABA_A$ receptor	competitive antagonist	TOCRIS	10µM
CNQX	AMPA/kainate receptor	competitive antagonist	TOCRIS	10µM, 20µM
D-APV	NMDA receptor	competitive antagonist	TOCRIS	100µM
MK-801	NMDA receptor	non-competitive antagonist	TOCRIS	40µM
4-AP	$K^+{}_v$ channel	blocker	SIGMA	100µM
TTX	$Na^+{}_v$ channel	blocker	BIOTREND	1µM
Glycine	NMDA receptor	agonist	Carl Roth	15µM
EGTA-AM	Ca^{2+}	chelator	Invitrogen	100µM
EGTA	Ca^{2+}	chelator	PanReac, AppliChem	0.1mM, 5mM
TEA	$K^+{}_v$ channel $K^+{}_{Ca}{}^{2+}$ channel	blocker	SIGMA	25mM
QX-314 chloride	Na^+ channel	blocker	TOCRIS	5mM

2.4 Field excitatory postsynaptic potentials

Field potentials are signals generated by the electrical field produced by the activity of a group of neurons. They are measured between two points in the extracellular space, i.e. recording extracellularly at a certain point with respect to a distant ground

electrode. Extracellular field potentials are used to infer the activity of a neuronal population evoked by a synchronous synaptic input, for example, through stimulation of an afferent pathway.

Pyramidal neurons in the hippocampus have the dendrites facing in one direction and the somata in the other. This open field arrangement is ideal for recording a typical extracellular field potential (Figure 2.2). Typically, the stimulating electrode is placed on the Schaffer collateral fibers for orthodromic activation of the hippocampal CA1 pyramidal neurons and the recording electrode is inserted in the apical dendritic region of the CA1 area. The classic waveform of a fEPSP consists of a fiber volley, which indicates the presynaptic AP at the recording site, and, of the population EPSP (pEPSP), which is the field potential in the dendrites. If the electrical stimulation is sufficiently strong, the pEPSP can be contaminated by the population spike (pSpike), which corresponds to the AP in the postsynaptic neurons (Johnston and Wu, 1995). In this study, we recorded hippocampal Schaffer collateral-evoked fEPSPs in the CA1 hippocampal stratum radiatum.

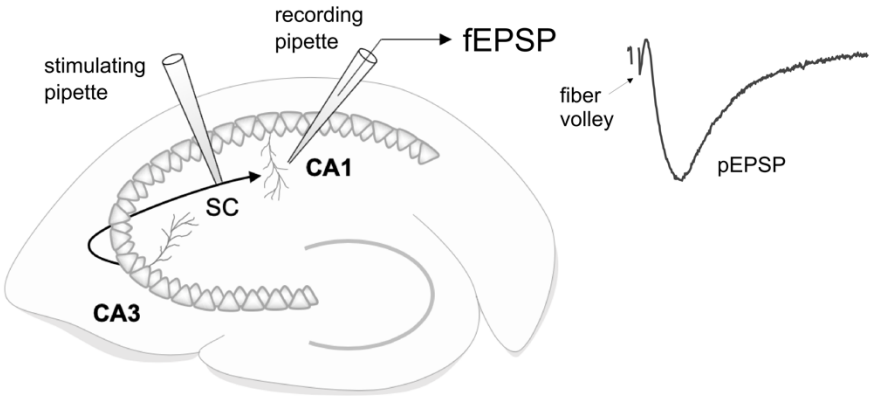

Figure 2.2 Scheme of Schaffer collateral-evoked fEPSPs recordings and a classical fEPSP waveform. The stimulating and recording electrodes are placed in the stratum radiatum of the hippocampal CA1 region. A typical fEPSP consists of a fiber volley and a pEPSP.

2.4.1 Setup

For fEPSPs recordings, horizontal hippocampal slices (300 µm thickness) were placed in a submerged recording chamber, positioned in a fluorescence microscope

(ECLIPSE E600FN, Nikon, Shinagawa, Tokyo, Japan). Slices were perfused with sACSF or HEPES ACSF containing different Ca^{2+} concentrations.

For physiological fEPSPs recordings, horizontal hippocampal slices (500 µm thickness) were positioned on a piece of lens paper and placed in a Haas-type interface recording chamber (Figure 2.3). The Haas-type interface chamber allows higher quality recordings as well as faster exchange of the perfusion fluid (Haas et al., 1979). Slices were perfused with 35 °C ACSF containing different Ca^{2+} concentrations. Slice and electrode positioning were managed with the help of a stereomicroscope (Citoval 2, Zeiss, Oberkochen, Germany).

In both types of recordings, signals were amplified with a field potential amplifier EXT-02F/2 (npi electronic GmbH, Tamm, Germany) and a postamplifier BF-48DGX (npi electronic GmbH, Tamm, Germany). A Hum Bug (HumBug Noise Eliminator, Digitimer, Welwyn Garden City, United Kingdom) was used to remove 50 or 60 Hz noise from the recorded signals. Those signals were filtered at 3 kHz and digitized with a sampling frequency of 10 kHz (NI USB-6229 National Instruments, Austin, TX, USA). The recordings were monitored on-line with an oscilloscope (Tektronix DPO 2024B Digital Phosphor Oscilloscope, Beaverton, OR, USA or Hameg HM507, Mainhausen, Germany). Stimulation protocols were delivered via an isolated pulse stimulator (Model 2100, A-M SYSTEMS, Sequim, WA, USA). The recordings were acquired and analysed on-line using IGOR Pro software (Wavemetrics, Portland, OR, USA).

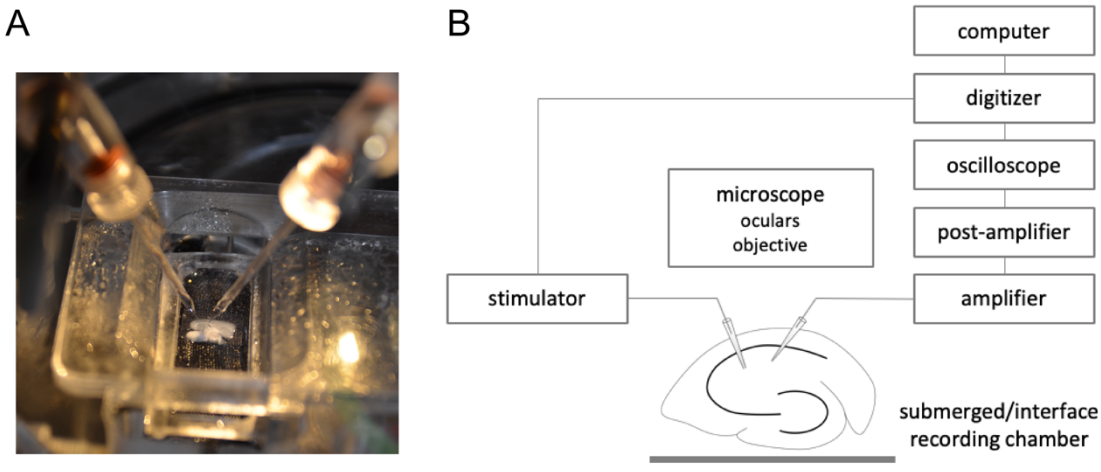

Figure 2.3 fEPSPs recordings setup. (A) Haas-type interface recording chamber

containing a hippocampal slice and the stimulating and recording electrodes. (B) Scheme of the fEPSPs recordings setup: a fEPSP potential amplifier was used to detect the electrical signal, and an isolated pulse stimulator was used to elicit the fEPSPs.

2.4.2 Electrodes

One mm thick glass capillaries (GB150F-8P, Science Products, Hofheim, Germany) were used to pull pipettes for stimulation (pipette resistance ~ 1-2 MΩ) and for recording (pipette resistance ~ 4-5 MΩ). The glass capillaries were pulled using a vertical puller (Model PP-830, Narishige, Setagaya, Tokyo, Japan). Stimulating and recording pipettes were filled with ACSF solution and placed in the stratum radiatum of the hippocampal CA1 region.

2.4.3 Experimental procedure

Schaffer collateral-evoked fEPSPs were measured in a submerged or Haas-type interface recording chamber. In the latter case, slices were incubated for one hour before the start of the measurement. To evoke fEPSPs, Schaffer collaterals were stimulated with current pulses of 200 µs duration and the stimulation intensity was adjusted to elicit maximal fEPSPs amplitude. The stimulation protocol was delivered every 30 seconds.

2.4.3.1 Fractional release Ca^{2+} curves

fEPSPs at the CA3-CA1 synapses were recorded in RIM1α KO, RIM3 KO, RIM4 KO, and wild-type (WT) mice. In each experiment, the slices were perfused with ACSF containing one of the different Ca^{2+} concentrations (in mM): 0.8, 1, 1.5, 2, 4, 10, or 20.

After 30 minutes of stable fEPSPs amplitude, one specific Ca^{2+} channel blocker diluted in the ACSF was bath-applied until a steady-state of the blocking effect was reached. 1 µM of Cgtx was applied for approx. 25 minutes. Agatx was applied for 10 minutes at 1 µM, followed by 20 minutes at 0.1 µM. Additionally, we evaluated the effect of the $GABA_A$ receptor inhibition on the excitatory synaptic transmission by bath-application of gabazine. The effect of 1 µM Cgtx on the fEPSPs amplitude was found to be similar in the presence and in the absence of 10 µM gabazine. Consequently, we performed further experiments without gabazine.

2.4.3.2 Paired-pulse facilitation

PPF was evaluated in RIM1α KO, RIM3 KO, RIM4 KO, and WT mice. The stimulation protocol consisted of two pulses of 200 µs with a 40 ms inter-stimulus interval.

2.4.3.3 Effect of the Ca^{2+} chelator EGTA-AM

The effect of the Ca^{2+} chelator EGTA on Schaffer collateral-evoked fEPSPs was analyzed in RIM1α KO and WT mice. We used a cell-permeable version of EGTA, EGTA-AM. The slices were perfused with sACSF. After 30 minutes of stable fEPSPs amplitude, 100 µM EGTA-AM was bath-applied for 15 minutes in the presence of 175 µM probenecid (Probenecid water soluble, Thermo Fisher Scientific, Waltham, MA, USA), 70 µM 2-hydroxypropyl-β-cylcodextrin (HBC; SIGMA, St. Louis, MO, USA) and 0.1% DMSO containing 20% pluronic F-127. In order to avoid foam formation, the Ca^{2+} chelator solution was not gassed with O_2/CO_2 during the bath-application. The sACSF used to prepare this solution was carbogen-saturated (95% O_2, 5% CO_2) before application, assuring a proper pH buffering via the sodium bicarbonate. EGTA-AM was initially dissolved in DMSO 20% pluronic, as stock solution and diluted with sACSF by a factor of 1000 to its final concentration before each experiment.

2.4.3.4 Effect of Cgtx on Et(iCre)-tdTomato-cDKO

To target RIM1αβ and RIM2αβγ deletion selectively to Schaffer collateral pathway, we employed a mouse line expressing Cre recombinase under a specific promoter of CA3 pyramidal cells (Et-iCre). The mouse strain used for this research project, B6(129S)-Et(icre)21614Rdav/J, RRID:MMRRC_034580-MU, was obtained from the Mutant Mouse Resource and Research Center (MMRRC) at University of Missouri, an NIH-funded strain repository, and was donated to the MMRRC by Ronald L Davis, The Scripps Research Institute. Paul Overbeek, Ph.D., Baylor College of Medicine. The lab of Prof. Dr. Susanne Schoch initially crossed this line to a Cre-reporter line which expresses tdTomato. Subsequently, they crossed the et(iCre)-tdTomato line to the cDKO RIM1$\alpha\beta^{fl/fl}$ and RIM2$\alpha\beta\gamma^{fl/fl}$ mouse line (Kaeser et al., 2011) generating the Et(iCre)-tdTomato-cDKO. fEPSPs at the Schaffer collateral pathway were

recorded from Cre recombinase negative mice, which retain RIM expression, and from Cre recombinase positive mice, referred to as cDKO mice. The slices were perfused with sACSF and after 30 minutes of stable fEPSPs, 1 µM of Cgtx was applied for approx. 25 minutes.

2.4.4 Analysis of fEPSPs

Data were analyzed with built-in and custom-made macros in IGOR Pro and Excel (Microsoft, Redmond, Washington, USA).

2.4.4.1 Fractional release Ca^{2+} curves

The maximal amplitude of the fEPSPs in the dendrites was measured. The amplitude of fEPSPs was calculated from the baseline immediately preceding the stimulation to the maximum negative deflection. The fractional fEPSPs amplitude remaining after the Ca^{2+} channel blocker application was calculated with the following formula:

$$\text{frac. fEPSP ampl. } (\%) = \left(\frac{\text{fEPSP}_{\text{Cgtx or AgaTx}}}{\text{fEPSP}_{\text{control}}}\right) * 100 \quad (3)$$

$fEPSP_{control}$ and $fEPSP_{Cgtx\ or\ AgaTx}$ maximum amplitudes were calculated from averaging 20 fEPSPs traces prior to and after toxin application, respectively. The fractional fEPSPs amplitudes, remaining after toxin application, were plotted against the relative changes in the local Ca^{2+} concentration reached at the release sensor during an AP (see 3.2.1).

2.4.4.2 Paired-pulse facilitation

The maximal amplitudes of both fEPSPs were calculated from the baselines immediately preceding each stimulation pulse. The paired-pulse ratio was calculated by the formula:

$$\text{PPF } (\%) = \left(\frac{\text{fEPSP}_2}{\text{fEPSP}_1}\right) * 100 \quad (4)$$

$fEPSP_1$ and $fEPSP_2$ maximum amplitudes were calculated from averaging twenty fEPSPs traces.

2.4.4.3 Effect of EGTA-AM

The maximal amplitude of fEPSPs was calculated from the baseline immediately preceding the stimulation. The fractional fEPSP amplitude remaining after EGTA-AM application was calculated with the following formula:

$$\text{frac. fEPSP ampl. (\%)} = \left(\frac{\text{fEPSP}_{\text{EGTA}}}{\text{fEPSP}_{\text{control}}}\right) * 100 \quad (\mathbf{5})$$

$fEPSP_{control}$ maximum amplitudes were calculated from averaging 20 fEPSPs traces right before the Ca^{2+} chelator application. $fEPSP_{EGTA}$ amplitudes were calculated 20 minutes after the start of the EGTA-AM perfusion and averaging 10 fEPSPs traces.

2.4.4.4 Analysis of fEPSPs kinetics

We evaluated three parameters: the delay of the release, which is the time between the peak of the presynaptic fiber volley and the 20% maximum fEPSPs amplitude; the 20-80% fEPSPs rise time, and the tau of the fEPSPs decay phase. Schaffer collateral-evoked fEPSPs kinetics was evaluated in RIM1α KO and WT mice under 2, 4, and 20 mM $[Ca^{2+}]_e$.

2.5 Evoked excitatory postsynaptic currents

We evaluated the effect of Cgtx on EPSC recorded from CA1 hippocampal pyramidal neurons.

2.5.1 Setup

For EPSCs recordings, horizontal hippocampal slices (300 µm thickness) were placed in a submerged recording chamber, and positioned in a fluorescence microscope (ECLIPSE E600FN, Nikon, Shinagawa, Tokyo, Japan). Signals were amplified with a patch clamp amplifier EPC 7 (Heka, Holliston, MA, USA) and a postamplifier BF-48DGX (npi electronic GmbH, Tamm, Germany). Signals were filtered at 1 kHz and digitized with a sampling frequency of 10 kHz (NI USB-6229 National Instruments, Austin, TX, USA). Recordings were monitored on-line with an oscilloscope (Tektronix DPO 2024B Digital Phosphor Oscilloscope, Beaverton,

Oregon, USA). Stimulation was delivered via an isolated pulse stimulator (Model 2100, A-M SYSTEMS, Sequim, WA, USA). The recordings were operated using IGOR Pro software.

2.5.2 Electrode

One mm thick glass capillaries were used to pull pipettes for stimulation, as for fEPSPs recordings, and for recording (pipette resistance approx. 5-6 MΩ). The glass capillaries were pulled using a vertical puller. The stimulating pipette was filled with ACSF and the recording pipette was filled with intracellular solution (see 2.2.2). The stimulating pipette was placed in the stratum radiatum of the hippocampal CA1 region.

2.5.3 Experimental procedure

EPSCs were recorded from RIM1α KO slices, while perfusing 1 mM $[Ca^{2+}]_e$, and from WT slices, while perfusing 2 mM $[Ca^{2+}]_e$. The sACSF contained 10 µM of gabazine. Whole-cell patch-clamp recordings were performed in CA1 pyramidal cells at room temperature. Cells were held at -70 mV.

During the whole-cell patch-clamp technique, under visual control, the recording pipette was positioned close to the optically selected CA1 pyramidal cell. A tight seal, at least 1 GΩ, was formed between the cell and the patch electrode. The membrane was ruptured by suction so that the glass electrode provides a low-resistance access to the cell. The access resistance (R_a) was monitored during the entire duration of the recording. Cells were discarded when R_a values were larger than 20 MΩ. EPSC were elicited by Schaffer collateral stimulation placing the stimulating electrode in the stratum radiatum of the CA1 region. Stimulation pulses of 200 µs and an intensity adjusted to elicit maximal amplitude, were delivered every 15 seconds. After 20 minutes stable EPSC amplitude 1 µM of Cgtx was applied.

2.5.4 Analysis

The effect of Cgtx on EPSC was analyzed with built-in and custom-made macros in IGOR Pro. The maximal amplitude of EPSCs was calculated from the baseline

immediately preceding the stimulation. The fractional EPSCs amplitude remaining after the Cgtx, was calculated with the following formula:

$$\text{frac. EPSC ampl. (\%)} = \left(\frac{\text{EPSC}_{\text{Cgtx}}}{\text{EPSC}_{\text{control}}}\right) * 100 \quad (6)$$

$EPSC_{control}$ and $EPSC_{Cgtx}$ maximum amplitudes were calculated from averaging 20 EPSC traces prior to and after toxin application, respectively.

2.6 Miniature excitatory postsynaptic currents

Due to the stochastic nature of neurotransmitter release, single synaptic vesicles can be released in the absence of presynaptic activity. The release of one single quantum generates a miniature postsynaptic current, for instance, a mEPSC. mEPSCs are detected in the presence of a voltage-gated Na^+ channel blocker, tetrodotoxin (TTX), which inhibits neuronal firing.

2.6.1 Experimental procedure

mEPSCs were recorded in RIM1α KO, RIM4 KO, and WT mice. The setup and recording electrode used for mEPSCs recordings were the same as for EPSCs. The slices were perfused with sACSF containing 10 µM of gabazine and 1 µM of TTX. Whole-cell patch-clamp recordings were performed in CA1 pyramidal cells at room temperature. Cells were held at -70 mV. The cell R_a was monitored during the whole experiment and cells were discarded if the values were larger than 20 MΩ. mEPSCs were recorded for 10-second cycles, with one-second pauses in between, for 20 minutes maximum.

2.6.2 mEPSCs detection and analysis

mEPSCs offline detection and analysis were performed using AxoGraph software (Axon Instruments, Foster City, CA, USA). mEPSC events were detected automatically by an optimally scaled template. The template function had an idealized synaptic event width and time course consisting of an exponential rise and decay. The template was generated by averaging 10 mEPSCs selected initially by eye. A detection criterion or threshold was calculated based on the template scaling

factor, and on the goodness-of-fit between the template and the data. A mEPSC event was detected when this criterion was larger than 3 times the standard deviation (SD) of the noise. To select events with a negative amplitude, as mEPSCs, a negative criterion, that is -3, needs to be used (Clements and Bekkers, 1997). After mEPSCs detection, events with a rise time larger than 5 ms were rejected. The rise time is defined as the time from 20 to 80% of the mEPSC amplitude. Events with a half-width smaller than 3 ms or larger than 50 ms were also rejected. The half-width is defined as the time between the rising and decay phases of each mEPSC at 50% of the peak amplitude.

After the mEPSC event selection, we used IGOR Pro software in order to calculate the mean event amplitude (pA) and the event frequency (Hz), defined as the reciprocal of the average inter-event interval (IEI). We also calculated kinetic parameters: the 20-80% rise time, and the time constant of decay (τ).

2.7 Presynaptic Ca^{2+} imaging in the Schaffer collaterals

Neurotransmitter release is initiated by Ca^{2+}. During an AP, Ca^{2+} entry through presynaptic VGCCs raises the $[Ca^{2+}]_i$ to levels that can be even 100 times higher. Ca^{2+} imaging techniques allow us to monitor the dynamics of Ca^{2+} at the presynaptic terminals.

We recorded intracellular Ca^{2+} signals from a neuronal population by bulk dye-loading of a membrane-permeable AM ester Ca^{2+} dye. Through application of VGCC blockers, we aimed to quantify the contribution of the different types of presynaptic VGCCs to the I_{Ca}.

2.7.1 Loading of AM ester Ca^{2+} indicator dye into Schaffer collaterals

For monitoring presynaptic Ca^{2+} transients, we performed acute network labeling by AM loading into horizontal hippocampal slices (300 µm thickness). We used the low-affinity cell-permeant Ca^{2+} indicator Mg-Green AM. This low-affinity Ca^{2+}-sensitive fluorescence indicator, K_d= 7 µM (Zhao et al., 1996), accurately reflects the change in the presynaptic Ca^{2+} concentration.

A loading pipette, containing the labeling solution (see 2.2.3), was placed into the border of the CA3-CA1 field. Mg-Green AM was injected by means of an air pressure pulse to the brain tissue, resulting in a stained area with a diameter of 300-500 µm (Figure 2.4). The carboxylate groups of the Ca^{2+} indicator are derivatized as AM esters, resulting in a nonpolar compound that is permeable to cell membranes. Once inside the cell, the lipophilic blocking groups are cleaved by nonspecific esterases, resulting in a charged indicator for the recognition of Ca^{2+}, which is trapped inside the cell.

After 30 minutes of loading, the labeling pipette was removed. Next, the stimulating glass electrode was placed in the CA1 stratum radiatum in order to elicit presynaptic Ca^{2+} transients.

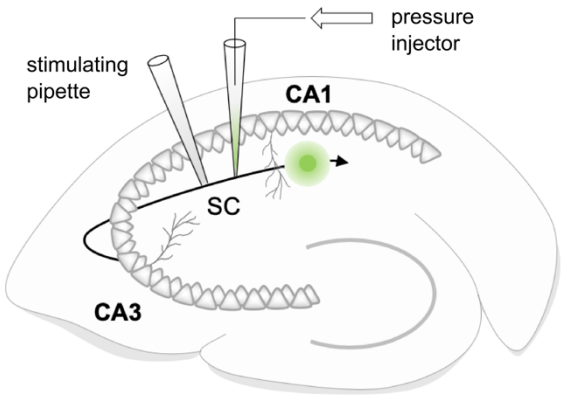

Figure 2.4 Scheme of the AM-dye bulk loading into the Schaffer collaterals. The membrane permeable Ca^{2+} indicator (Mg-Green AM) was pressure injected under visual control into the stratum radiatum. Ca^{2+} transients were elicited by a stimulating electrode placed also in the stratum radiatum.

2.7.2 Setup

For imaging of intraterminal Ca^{2+} transients, hippocampal slices were placed in a submerged recording chamber positioned in a fluorescence microscope (ECLIPSE E600FN, Nikon, Shinagawa, Tokyo, Japan). The slices were perfused with sACSF.

A LED lamp (OptoLED, Cairn Research, Faversham, Kent, UK) with 470 nm wavelength was used to excite the Ca^{2+} indicator. Mg-Green AM exhibits a fluorescence emission peak ~ 530 nm. Excitation and emission light are separated by a dichroic beam splitter unit (model DCXRUV, AHF Analysetechnik AG,

Tübingen, Germany). The band-pass filtered fluorescence (530 ± 43 nm, AHF Analysetechnic AG, Tübingen, Germany) was detected by a photodiode (Till Photonics GmbH, Gräfelfing, Germany) through a 60x objective (60x Fluor, DIC H, NA 1.00, WD 2.0, Nikon, Shinagawa, Tokyo, Japan) and monitored by a charge-coupled device (CCD)-based camera (FK 7512 IQ, Pieper GmbH, Schwerte, Germany). Signals were amplified by the voltage converter unit (Till Photonics GmbH, Gräfelfing, Germany). Recordings were monitored on-line with an oscilloscope (Tektronix DPO 2024B Digital Phosphor Oscilloscope, Beaverton, Oregon, USA). Stimulation protocols were delivered via an isolated pulse stimulator (Model 2100, A-M SYSTEMS, Sequim, WA, USA). The recordings were analyzed on-line using IGOR Pro software.

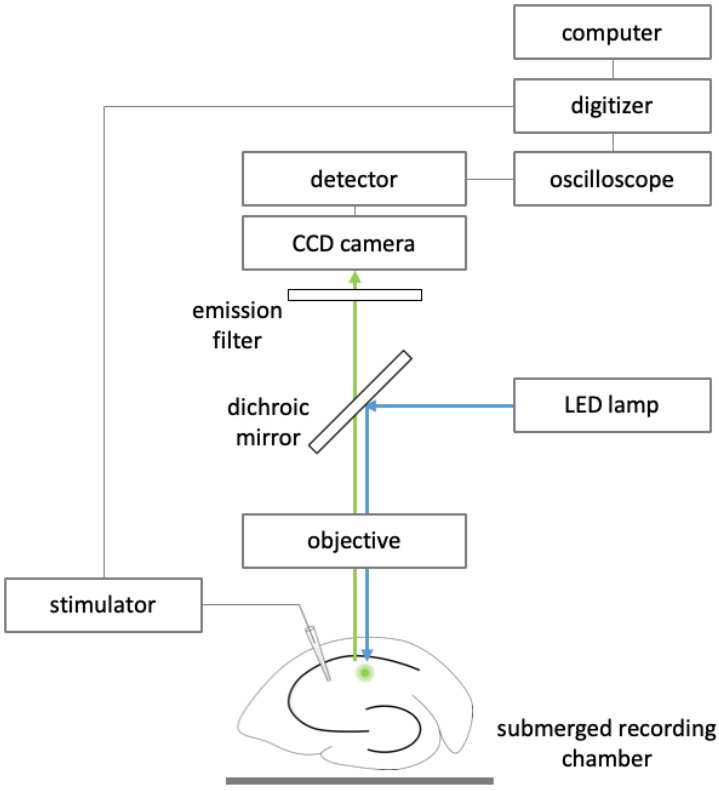

Figure 2.5 Ca^{2+} imaging setup. An LED lamp was used as a light source; the excitation and emission light were separated by a dichroic mirror, and the fluorescence was detected with a photodiode; and an isolated pulse stimulator was used to elicit the Ca^{2+} transients.

2.7.3 Electrodes

One mm thick glass capillaries were used to pull pipettes for loading (pipette resistance ~ 4-5 MΩ) and stimulation (pipette resistance ~ 1-2 MΩ). The glass capillary was pulled using a vertical puller. The loading pipette was filled with the labeling solution and the stimulating pipette with sACSF.

2.7.4 Experimental procedure

Presynaptic Ca^{2+} transients at hippocampal CA3-CA1 synapses were measured in a submerged recording chamber. In order to evoke AP-mediated Ca^{2+} transients, the stimulating electrode was placed in the stratum radiatum of the hippocampal CA1 region, parallel to the Schaffer collaterals. Stimulation was carried out with 200 µs current pulses and the stimulation intensity was adjusted to evoke a maximal increase in fluorescence intensity. The stimulation protocol was delivered every 30 seconds.

Presynaptic Ca^{2+} transients were recorded in RIM1α KO and WT mice. The slices were perfused with sACSF or sACSF without NaH_2PO_4, in case of posterior Ni^{2+} application, in the presence of 10 µM 6-cyano-7-nitroquinoxaline-2,3-dione (CNQX). After 30 minutes of stable presynaptic Ca^{2+} transients, specific VGCC blockers diluted in sACSF, containing 10 µM CNQX, were bath-applied until a steady-state of the blocking effect was reached.

The following Ca^{2+} channel blockers were individually bath-applied: 1 µM Cgtx, for approx. 25 minutes; 1 µM Agatx, for 10 minutes and 0.1 µM for 20 minutes; 1 µM SNX-482, a specific R-type VGCC blocker, for 10 minutes and 0.1 µM for 20 minutes. In order to elucidate the nature of the Cgtx-Agatx-insensitive Ca^{2+} transient fraction, the slices were simultaneously perfused with 100 µM Ni^{2+} and 10 µM verapamil. Those slices were initially preincubated for one hour in sACSF containing 2 µM Cgtx and 2 µM Agatx.

The collective contribution of the different presynaptic VGCCs to the AP-induced Ca^{2+} transients was evaluated by the combined bath-application of the VGCC toxins for 20 minutes: 1 µM Cgtx, 1 µM Agatx (0.1 µM for the last 10 minutes), 0.5 µM SNX-482, 100 µM Ni^{2+}, 10 µM verapamil, and 10 µM nimodipine, a specific L-type VGCC

blocker. All drugs were dissolved as stock solutions and diluted with sACSF at least by a factor of 100 to final concentrations before each experiment. All VGCC blockers were dissolved in water, except nimodipine, which was dissolved in DMSO.

2.7.5 Aperture

We defined a small imaging region, at least 500 µm from the injection site, where Mg-Green AM-labeled presynaptic buttons from Schaffer collaterals were located. The aperture was adjusted in order to get an imaging region of approximately 20 µm x 20 µm. For monitoring presynaptic Ca^{2+} transients, the aperture was positioned in front of the stimulation pipette. The aperture, the focal plane, and the stimulating electrode position were visually adjusted for each experiment to obtain best Ca^{2+} signal conditions.

2.7.6 Analysis of presynaptic Ca^{2+} transients

Data were analyzed with built-in and custom-made macros in IGOR Pro and Excel.

Data in each experiment were normalized to the baseline before light excitation. The amplitude of the AP-evoked Ca^{2+} transients was expressed as the ratio of the difference between the peak fluorescence (ΔF) and the baseline fluorescence (F).

The maximal amplitude of the Ca^{2+} transients was measured ($\Delta F/F$). The amplitude was calculated from the baseline immediately preceding the start of the transient. The fractional Ca^{2+} transient amplitude remaining after the VGCC blocker application was calculated with the following formula:

$$\mathrm{frac.}\,\Delta\mathrm{F/F(\%)} = \left(\frac{\Delta\mathrm{F/F_{blocker}}}{\Delta\mathrm{F/F_{control}}}\right) * 100 \qquad (7)$$

$\Delta F/F_{control}$ and $\Delta F/F_{blocker}$ maximum amplitudes were calculated from averaging 20 Ca^{2+} transients prior to and after toxin application, respectively. The reduction of the I_{Ca} by Ni^{2+} and verapamil was quantified by subtracting to 1 the Cgtx-sensitive and Agatx-sensitive fractions and multiplying by the effect of the Ni^{2+} and verapamil on the remaining Cgtx-Agatx-insensitive Ca^{2+} transients.

2.8 NMDAR-mediated EPSCs, IPSCs, and mIPSCs recordings in hippocampal cell cultures

Primary hippocampal neuronal cultures were prepared from new-born pups of RIM1/2 cDKO according to standard protocols (Zürner et al., 2011). The transductions were performed at 3-4 days in vitro (DIV) using lentiviruses expressing a non-active Cre-recombinase, an active Cre-recombinase, or a GFP-tagged active Cre-recombinase (Kaeser et al., 2011). Primary cultures and lentiviral particles were provided by Prof. Dr. Susanne Schoch's lab.

Whole-cell patch-clamp recordings were performed in cultured hippocampal neurons at DIV 14-16. The same setup as for EPSCs and mEPSCs recordings, was used. The recording pipettes had a resistance of 4-5 MΩ, and they were filled with intracellular solution (see 2.2.2).

2.8.1 Release probability as determined by progressive block of NMDA synaptic currents

For NMDAR-mediated EPSCs recordings, 10 µM gabazine and 20 µM CNQX were added to the extracellular solution (see 2.2.1). Cells were held at +40 mV, in order to remove the voltage-dependent block by Mg^{2+}. APs in presynaptic neurons were elicited with a concentric bipolar focal stimulation electrode. The stimulation was carried out with 200-400 µs current pulses and delivered every 10 seconds. The stimulation strength was adjusted in order to elicit the maxim amplitude of the NMDAR-mediated EPSCs. The stimulation protocol was conducted for 5 to 10 minutes in order to obtain a baseline response. Afterwards, the stimulation was halted for five minutes, while 40 µM of MK-801 was added via bath-application and the MK-801 concentration equilibrated through the coverslip. The stimulation was resumed after those five minutes and the NMDAR-mediated EPSCs were recorded in the continuous presence of MK-801 until a steady-state was reached.

2.8.2 Time course of release rate as determined by deconvolution

In order to obtain the time course of the release rate, IPSCs and mIPSCs were recorded in the same cultured hippocampal neuron. 10 µM CNQX and 50 µM D-APV

were added to the extracellular solution (see 2.2.1). Cells were held at -80 mV. IPSCs were elicited by a concentric bipolar focal electrode. A single stimulation pulse, of 200-400 μs, was delivered every 15 seconds. After recording 20 IPSCs, 1 μM TTX was added to the extracellular solution in order to record mIPSCs. Five minutes after the start of the TTX perfusion, mIPSCs were recorded for 10-second cycles, with one-second pauses in between, for 20 minutes maximum.

In order to perform the IPSCs deconvolution, on one hand, mIPSCs were offline detected as described for mEPSCs in CA1 pyramidal cells (see 2.6.2), and all selected events were used to create an average mIPSC. And on the other hand, from the 20 recorded IPSCs, an average IPSC response was calculated.

The deconvolution approach was executed using the IGOR Pro software.

3 Results

3.1 Impaired neurotransmitter release in RIM1α-deficient synapses

Many modulators of synaptic transmission, such as AZ proteins, influence the synaptic strength, and therefore, synaptic plasticity. The temporal pattern of neurotransmitter release can be modulated by the basal P_r and by the number of SVs available for release at the nerve terminal. As AZ proteins, we expected RIM proteins to modulate at presynaptic level fast synaptic transmission. We evaluated RIM1α's function, shown to be essential for maintaining P_r and for regulating release during STP (Schoch et al., 2002), and RIM4.

3.1.1 Unaltered spontaneous release in RIM1α KO and RIM4 KO mice

To elucidate if the ablation of the RIM isoforms altered synaptic transmission at the presynaptic or at the postsynaptic level, we first performed in WT, RIM1α KO, and RIM4 KO mice, whole-cell patch clamp recordings of CA1 pyramidal cells. Measurements of mEPSCs showed that the amplitude of the miniature events did not differ between WT and RIM1α KO mice, indicating an unchanged quantal size, i.e. intact postsynaptic responsiveness to the neurotransmitter release. The overall frequency of mEPSCs in RIM1α KO was unchanged, although there was a trend towards a decreased frequency. The cumulative distribution of the mEPSC events revealed a decreased number of mEPSCs with a shorter IEI (Figure 3.1). These results support the idea that the deficit in synaptic output observed previously in RIM1α KO mice is not due to a deficit in the synapse number, nor in the postsynaptic response. The decreased synaptic output observed during AP-mediated neurotransmitter release is likely due to a lower P_{ves} or a decrease in the availability of SVs for release. Although P_{ves} and the number of release-ready state SVs are involved in any form of neurotransmitter release, the mechanisms regulating evoked release may differ from the mechanisms regulating spontaneous release.

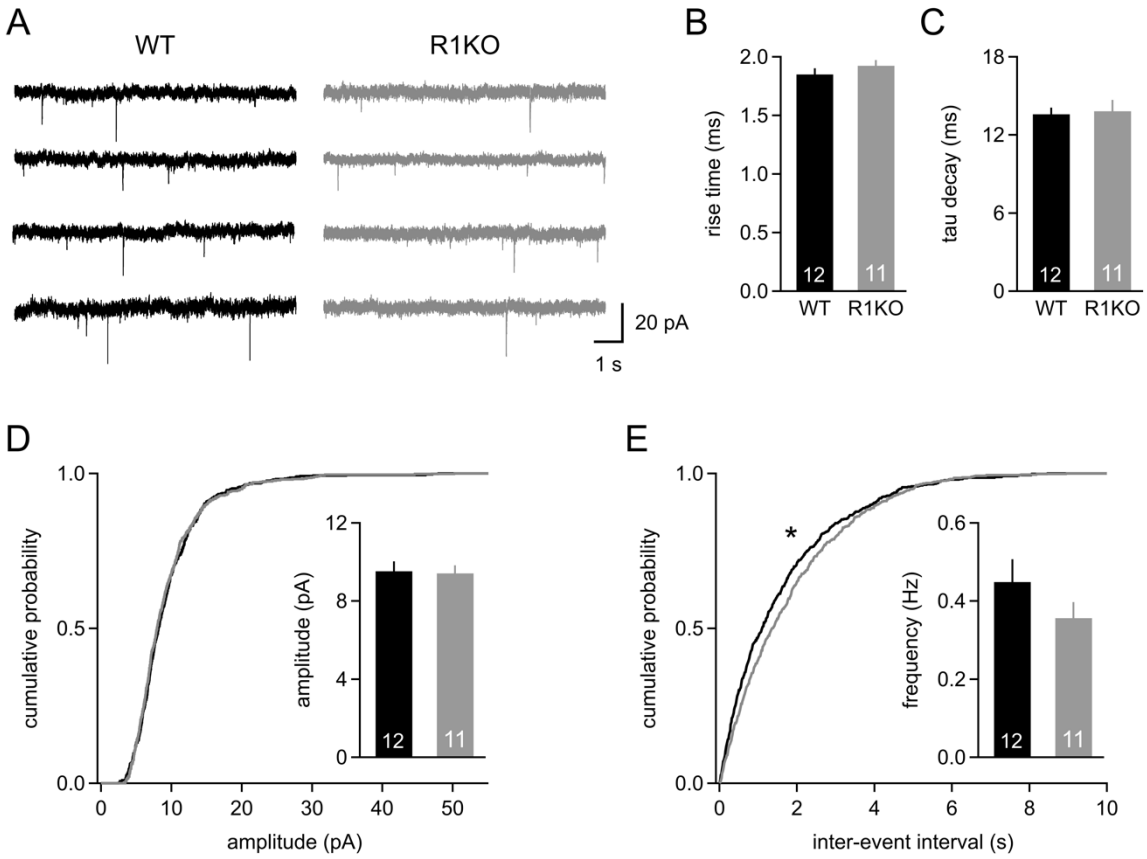

Figure 3.1 Miniature synaptic transmission is unaltered in RIM1α KO mice. mEPSCs were recorded in CA1 pyramidal cells from WT (black) and RIM1α KO mice (grey). Cumulative distribution functions (CDF) were constructed using 50 randomly selected events from each cell. The bar graphs depict the data as means ± standard error of the mean (SEM). The number of cells/mice is WT=12/8, and RIM1α KO=11/10. (A) Sample traces of mEPSCs. (B) mEPSCs rise time, WT 1.85 ± 0.05, and RIM1 KO 1.92 ± 0.05. (C) mEPSCs time constant of decay, WT 13.6 ± 0.5, and RIM1 KO 13.8 ± 0.9. (D) CDF of mEPSCs amplitude; inset displays bar graph for mEPSCs amplitude, WT 9.52 ± 0.5, and RIM1 KO 9.42 ± 0.4. (E) CDF of mEPSCs frequency, as measured by the IEIs; inset displays bar graph for mEPSCs frequency, WT 0.45 ± 0.06, and RIM1 KO 0.35 ± 0.04. Statistical significance was assessed by unpaired Student's t-test for the bar graphs and by Kolmogorov-Smirnov test for the CDFs (* $p < 0.05$).

mEPSC recordings in RIM4 KO mice were the first attempt to study the functional role of RIM4 in synaptic transmission. Neither the *q* nor the mEPSCs frequency was altered in CA1 pyramidal cells after the ablation of RIM4 (Figure 3.2). The kinetics parameters of the quantal events of RIM1α KO and RIM4 KO mice were unchanged.

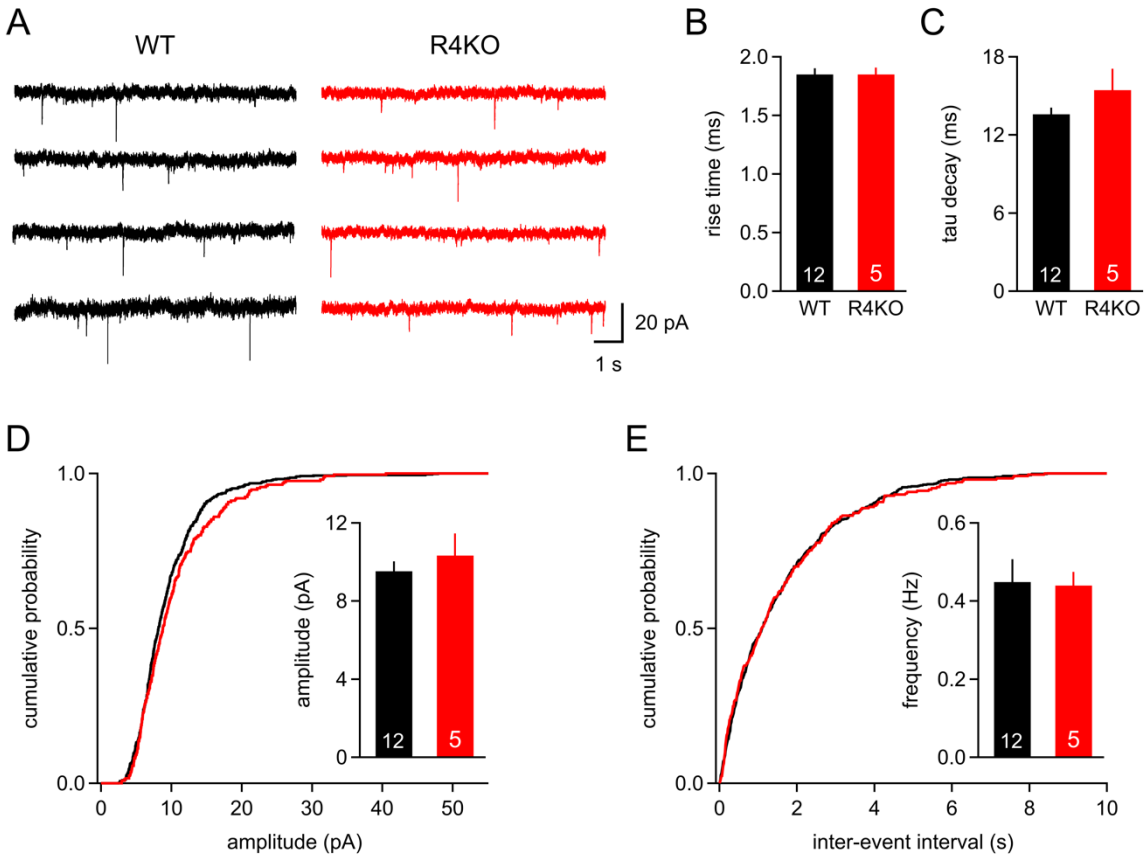

Figure 3.2 Unchanged spontaneous release in RIM4 KO mice. mEPSCs were recorded in CA1 pyramidal cells from WT (black) and RIM4 KO (red) mice. Cumulative distribution functions (CDF) and bar graphs are built as in figure 3.1. The number of cells/mice is WT=12/8, and RIM4 KO=5/4. (A) Sample traces of mEPSCs. (B) mEPSCs rise time, RIM4 KO 1.85 ± 0.06. (C) mEPSCs time constant of decay, RIM4 KO 15.4 ± 1.6. (D) CDF of mEPSCs amplitude; inset displays bar graph for mEPSCs amplitude, RIM4 KO 10.33 ± 1.1. (E) CDF of mEPSCs frequency, as measured by the IEIs; inset displays bar graph for mEPSCs frequency, RIM4 KO 0.44 ± 0.03. Statistical significance was assessed by unpaired Student's t-test for the bar graphs and by Kolmogorov-Smirnov test for the CDFs (* $p < 0.05$). WT data are the same as presented in figure 3.1.

3.1.2 Altered short-term synaptic plasticity in RIM1α KO mice

Short-term synaptic plasticity is primarily a presynaptic phenomenon, the activation of a synapse at short intervals results in a presynaptic facilitation of transmitter release in response to a second stimulus. Short-term plasticity is frequently assessed by the paired-pulse ratio. We measured PPF at the excitatory synapses between the hippocampal CA3 and CA1 pyramidal cells, a facilitating synapse, in WT, RIM1α, RIM3, and RIM4 KO mice. We recorded fEPSPs in the stratum radiatum of the hippocampal CA1 region evoked by Schaffer collateral stimulation in acute

brain slices. PPF is expressed as a marked increment of the fEPSPs amplitude elicited by the second of two closely spaced stimuli (40 ms interval).

At first, in order to study whether the inhibitory neural network affected short-term synaptic plasticity at excitatory synapses, PPF was tested in the presence and in the absence of 10 µM of Gabazine, a competitive and selective $GABA_A$ receptor antagonist. The presence or absence of Gabazine did not affect PPF. Therefore, within each experimental group, we pooled data from experiments recorded with and without Gabazine. Furthermore, we evaluated PPF in WT mice from different lines: the three WT RIM lines and the C57BL/6 line. As for Gabazine, no difference in PPF was found between the different WT mice, allowing us to pool the data from all WT mice. The statistical significance was tested by two-way ANOVA (data not shown).

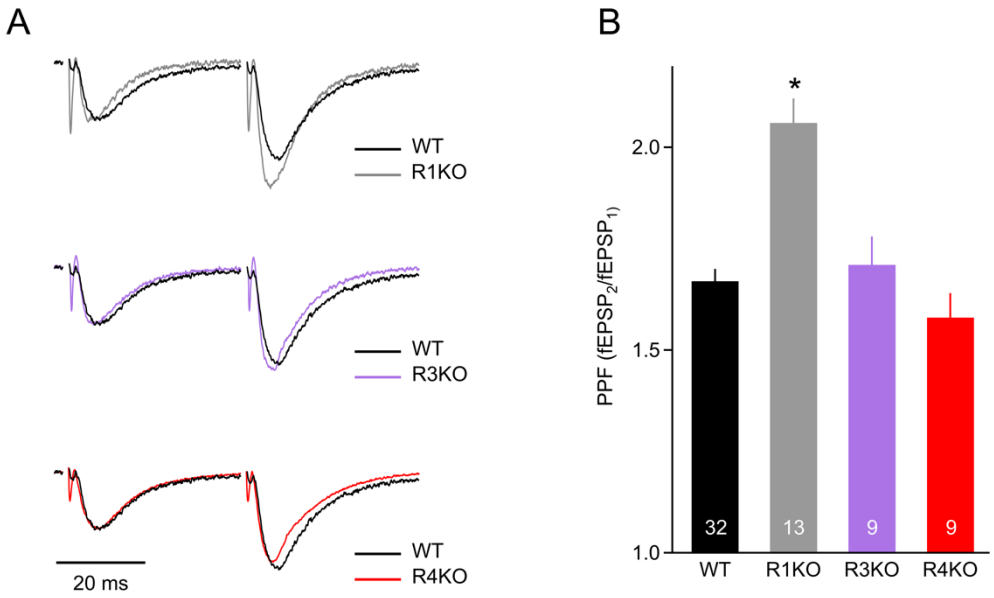

Figure 3.3 Increased short-term synaptic plasticity in RIM1α KO mice. (A) Representative traces for WT (black), RIM1α KO (grey), RIM3 KO (purple), and RIM4 KO (red) mice, normalized to the first fEPSP peak. (B) Bar graph displaying mean values ± SEM. WT 1.67 ± 0.03, RIM1 KO 2.06 ± 0.06, RIM3 KO 1.71 ± 0.07, and RIM4 KO 1.58 ± 0.06. Statistical significance between WT data and each KO data was evaluated by Student´s t-test (* p-value < 0.05).

Compared to WT mice, RIM1α KO mice displayed larger PPF (Figure 3.3), whereas PPF values for RIM3 and RIM4 KO mice were similar to PPF WT values. This alteration of the short-term synaptic plasticity in RIM1α KO mice agrees with a basal

lower P_r. It is unclear whether this alteration is primarily due to an altered P_{ves}, to a disturbed signalling of Syt7, or to a decrease in the very Ca^{2+}concentration operating the Ca^{2+} sensor of release.

3.2 The Ca^{2+} signal at the release machinery Ca^{2+} sensor is tuned by RIM1α

In order to elucidate the origin of the impaired neurotransmitter release in RIM1α KO mice as well as to shed light in a putative role for RIM3 and RIM4 controlling neurotransmitter release at the presynaptic level, we examined the Ca^{2+} signal built at the Ca^{2+} microdomain near docked SVs after an AP. Using fEPSP recordings and specific VGCC blockers as experimental components, and the simple power-law-description of the Ca^{2+}-dependence of release, being approximated by $(I_{Ca})^n$, as theoretical background, we developed a novel approach which promised to be of general use in assessing several aspects of the AP-mediated presynaptic Ca^{2+} signal, like the relative contribution of the different VGCC types to neurotransmitter release, the Ca^{2+}-binding parameters to the Ca^{2+} sensors located at the release machinery, as the Ca^{2+} affinity and the Ca^{2+} cooperativity, and the relative P_{ves}.

3.2.1 Mathematical approach to analyze the Ca^{2+} signal at the release machinery Ca^{2+} sensor

As extensively explained during the introduction, the steep Ca^{2+} cooperativity during an AP makes synaptic transmission extremely sensitive to changes in the Ca^{2+} concentration at the release site ($[Ca^{2+}]_{local}$).

Our mathematical approach built upon the fact that AP-induced Ca^{2+} binding to the Ca^{2+} sensor of the release machinery can be brought near to saturation when perfusing high $[Ca^{2+}]_e$. This scenario of “near-saturation” of Ca^{2+} sensors renders synaptic transmission insensitive to partial reduction of I_{Ca} (Wheeler et al., 1994). We employed fEPSP amplitudes from recordings at the Schaffer collaterals to CA1 pyramidal neuron (Sc-CA1) synapses as a readout for transmitter release. To alter the $[Ca^{2+}]_{local}$, we perfused a wide range of different $[Ca^{2+}]_e$ and used specific VGCC blockers, Cgtx and Agatx, which reduce I_{Ca} to a certain and constant fraction. After VGCC toxin application, we could quantify the resulting relative decrease on the

fEPSP amplitude. This relative decrease of synaptic release depends on the saturation level of the Ca^{2+} sensor at the release machinery: at elevate $[Ca^{2+}]_{local}$, achieved perfusing high $[Ca^{2+}]_e$, the release machinery is near saturation and therefore, the relative decrease in synaptic transmission by the specific VGCC toxins is reduced; on the contrary, at low $[Ca^{2+}]_{local}$, achieved perfusing low $[Ca^{2+}]_e$, the release machinery is far from saturation, and the relative decrease in release is more pronounced (Figure 3.4).

Non-linear relationship between $[Ca^{2+}]_{local}$ and release

We examined the role of Ca^{2+} during AP-induced transmitter release by a Hill equation describing the cooperative Ca^{2+}-binding scheme. The transmitter release resulting from such binding scheme at various $[Ca^{2+}]_e$ can be fitted by a Hill equation with apparent cooperativity (n_{app}) lower than n.

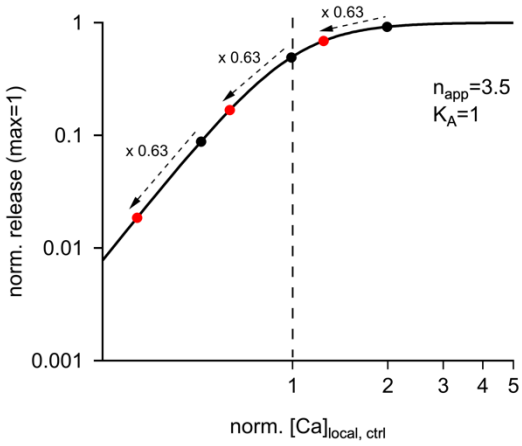

$$\text{release} = \frac{[Ca^{2+}]_e^{\,n_{app}}}{[Ca^{2+}]_e^{\,n_{app}} + K_A^{\,n_{app}}} \quad (8)$$

Figure 3.4 Ca^{2+}-dependence synaptic transmission inhibition. Plot of equation (8). n_{app} equal to 3.5, and K_A equal to 1. The $[Ca^{2+}]_{local}$ is normalized on that concentration achieved during an AP under control conditions, 2 mM $[Ca^{2+}]_e$. The degree of inhibition of transmitter release depends on the saturation level of the Ca^{2+} sensor at the release machinery, i.e. the horizontal position of the black dots.

(8), K_A indicates the Ca^{2+} concentration leading to half-maximal Ca^{2+} sensor occupancy and therefore, half-maximal neurotransmitter release; and, n_{app} indicates the degree of the Ca^{2+} cooperativity.

Estimation of $[Ca^{2+}]_{local}$ by means of $[Ca^{2+}]_e$ and I_{Ca}

To estimate normalized I_{Ca} from the $[Ca^{2+}]_e$, we employed a calibration procedure based on several previous measurements of I_{Ca} through VGCCs. I_{Ca} is well fitted by a function for a bimolecular reaction scheme describing the Ca^{2+} channel pore occupancy by the $[Ca^{2+}]_e$ with a K_D, dissociation constant of the Ca^{2+} binding site, being 3.3 mM (Carbone and Lux, 1987, Erdmann et al., 2012, Mintz et al., 1995).

$$\mathrm{norm.\,I_{Ca}} = \frac{2.7 * \ [\mathrm{Ca^{2+}}]_e}{([\mathrm{Ca^{2+}}]_e + \ 3.3)} \tag{9}$$

Changes in the I_{Ca}, by changes in the $[Ca^{2+}]_e$, must be converted into the respective relative changes of the $[Ca^{2+}]_{local}$. Previous studies showed that the $[Ca^{2+}]_{local}$ is over a large range of conditions proportional to the I_{Ca} (Erdmann et al., 2012); therefore, the output of equation (9), sufficiently describes relative changes in the $[Ca^{2+}]_{local}$ at the release sensor. Consequently, we could rewrite equation

(**8**) in terms of normalized I_{Ca} or, directly, normalized $[Ca^{2+}]_{local}$.

$$\mathrm{release} = \frac{\mathrm{norm.}\,[\mathrm{Ca^{2+}}]_{\mathrm{local}}{}^{\mathrm{n_{app}}}}{\mathrm{norm.}\,[\mathrm{Ca^{2+}}]_{\mathrm{local}}{}^{\mathrm{n_{app}}} + (\mathrm{b} * \mathrm{norm.\,K_A})^{\mathrm{n_{app}}}} \tag{10}$$

In equation (10), the previous parameter K_A was separated in two factors: *b* and *norm.* K_A. As a whole, the element (*b* **normalized* K_A) states how much the $[Ca^{2+}]_{local}$ has to be increased with respect to the condition of 2 mM $[Ca^{2+}]_e$ in order to achieve half-maximal occupancy of the Ca^{2+} sensor. The factor *norm.* K_A reports changes in the biochemical affinity of the Ca^{2+} sensor, and the factor *b*, changes in the $[Ca^{2+}]_{local}$ seen by the Ca^{2+} sensor. The factor *b* indicates modifications of $[Ca^{2+}]_{local}$ which can be caused by an alteration in the number of tethered VGCCs at the release site or in their distance relative to the docked SVs where the Ca^{2+} sensors are located. (The distinction between *norm.* K_A and *b* is a key consideration during the analysis of our data).

VGCCs mediating neurotransmitter release: P/Q-type and N-type

At the Sc-CA1 synapses, neurotransmitter release is mainly mediated by two types of VGCCs: P/Q-type and N-type. In other words, the I_{Ca} at those synapses relies on the contribution of the P/Q-type VGCCs (fraction *P*) and the contribution of the N-

type VGCCs (fraction *N*). As we could not discard completely the possibility of other types of VGCCs contributing to the I_{Ca} at the Schaffer collaterals, apart from *P* and *N*, a possible contribution of remaining VGCCs, which are not blocked by Agatx neither Cgtx, had to be taken into account. This contributing factor was defined as fraction *R* (remaining VGCCs). To reflect that each VGCC subtype is contributing a certain fraction to the I_{Ca} we defined:

$$\mathrm{P} + \mathrm{N} + \mathrm{R} = 1 \tag{11}$$

Consequently, we could re-express equation (10) as:

$$\mathrm{release} = \frac{((\mathrm{P}+\mathrm{N}+\mathrm{R}) * \ \mathrm{norm.}\,[\mathrm{Ca}^{2+}]_{\mathrm{local}})^{\mathrm{n_{app}}}}{((\mathrm{P}+\mathrm{N}+\mathrm{R}) * \ \mathrm{norm.}\,[\mathrm{Ca}^{2+}]_{\mathrm{local}})^{\mathrm{n_{app}}} + (\mathrm{b} * \mathrm{norm.}\,\mathrm{K_A})^{\mathrm{n_{app}}}} \tag{12}$$

Inhibitory effect on Sc-CA1 fEPSPs caused by Cgtx and Agatx

We employed as a readout of neurotransmitter release, fEPSP recordings. After VGCC toxin application (Cgtx or Agatx), we could quantify the resulting relative decrease of the fEPSP amplitude. In the presence of Cgtx, the specific N-type VGCC blocker, the I_{Ca}, and ergo $[Ca^{2+}]_{local}$, is explained by the contribution of P/Q-type VGCCs and the contribution of Cgtx-Agatx-insensitive channels:

$$\mathrm{norm.}\,\mathrm{I_{Ca}}(\mathrm{Cgtx}) = (\mathrm{P}+\mathrm{R}) * \mathrm{norm.}\,\mathrm{I_{Ca}} \tag{13}$$

The resulting fractional relative release in the presence of Cgtx, given by diving the release in the presence of Cgtx by the release prior to toxin application, can be expressed as:

$$\begin{aligned} &\mathrm{fract.\,rel.\,Cgtx} \\ &= \frac{((\mathrm{P}+\mathrm{R}) * \ \mathrm{norm.}\,[\mathrm{Ca}^{2+}]_{\mathrm{local}})^{\mathrm{n_{app}}}}{((\mathrm{P}+\mathrm{R}) * \ \mathrm{norm.}\,[\mathrm{Ca}^{2+}]_{\mathrm{local}})^{\mathrm{n_{app}}} + (\mathrm{b} * \mathrm{norm.}\,\mathrm{K_A})^{\mathrm{n_{app}}}} \\ &/ \frac{((\mathrm{P}+\mathrm{N}+\mathrm{R}) * \ \mathrm{norm.}\,[\mathrm{Ca}^{2+}]_{\mathrm{local}})^{\mathrm{n_{app}}}}{((\mathrm{P}+\mathrm{N}+\mathrm{R}) * \ \mathrm{norm.}\,[\mathrm{Ca}^{2+}]_{\mathrm{local}})^{\mathrm{n_{app}}} + (\mathrm{b} * \mathrm{norm.}\,\mathrm{K_A})^{\mathrm{n_{app}}}} \\ &= \frac{((\mathrm{P}+\mathrm{R}) * \ \mathrm{norm.}\,[\mathrm{Ca}^{2+}]_{\mathrm{local}})^{\mathrm{n_{app}}} + ((\mathrm{P}+\mathrm{R}) * (\mathrm{b} * \mathrm{norm.}\,\mathrm{K_A}))^{\mathrm{n_{app}}}}{((\mathrm{P}+\mathrm{R}) * \ \mathrm{norm.}\,[\mathrm{Ca}^{2+}]_{\mathrm{local}})^{\mathrm{n_{app}}} + (\mathrm{b} * \mathrm{norm.}\,\mathrm{K_A})^{\mathrm{n_{app}}}} \end{aligned} \tag{14}$$

Similarly, in the presence of Agatx, the specific P/Q-type VGCC blocker, the I_{Ca} is explained by the contribution of the N-type VGCCs and the contribution of Cgtx-Agatx-insensitive channels:

$$\mathrm{norm.\,I_{Ca}(AgaTx)} = (\mathrm{N} + \mathrm{R}) * \mathrm{norm.\,I_{Ca}} = (1 - \mathrm{P}) * \mathrm{norm.\,I_{Ca}} \qquad (15)$$

Accordingly, the fEPSP fractional release after Agatx application is expressed as:

$$\mathrm{fract.\,rel.\,Agatx} \qquad (16)$$
$$= \frac{((1-\mathrm{P}) * \mathrm{norm.}[\mathrm{Ca}^{2+}]_{\mathrm{local}})^{\mathrm{n_{app}}} + ((1-\mathrm{P}) * (\mathrm{b} * \mathrm{norm.\,K_A}))^{\mathrm{n_{app}}}}{((1-\mathrm{P}) * \mathrm{norm.}[\mathrm{Ca}^{2+}]_{\mathrm{local}})^{\mathrm{n_{app}}} + (\mathrm{b} * \mathrm{norm.\,K_A})^{\mathrm{n_{app}}}}$$

A particular advantage of our approach is that allowed us to study the release machinery at different degrees of Ca^{2+} binding induced by elevating the $[Ca^{2+}]_e$ while at the same time circumventing the problems associated with different divalent cation concentrations such as changes in the number of axons stimulated. This is achieved because all the measurements were based on quantifying the relative inhibition of release and not absolute fEPSP amplitudes.

3.2.2 fEPSPs Cgtx relative inhibition in WT and RIM1α KO mice

We measured the reduction of Sc-CA1 fEPSPs amplitude by Cgtx under seven different $[Ca^{2+}]_e$: 0.8, 1, 1.5, 2, 4, 10, and 20 mM, in WT and RIM1α KO mice, in a submerged recording chamber. As synaptic responses in RIM1α KO mice are small, particularly when perfusing low $[Ca^{2+}]_e$, the effect of Cgtx on fEPSPs while perfusing 1 mM $[Ca^{2+}]_e$, was tested at 35 °C in the Haas-type interface chamber which yields a better signal-to-noise ratio. We performed control experiments, in WT mice and perfusing 2 mM $[Ca^{2+}]_e$, in order to test the effect of the different recording chambers on the Cgtx-induced fEPSP inhibition. The fractional fEPSP amplitude after Cgtx application was 44.5% ± 1.41 (mean ± SEM) (n=33) in the submerged chamber, and 47.3% ± 5.04 (n=5) in the interface chamber. These control experiments (data not shown) revealed no difference between recording chambers (statistical significance evaluated by Student's t-test, p-value > 0.05). Recordings in lower $[Ca^{2+}]_e$ (0.8 mM) were not performed in RIM1α KO mice.

As predicted, the degree of the Cgtx effect depends on the saturation level of the release machinery. The Cgtx inhibition of release was much large when applied in low $[Ca^{2+}]_e$, and the toxin effect decreased as we increased the $[Ca^{2+}]_e$ (Figure 3.5 A). This elevation of $[Ca^{2+}]_e$ could almost completely overcome the blocking effect of the VGCC toxin. In addition, in order to check a scenario of maximal $P_{r,}$ where synaptic transmission is insensitive to a partial blockade of I_{Ca}, we tested the effect of Cgtx while perfusing 20 mM $[Ca^{2+}]_e$ and 100 µM 4-Aminopyridine (4-AP), an A-type K^+ channel blocker, and did not observe a decrease in the fEPSP amplitudes (Figure 3.5 A). Cgtx decreased fEPSP amplitudes, in any of the $[Ca^{2+}]_e$ evaluated, in a lesser extent in RIM1α KO mice than in WT mice. The Cgtx inhibitory degree between genotypes was only comparable in large $[Ca^{2+}]_e$. In 1.5 mM $[Ca^{2+}]_e$ Cgtx reduced release to 38.1% ± 4.9 in WT (n=5), and to 59.6% ± 2.5 (n=5) in RIM1α KO mice; in 2 mM $[Ca^{2+}]_e$ Cgtx reduced release to 44.5% ± 1.4 in WT (n=36), and to 59.9% ± 2.9 (n=13) in RIM1α KO mice; and, in 20 mM $[Ca^{2+}]_e$ Cgtx reduced release to 85.4% ± 2.8 in WT (n=5), and to 86.9% ± 3.7 (n=13) in RIM1α KO mice.

The fractional fEPSP amplitudes remaining after Cgtx application for each single experiment were plotted versus the relative changes in the $[Ca^{2+}]_{local}$ calculated from equation (9) (Figure 3.5 B). The $[Ca^{2+}]_{local}$ achieved under control conditions (2 mM $[Ca^{2+}]_e$) is by definition set to 1 (see 3.2.1).

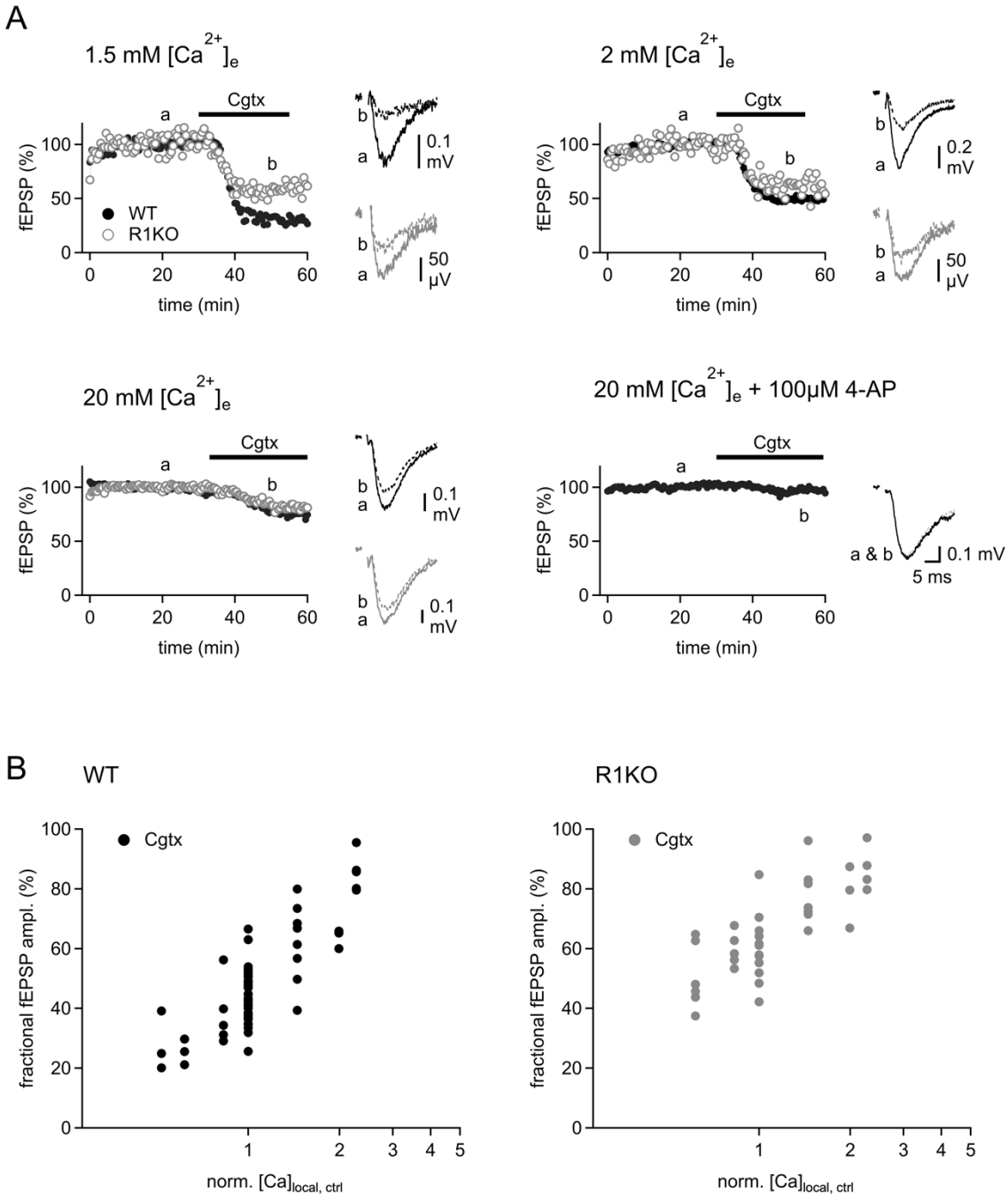

Figure 3.5 The depression of transmission by Cgtx depends on the $[Ca^{2+}]_e$. (A) Sc-CA1 fEPSPs in WT (black) and RIM1α KO mice (grey) under different $[Ca^{2+}]_e$ (1.5, 2, 20, and 20 mM with 4-AP). Cgtx is much less effective in depressing transmission when applied in elevated $[Ca^{2+}]_e$. Each of the four panels contains the time course of an example experiment for WT (solid dots) and for RIM1α KO (empty dots) mice, and the corresponding traces prior (a, solid lines) and after (b, dashed lines) Cgtx application. (B) Semi-logarithmic fractional release plots displaying the fractional fEPSP amplitudes remaining after Cgtx application in WT mice (left panel) and RIM1α KO mice (right panel).

3.2.3 fEPSPs Agatx relative inhibition in WT and RIM1α KO mice

Apart from the Cgtx effect, we tested the result of blocking the other subtype of VGCC which drives neurotransmitter release at the Sc-CA1 synapses, the P/Q-type VGCC. We performed fEPSP recordings in WT and RIM1α KO mice, under three different $[Ca^{2+}]_e$ (2, 4, and 10 mM), and quantified the resulting relative decrease after Agatx application. In the same way as Cgtx, the potency of the Agatx blocking effect was much larger in low levels of release machinery saturation. i.e. low $[Ca^{2+}]_e$; and, the inhibitory effect decreased at higher $[Ca^{2+}]_e$. In 2 mM and 4 mM $[Ca^{2+}]_e$, selective blockade of P/Q-type VGCCs with Agatx resulted in a nearly complete block of synaptic transmission in RIM1α KO mice, reduction by 80%, and in a slightly lower blocking effect in WT mice, around 60%. In 10 mM $[Ca^{2+}]_e$, there was still a considerable level of synaptic transmission after Agatx application but, as expected, the inhibition of neurotransmitter release was completely abolished in 20 mM $[Ca^{2+}{}_e]$ and 100 μM of 4-AP, conditions which bring the release machinery to saturation levels. Under all the $[Ca^{2+}]_e$ levels evaluated, the blocking potency of Agatx was noticeable larger in RIM1α KO mice than in WT mice, suggesting a larger contribution of P/Q-type VGCCs mediating neurotransmitter release in RIM1α-deficient synapses (Figure 3.6 A). In 2 mM $[Ca^{2+}]_e$ Agatx reduced release to 39.8% ± 5.6 (average ± SEM) in WT (n=5), and to 19.9% ± 3.7 (n=5) in RIM1α KO mice; in 4 mM $[Ca^{2+}]_e$ Agatx reduced release to 44% ± 4.2 in WT (n=5), and to 20.3% ± 1.6 (n=4) in RIM1α KO mice; and, in 10 mM $[Ca^{2+}]_e$ Agatx reduced release to 64.6% ± 3.6 in WT (n=5), and to 45.9% ± 4 (n=4) in RIM1α KO mice. As for Cgtx data, we plotted the fractional fEPSP amplitudes remaining after Agatx application against the relative changes in the $[Ca^{2+}]_{local}$ (Figure 3.6 B).

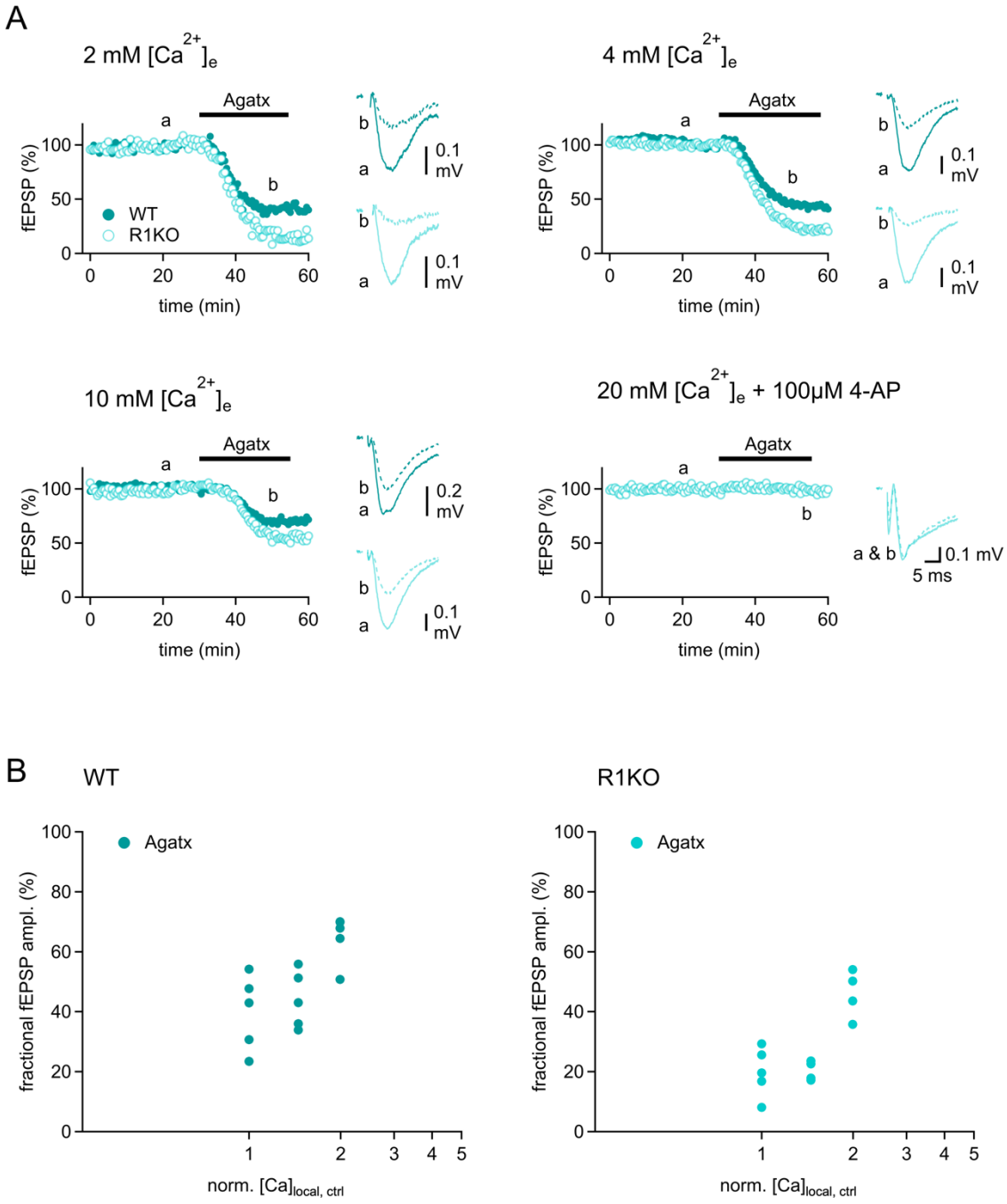

Figure 3.6 The depression of transmission by Agatx is more pronounced in RIM1α KO mice. (A) Sc-CA1 fEPSP recordings in WT (petrol) and RIM1α KO mice (turquoise) under different $[Ca^{2+}]_e$ (2, 4, 10, and 20 mM with 4-AP). Each panel contains the time course of an example experiment for WT (solid dots) and for RIM1α KO (empty dots) mice, and the corresponding traces prior (a, solid lines) and after (b, dashed lines) Agatx application. (B) Semi-logarithmic fractional release plots displaying the fractional fEPSP amplitudes remaining after Agatx application in WT mice (left panel) and RIM1α KO mice (right panel).

3.2.4 Ca^{2+} signal operating the Ca^{2+} sensor of release: increased P/Q-type VGCC contribution to the $[Ca^{2+}]_{local}$ in RIM1α KO mice

As previously mentioned, we used the fEPSPs and the Ca^{2+}-dependence blocking potency of specific VGCCs as tools to shed new light on the intracellular Ca^{2+} signal triggering neurotransmitter release. By the application of our model, extensively explained earlier in this section, we aimed to corroborate, among some other Ca^{2+}-dependence parameters, for instance, the above-suggested hypothesis of a larger contribution of P/Q-type VGCCs to synaptic transmission in RIM1α KO mice.

The fEPSP recordings consisted of four experimental datasets: two Cgtx datasets, one containing the fractional fEPSP amplitudes obtained from the WT mice, and one containing the data from RIM1α KO mice; and likewise, two Agatx datasets, WT and RIM1α KO groups. Due to the nature of the data, our model required a global analysis of the four datasets. A global fitting means that the same fitting parameters are used for all four curves and are adjusted to simultaneously best match all four datasets. One advantage of this analysis procedure is to gain the benefits of a larger number of points contributing to the fitting. Another advantage is the possibility to share parameters among the distinct datasets. When a parameter of the fitting function is shared or linked, a single value is calculated for all the datasets; whereas, when a parameter is not linked, a separate value is calculated for each dataset.

During the global fitting, the two Cgtx datasets were fitted by equation

(14), whereas the two Agatx datasets were fitted by equation (16). These two equations share global parameters, such as the normalized $[Ca^{2+}]_{local}$, the n_{app}, the factor b and the normalized K_A. The only difference between the equations resides in the type of VGCCs contributing to the I_{Ca}, and therefore, to the $[Ca^{2+}]_{local}$, as explained above. The fraction P, which indicates the contribution of P/Q-type VGCCs to the $[Ca^{2+}]_{local}$ at the release sensor, and the fraction R, which refers to the contribution of the Cgtx-Agatx-insensitive channels, were linked within the datasets for the same genotype, i.e. the global fitting provided one P and one R values for WT data, and one P and one R values for RIM1α KO data. The decision of linking those parameters was based on the fact that the contribution of the different subtypes of VGCCs to transmitter release can differ between genotypes, but not due to the

applied toxins. Regarding the fraction *R*, we decided to link it only within each genotype, because presynaptic Ca^{2+} imaging data, which will be presented later in the dissertation, showed different contribution of Cgtx-Agatx-insensitive VGCCs to the total I_{Ca} at WT and RIM1α KO presynaptic boutons, which could also be true at the level of the Ca^{2+} microdomain at the AZ.

Regarding Ca^{2+}-dependence parameters, the normalized K_A, which reports changes in the biochemical affinity of the Ca^{2+} sensor, was linked among the four datasets. This parameter was considered to be exclusively dependent on the properties of the Ca^{2+} sensor, therefore, independent on the genotype and the VGCC blocker applied during the recording. The Ca^{2+} affinity was shown to be practically unchanged in the absence of all RIM isoforms (Han et al., 2011). The factor *b* was introduced in the RIM1α KO equations to account for a possible alteration in the overall I_{Ca} (in the WT equations the factor *b* is not existing, i.e. equal to 1). The factor *b* is particularly important, thus it reports relative changes in the $[Ca^{2+}]_{local}$ seen by the Ca^{2+} sensor. A decreased total number of VGCCs at the AZ or a larger coupling distance between the channels and the sensor would decrease the $[Ca^{2+}]_{local}$ and consequently, the occupancy of the Ca^{2+} sensor, and finally the P_{ves}.

n_{app}, theoretically reports changes in the stoichiometry of the multi-step Ca^{2+} binding scheme by the release machinery, which we assumed not to be changed between genotypes (Han et al., 2011). Therefore, this factor was shared and simultaneously fitted among the four datasets.

During the global fitting procedure, we introduced weighting of the datasets, in order to account for the unequal scatter along the regression and therefore, improve the quality of the fitting. Each dataset was weighted using the inverse of the SD times the mean within all the y values (fractional fEPSP amplitudes) for each level of $[Ca^{2+}]_{local}$. Multiplication by the mean was performed to reduce the overweight of large values (large differences at same relative deviation) within standard chi-square calculation used by the fitting routine. The four datasets were simultaneously well fitted by the corresponding modified Hill equations

(14) and (16), as illustrated in Figure 3.7.

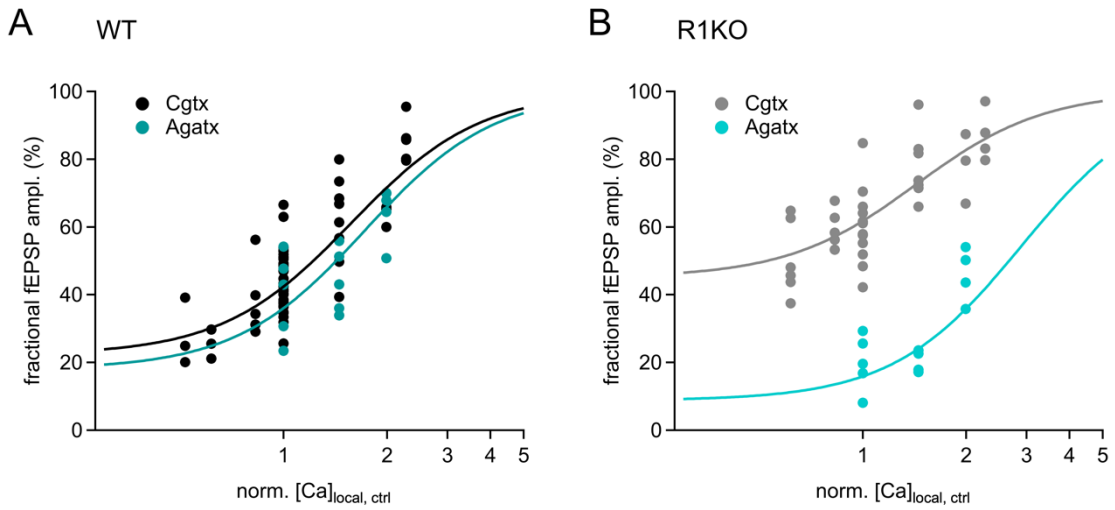

Figure 3.7 Analysis of the Ca^{2+} signal driving neurotransmitter release in RIM1α KO mice. Semi-logarithmic plots displaying the relative fractional fEPSP amplitudes against the relative changes in the $[Ca^{2+}]_e$ for WT mice (A) and for RIM1α KO mice (B). Datasets fitted by global analysis: Cgtx WT (black), Agatx WT (petrol), Cgtx RIM1α KO (grey), Agatx RIM1α KO (turquoise).

Several interesting findings regarding the Ca^{2+} signal at the release site were obtained from the global fitting. First, the analysis provided estimates of the Ca^{2+} cooperativity, n_{app}=2.32 ± 0.0048 (n=131), and the Ca^{2+} affinity, normalized K_A =0.82 ± 0.0026 (n=131) (best-fit values ± SD). The normalized K_A states how much I_{Ca} has to be altered with respect to the condition when perfusing 2 mM $[Ca^{2+}]_e$ in order to achieve half-maximal occupancy of the Ca^{2+} sensor of the release machinery. In our case, I_{Ca} has to be lowered to 82% to reach half maximal occupancy of the sensor. Second, the global fitting reported an altered $[Ca^{2+}]_{local}$ seen by the Ca^{2+} sensor in RIM1α KO mice. The factor *b* for RIM1α KO group was *b*=1.23 ± 0.0038 (n=131). Therefore, the reduction in the $[Ca^{2+}]_{local}$ was 1/*b* = 0.81, i.e. reduced by 19%. By substituting into the equation (10) the fitted values for n_{app}, normalized K_A, and *b*, and evaluating at $[Ca^{2+}]_{local}$ equal to 1, condition in 2 mM $[Ca^{2+}]_e$, we could infer the relative P_{ves} under control conditions. P_{ves} was 0.6 for WT mice, and 0.49 for RIM1α KO mice. The P_{ves} was reduced by approximately 19% in the RIM1α KO mice. Third, the subtype contribution of VGCCs to activate the Ca^{2+} sensor during fast synaptic transmission differed between genotypes. The values for *P* and *R* were directly obtained from the global fitting, and were used afterwards to

calculated the values for the fraction *N* as explained in the equation (11) (the error for *N* values were calculated according to error propagation rules). The global analysis revealed that N-type and P/Q-type VGCCs contributed almost equally to the $[Ca^{2+}]_{local}$ seen by the sensor in WT mice, being (best-fit values ± SD) P_{WT}= 0.52 ± 0.0014 (n=131) and N_{WT}= 0.48 ± 0.003 (n=131). However, in RIM1α KO mice the fractional contribution was strongly shifted towards P/Q-type VGCCs, being P_{R1KO}=0.65 ± 0.0013 (n=131) and N_{R1KO}=0.29 ± 0.0026 (n=131). Apart from a higher P/Q-type VGCC contribution in RIM1α KO mice, the fraction *R* revealed an involvement of Cgtx-Agatx-insensitive VGCCs contributing to the $[Ca^{2+}]_{local}$, R_{R1KO}=0.06 ± 0.0022 (n=131), which is not existing in WT mice (R_{WT}=3.14·10^{-17}% ± 0.0022 (n=131).

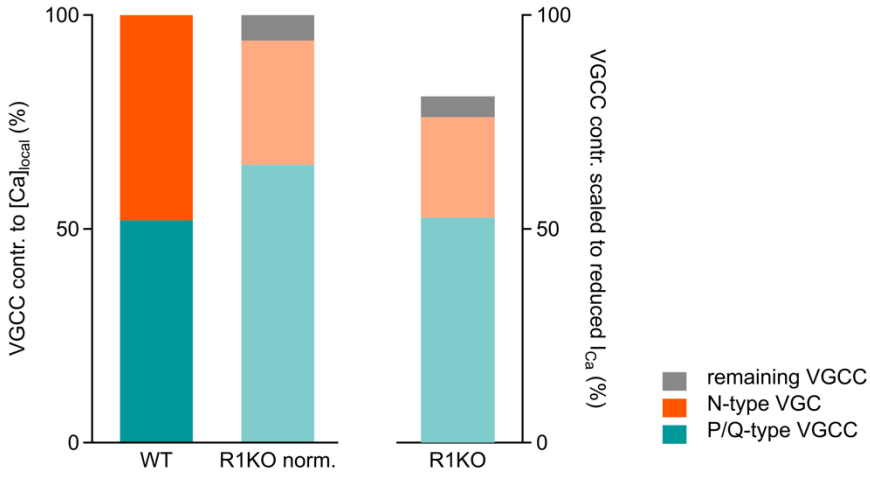

Figure 3.8 Increased P/Q-type VGCC contribution to the $[Ca^{2+}]_{local}$ in RIM1α KO mice. Bar graph depicting the subtype contribution of VGCCs to the $[Ca^{2+}]_{local}$ for WT and RIM1α KO mice. Right bar indicates the contribution of VGCC to the $[Ca^{2+}]_{local}$ scaled to the presynaptic Ca^{2+} entry in RIM1α KO mice, reduced by 19% compared to WT mice. N-type VGCCs (orange), P/Q-type VGCCs (petrol), and Cgtx-Agatx-insensitive VGCCs (grey).

The statistical analysis of the global fitting outcome was performed by calculating the 95% confidence intervals (CI) of the best-fit values for *P*, *N*, and *R*. The CIs were very narrow (see legend of Figure 3.8), indicating that the best-fit values were estimated precisely. Because the 95% CIs for the RIM1α KO best-fit values for *P*, *N*, and *R*, do not contain the values of the null hypothesis, the WT values for *P*, *N*, and *R*, the subtype contribution of VGCCs mediating synaptic transmission between WT and RIM1α KO mice was statistically significant with a P-value < 0.05 for all of the

different subtypes. This outcome highlights a role for RIM1α tuning the subtype of VGCCs involved in driving neurotransmitter release at a small central synapse, such as the hippocampal Sc-CA1 synapses.

3.2.5 Ca^{2+} signal operating the Ca^{2+} sensor of release in RIM3 KO and RIM4 KO mice

The functional role of α-RIMs has been intensively studied during the past years, however much little attention has been devoted to the role of the small RIM isoforms RIM3 and RIM4. Our results showed unaltered short-term synaptic plasticity in RIM3 KO mice and in RIM4 KO mice (Figure 3.3), as well as unchanged spontaneous release in the RIM4 KO animals (Figure 3.2). Nevertheless, in order to continue analyzing a possible physiological role of γ-RIMs modulating synaptic release, we applied our newly developed mathematical approach to explore the nature of the AP-triggered presynaptic Ca^{2+} signal. We hypothesized that γ-RIMs may modulate fast synaptic transmission by competing with α-RIMs due to a possible homodimerization of the C_2B RIM domain present in all isoforms.

We evaluated the inhibitory Cgtx effect on Sc-CA1 fEPSP recordings performed in RIM3 KO and RIM4 KO mice under several $[Ca^{2+}]_e$ (0.8, 1, 1.5, 2, 4, 10 and 20 mM). As seen in WT and RIM1α KO for both specific VGCC toxins, Cgtx reduced fEPSPs in a Ca^{2+}-dependent manner in RIM3 KO and RIM4 KO recordings. The degree of inhibition at any level of $[Ca^{2+}]_e$ was comparable between the γ-RIM KOs and WT mice (Figure 3.9). In 1.5 mM $[Ca^{2+}]_e$ Cgtx reduced release to 38.1% ± 4.9 in WT (n=5), to 28.8% ± 3.4 (n=7) in RIM3 KO, and to 25.2% ± 2.3 (n=5) in RIM4 KO mice. In 2 mM $[Ca^{2+}]_e$ Cgtx reduced release to 44.5% ± 1.4 in WT (n=36), to 47.6% ± 3.3 (n=6) in RIM3 KO, and to 35.6% ± 3 (n=11) in RIM4 KO mice. And in 20 mM $[Ca^{2+}]_e$ Cgtx reduced release to 85.4% ± 2.8 in WT (n=5), and to 80.4% ± 5 (n=5) in RIM3 KO, and to 78.5% ± 2 (n=5) in RIM4 KO mice. The remaining fractional fEPSP amplitudes after Cgtx application were plotted against the relative values of $[Ca^{2+}]_{local}$. The RIM3 KO data and the RIM4 KO data were fitted separately by the following equation:

$$\text{fract. rel. Cgtx} = \\ = \frac{((1-N) * \text{ norm.}[\text{Ca}^{2+}]_{\text{local}})^{\text{n}_{\text{app}}} + ((1-N) * (\text{b} * \text{norm. K}_{\text{A}}))^{\text{n}_{\text{app}}}}{((1-N) * \text{ norm.}[\text{Ca}^{2+}]_{\text{local}})^{\text{n}_{\text{app}}} + (\text{b} * \text{norm. K}_{\text{A}})^{\text{n}_{\text{app}}}} \quad (17)$$

This equation is equivalent to equation

(**14**), but the I_{Ca} after the blockade of N-type VGCC by Cgtx is expressed in terms of fraction *N*. During the fitting, the parameters normalized K_A and n_{app}, which are supposed to be independent of the genotype, were held. The holding values for normalized K_A and n_{app} were the ones obtained from the global analysis for the WT mice (normalized K_A=0.82; n_{app}=2.32, see above). The datasets were weighted as for the WT and RIM1α KO datasets. Regarding RIM3 KO data, the fitting indicated a fraction N_{R3KO}= 0.51 ± 0.0007 (n=29). The factor *b* for the RIM3 KO was equal to 0.89 ± 0.0028 (n=29), suggesting an increase in $[Ca^{2+}]_{local}$ by 11% compared to WT mice. By means of equation (10), the P_{ves} for RIM3 KO synapses was approximately equal to 0.67, similar to WT synapses. Regarding the RIM4 KO data, the individual fitting gave rise to a fraction N_{R4KO}= 0.56 ± 0.0005 (n=42), and a factor *b* equal to 0.8 ± 0.0018 (n=42). From the best-fit value for factor *b*, we estimated an increase in $[Ca^{2+}]_{local}$ by 23%, which, by using equation (10), indicated a P_{ves}=0.72. Compared to a WT scenario, the P_{ves} was increased by 20% in RIM4 KO mice.

We compared the fractions *N* for both γ-RIMs to the one obtained for the WT group by calculating the 95% CIs. According to the statistical analysis, the values were different when compare N_{R3KO} to N_{WT}, as well as N_{R4KO} to N_{WT}. Nevertheless, the physiological meaning of this result remained to be elucidated. The ablation of the γ-RIMs shaped, in both cases, a presynaptic AZ where the N-type VGCCs seemed to contribute in a slightly larger degree than the P/Q-type channels to the $[Ca^{2+}]_{local}$ seen by the sensor during an AP.

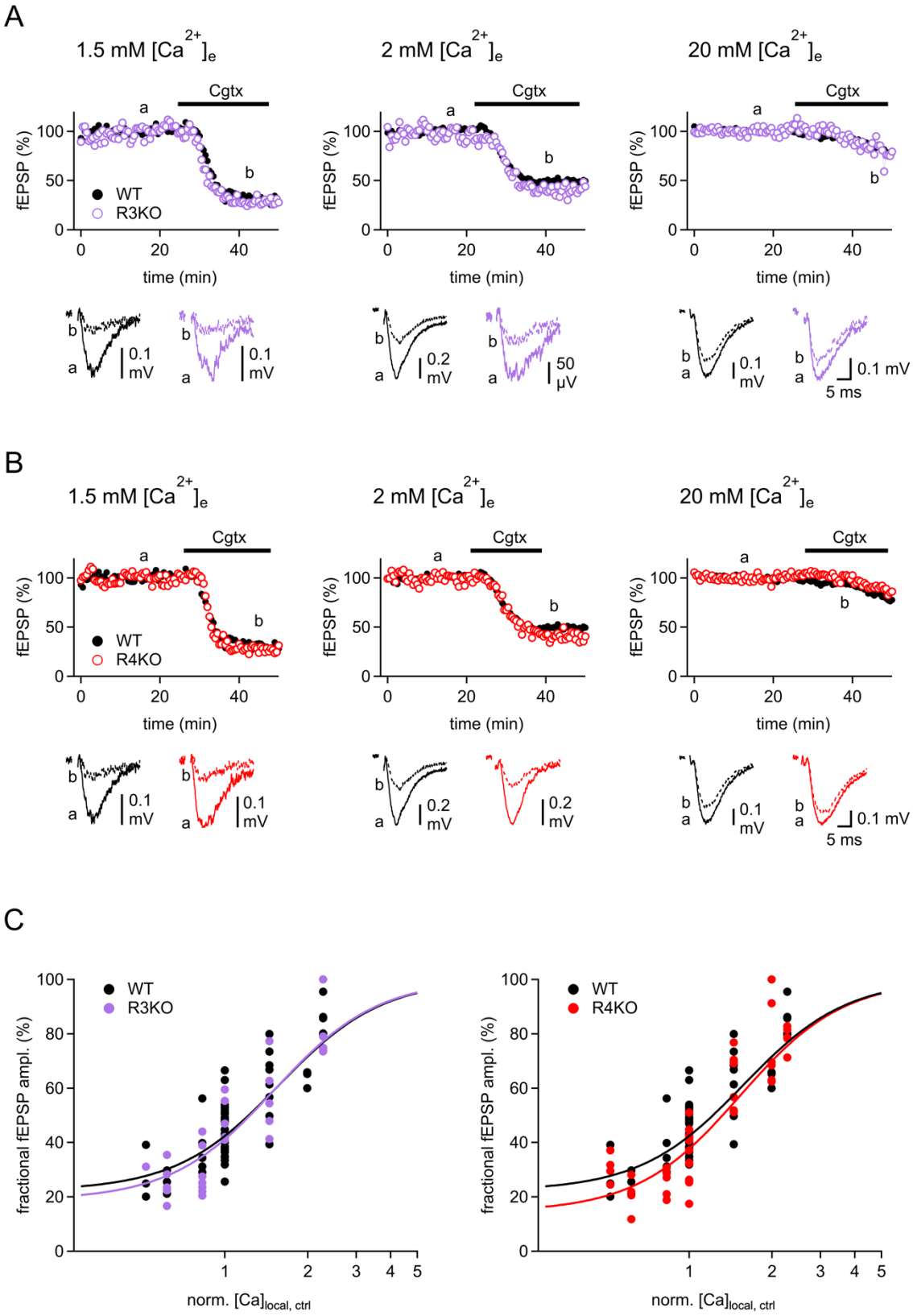

Figure 3.9 Screening for a possible synaptic function of the γ-RIMs, RIM3 and RIM4. (A) Time courses of representative experiments for Cgtx-mediated inhibition of Sc-CA1

fEPSP recordings in WT (black, solid dots) and in RIM3 KO (purple, empty dots) mice, under several $[Ca^{2+}]_e$ (1.5, 2, and 20 mM). Insets display fEPSP traces before (a, solid line) and after (b, dashed line) blocker application. (B) Representative experiments for WT (black, solid dots) and RIM4 KO (red, empty dots) mice depicted as RIM3 KO data. (C) Fractional release curves calculated from the fractional fEPSP amplitudes remaining after application of Cgtx. Data fitted not simultaneously by equation (14), WT data (black), RIM3 KO data (purple), and RIM4 KO data (red).

3.3 Slightly decelerated fast neurotransmitter release in RIM1α KO mice

The above data showed that in the absence of RIM1α, there was a strong shift in the relative contribution of the different subtypes of VGCCs to the $[Ca^{2+}]_{local}$, together with a slight reduction in the $[Ca^{2+}]_{local}$, which translated into a decreased P_{ves}, and an altered short-term synaptic plasticity. A decreased $[Ca^{2+}]_{local}$, which would impact temporal release properties, could be reflected in the kinetics of release. We focussed this kinetics analysis on RIM1α KO mice as they show a clearly altered transmitter release. Our data and previous publications revealed decreased P_{ves}, decreased P_r, and enhanced PPF in the absence of RIM1α (Schoch et al., 2002)

We measured three different kinetic parameters of release: the synaptic delay, the 20-80% rise time, and the time constant of the decay phase. We analyzed the kinetics of fEPSPs recorded in WT mice and RIM1α KO mice in several $[Ca^{2+}]_e$ (Figure 3.10). The kinetics parameters did not significantly differ.

We quantified the synaptic delay as the time from the peak of the fiber volley, which indicates the occurrence of the presynaptic AP, to the 20% of the fEPSP amplitude. The synaptic delay is shaped by the kinetics of the I_{Ca} and the kinetics of the Ca^{2+} binding to the release machinery as well as the vesicular fusion process and the opening of postsynaptic glutamate receptors. RIM1α KO mice displayed a slightly, although not significant, larger delay in the latency of the Ca^{2+}-induced release, which, as in WT mice, decreased by elevating the $[Ca^{2+}]_e$. Second, we assessed the kinetics of the fEPSPs: the 20-80% rise time, and the tau of the decay phase, obtained by a single exponential fitting. The rise time tended to be larger in RIM1α KO mice, suggesting a slightly decelerated release. This difference between genotypes was overcome by increasing I_{Ca}. The tau of the decay seemed to be constant among the different $[Ca^{2+}]_e$ in RIM1α KO mice suggesting that the release

rate does not accelerate correspondingly to an increase in I_{Ca}, effect which we observed in WT mice. However, this parameter has to be treated carefully as its shape is also defined by the gating properties of the glutamate postsynaptic receptors. Additionally, the differences across $[Ca^{2+}]_e$ for all the studied parameters were more pronounced between to 2 mM and 4 mM, than between 4 mM and 20 mM, implying a possible "near-saturation" scenario at the release machinery in 4 mM $[Ca^{2+}]_e$. Despite the restrictions of this analysis, our data indicated a vaguely slower transmitter release in RIM1α KO mice, a likely consequence of the decreased $[Ca^{2+}]_{local}$ at the release sensor.

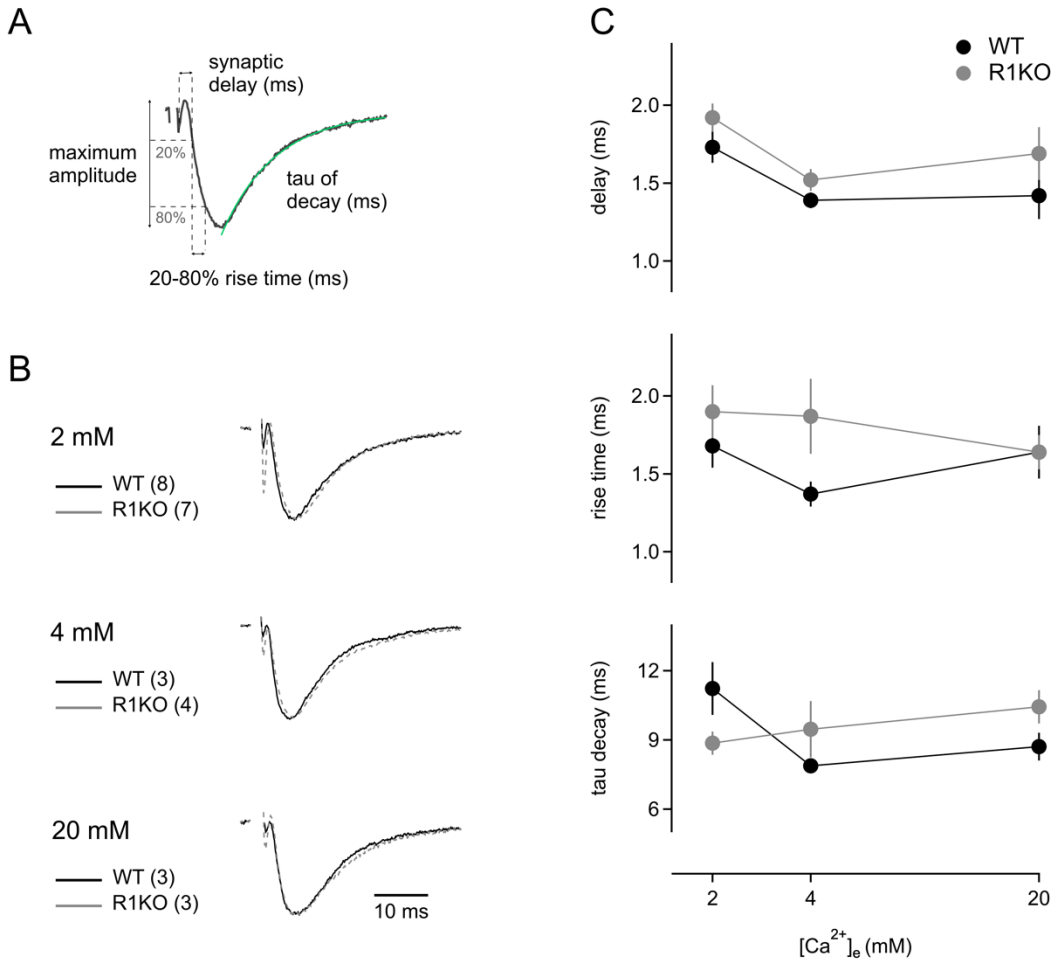

Figure 3.10 Kinetics of release in Sc-CA1 synapses. (A) Scheme illustrating the kinetic parameters of release: synaptic delay, rise time, and tau of decay. (B) Superimposed average traces of fEPSPs under 2, 4, and 20 mM $[Ca^{2+}]_e$ for WT (solid and black line) and RIM1α KO (dashed and grey line). (C) WT (black) and RIM1α KO (grey) data of synaptic delay, 20-80% rise time, and the time constant of the decay plotted against the $[Ca^{2+}]_e$. Data depicted as mean ± SEM. Synaptic delay values for WT in 2, 4, and 20 mM were 1.73 ± 0.1,

1.39 ± 0.05, and 1.42 ± 0.15, respectively; and for RIM1α KO 1.92 ± 0.09, 1.52 ± 0.07, and 1.69 ± 0.17. Rise time values for WT in 2, 4, and 20 mM were 1.68 ± 0.14, 1.37 ± 0.08, and 1.64 ± 0.17, respectively; and for RIM1α KO 1.9 ± 0.17, 1.87 ± 0.24, and 1.64 ± 0.11. Tau of decay values for WT in 2, 4, and 20 mM were 11.2 ± 1.14, 7.8 ± 0.08, and 8.7 ± 0.6, respectively; and for RIM1α KO 8.86 ± 0.5, 9.46 ± 1.22, and 10.43 ± 0.72. Statistical significance for every kinetics parameter was tested within each $[Ca^{2+}]_e$ by Student's t-test, P-values > 0.05.

3.4 Unaltered distance between Ca^{2+} source and Ca^{2+} sensor in RIM1α KO mice

The $[Ca^{2+}]_{local}$ built up close to the RRP in response to an AP is a function of the distance between VGCCs and SVs. An altered coupling distance between the Ca^{2+} source and the Ca^{2+} sensor, could also explain the decreased in the $[Ca^{2+}]_{local}$ observed in RIM1α KO mice.

To test for a decreased coupling distance between VGCCs and SVs, we measured the reduction of transmitter release by the slow Ca^{2+} buffer, EGTA-AM. EGTA at presynaptic terminals reduces transmitter release by capturing Ca^{2+} ions originated from remote VGCCs. We measured fEPSPs at the Sc-CA1 synapses in WT and RIM1α KO mice and measured the inhibition by the slow Ca^{2+} chelator. In both genotypes, the EGTA-dependent Ca^{2+} chelation reduced transmitter release significantly, but little, indicating a tight coupling between VGCCs and SVs at the presynaptic AZs of the CA3 pyramidal cells. At WT synapses, EGTA-AM reduced fEPSPs by 23% ± 3.42 (n=6), and at RIM1α KO synapses to a similar degree, by 17% ± 1.18 (n=6) (Figure 3.11).

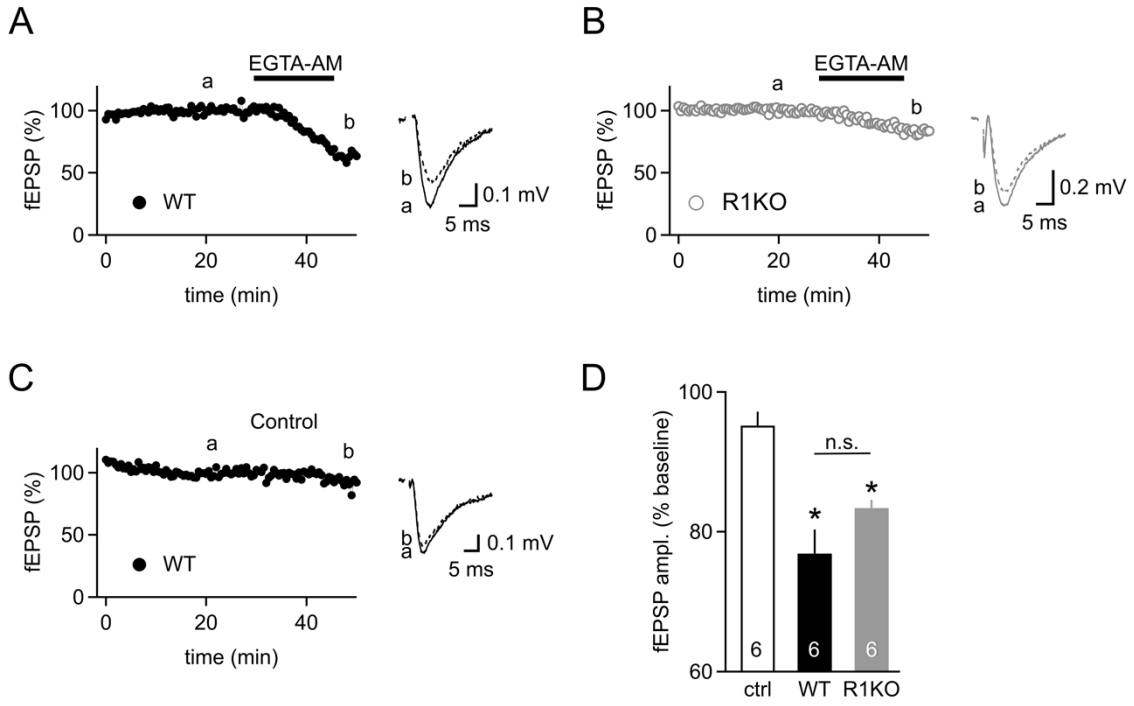

Figure 3.11 Unaltered distance between VGCCs and SVs in RIM1α KO mice. Time courses of representative examples showing the inhibition of fEPSPs induced by addition of the membrane-permeable Ca^{2+}-chelator EGTA-AM (100 µM) in WT mice (A), in RIM1α KO mice (B), and adding a control solution (C). Sample traces before (a, solid line) and after (b, dashed line) EGTA-AM are shown next to the time courses graphs. (D) Summary bar graph of the percentage of fEPSP amplitude, respect to baseline, remaining after the chelator application. In control solution 95.2% ± 1.98, in WT 76.9% ± 3.42, and in RIM1α KO 83.4% ± 1.18. Statistical significance was assessed by one-way ANOVA and Tukey post-hoc test (p-value < 0.05 for the comparison between control and WT, and control and RIM1α KO; p-value > 0.05 for the comparison between WT and RIM1α KO).

3.5 Equivalent Cgtx effect on fEPSPs and EPSCs

Most of our data were based on extracellular readouts of the synaptic activity (fEPSPs); therefore, we considered necessary to test the reproducibility of our data when recording synaptic activity intracellularly, i.e. through whole-cell patch-clamp recordings (EPSCs).

As the Cgtx-mediated reduction of transmitter release was extensively used for the analysis of the presynaptic Ca^{2+} signal, we compared the Cgtx inhibitory effect on Schaffer collateral-mediated fEPSPs and on EPSCs recorded from CA1 pyramidal cells. We measured EPSCs in WT in the presence of 2 mM $[Ca^{2+}]_e$ and in RIM1α KO

mice in 1 mM $[Ca^{2+}]_e$ and compared them to our previous estimates of Cgtx inhibition of fEPSPs. The reduction of synaptic transmission by Cgtx was equivalent between field potential and single cell recordings in both genotypes. In WT mice, 1 μM of Cgtx reduced fEPSPs amplitude to 44.5% ± 1.39 (n=36), and EPSCs amplitude to 42.1% ± 4.06 (n=4). In RIM1α KO, generally less sensitive to the specific N-type VGCC, Cgtx reduced synaptic activity measured extracellularly to 50.4% ± 4.07 (n=6), and to 62.6% ± 3.38 (n=5), when it was measured from a single cell. We quantified the degree of inhibition from average EPSC traces before and after drug application; in the case of RIM1α KO EPSCs, both average traces, prior to and after toxin, were a mixed population of successful EPSCs and failures, due to the reduced synaptic transmitter output inherent to RIM1α KO phenotype and emphasized by the low $[Ca^{2+}]_e$ (i.e. 1 mM). We illustrated the effect of Cgtx on RIM1α KO EPSCs (Figure 3.12 D) by showing the increase in the number of failures upon Cgtx application.

These results strongly support the validity of our extracellular recordings data, which give us the advantage of recording large numbers of neurons simultaneously, to infer knowledge about individual neuron synaptic transmission mechanisms.

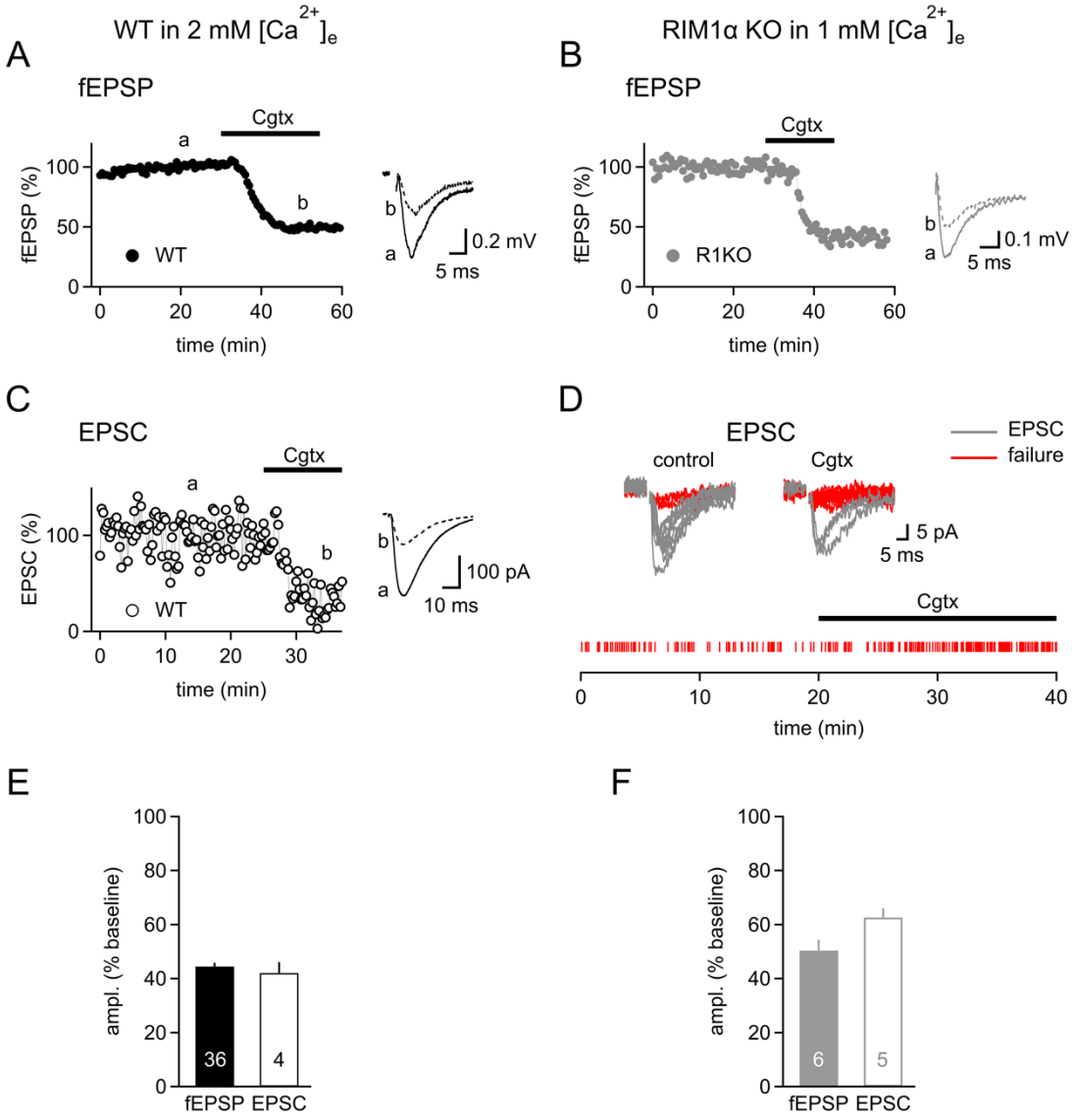

Figure 3.12 The Cgtx effect on the synaptic output recorded from a population of neurons reflected accurately the effect on the synaptic output recorded from individual neurons. Inhibition of synaptic transmission by Cgtx. (A) Representative experiment for fEPSPs recordings in WT mice in 2 mM $[Ca^{2+}]_e$. Time course and average traces before (a, solid line) and after (b, dashed line) toxin application. (B) Representative experiment for fEPSPs recorded in RIM1α KO mice during 1 mM $[Ca^{2+}]_e$. Time course and average traces. (C) Representative experiments for whole-cell patch-clamp recordings in WT mice in 2 mM $[Ca^{2+}]_e$. Time course of the EPSC amplitudes and average traces before (a, solid line) and after (b, dashed line) Cgtx application. (D) Representative experiment of EPSCs recorded in RIM1α KO mice in 1 mM $[Ca^{2+}]_e$. The EPSCs and failures in response to stimulation are represented before (control) and during Cgtx application (Cgtx). Increased number of failures during drug application. Raster plot depicting the failures during the time course of the recording. (E) and (F) Summary diagram of the degree of inhibition triggered by Cgtx application. Amplitude remaining after drug application normalized to control conditions. Data depicted as mean ± SEM. In WT mice, the amplitude remaining after Cgtx application was 44.5% ± 1.39 for fEPSPs and 42.1% ± 4.06 for EPSCs. In RIM1α KO mice,

the amplitude remaining after Cgtx application was 50.4% ± 4.07 for fEPSPs and 62.6% ± 3.38 for EPSCs. Statistical test was assessed by Student's t-test (p-value > 0.05).

3.6 Unaltered Cgtx sensitivity of transmitter release in cDKO mice

Our data revealed that the single deletion of RIM1α made neurotransmitter release less sensitive to the specific N-type VGCC, Cgtx, indicating a role for RIM1α tuning the subtype VGCC contribution to synaptic transmission at the hippocampal Sc-CA1 synapses. In order to investigate the contribution of action of different large RIM isoforms, i.e. RIM1β, RIM2α, and RIM2β, to the newly defined functional role of RIM1α, we analyzed the contribution of N-type VGCC to transmitter release in mice lacking all the α and β RIM isoforms. We used cDKO mice RIM1αβ and RIM2αβγ, as constitutive DKO mice die immediately after birth (Schoch et al., 2006). In order to target RIM1αβ and RIM2αβγ deletion selectively to Schaffer collateral pathway, we employed the Cre-lox system. We used a mouse line expressing Cre recombinase under a specific promoter of CA3 pyramidal cells, crossed to the cDKO line in order to generate the Et(iCre)-tdTomato-cDKO mouse line (Figure 3.13 A). Before electrophysiological recordings, with the help of Hyuntae Kim, a colleague from the lab, we evaluated the efficiency of the Cre-mediated recombination by counting CA3 pyramidal cells which were positive for tdTomato, the reporter line. We measured the recombination efficiency at four different levels of the hippocampal CA3 area using regions of interest (ROIs) (Figure 3.13 B and C). The quantification revealed that the Cre-mediated recombination efficiency decreased along the proximal-distal axis of the CA3 region (Figure 3.13 D).

After evaluating the recombination efficiency, we recorded Schaffer collateral-evoked fEPSPs from Cre-recombinase negative mice, which retain RIM expression, and from Cre-recombinase positive mice, the cDKO mice. We quantified the relative decrease in fEPSPs amplitude after Cgtx application in 2 mM $[Ca^{2+}]_e$. Conditional Cre-recombinase negative mice, expected to be as WT mice, showed a Cgtx-mediated decrease in synaptic transmission comparable to WT mice. WT mice showed a reduction to 44.5% ± 1.4 (n=36), and the Cre-recombinase negative mice a reduction to 52.4% ± 6.48 (n=3) (data not shown). In the cDKO mice, Cgtx reduced neurotransmitter release more pronounced than in the RIM1α KO mice. The

reduction seen in cDKO was equal to 50% ± 3.8 (n=8), whereas in RIM1α KO mice was equal to 60% ± 2.9 (n=13), significantly different to WT and to cDKO mice. cDKO mice showed values for Cgtx sensitivity similar to WT mice (Figure 3.13 F). Surprisingly, these data seem to suggest that after the ablation of all large RIM isoforms, the alteration seen in RIM1α KO regarding subtype VGCC contribution to transmitter release, was restored. Nonetheless, to give a larger power to our data it would be necessary a deeper analysis of the Ca^{2+} signal-mediating neurotransmitter release by our fractional release Ca^{2+} curve approach.

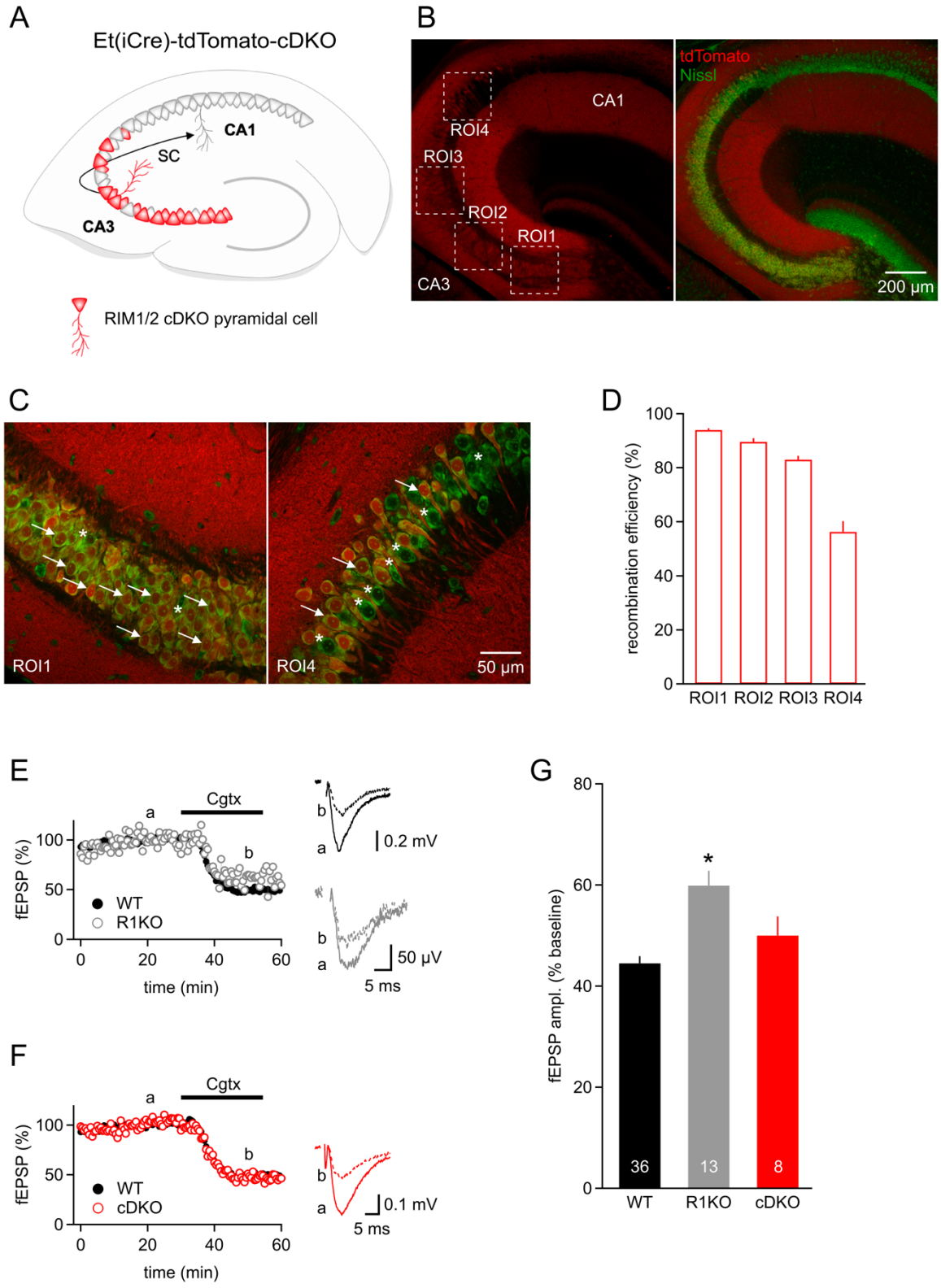

Figure 3.13 Cgtx sensitivity of transmitter release in cDKO mice is similar to WT mice. (A) Scheme of the hippocampus of the Et(iCre)-tdTomato-cDKO mice showing the recombining CA3 pyramidal cells in red. (B) Confocal image illustrating the tdTomato

reporter expression in the hippocampus (red) indicating the location of the analyzed ROIs along the proximal-distal axis of the CA3 region; previous confocal image in combination with Nissl staining (green), a marker for cell bodies. (C) Confocal images for the proximal ROI, RO1, and the distal ROI, ROI4. Arrows indicate colocalization of tdTomato and Nissl expression, i.e. recombining CA3 pyramidal cells. Asterisks indicate non-recombining cells. (D) Bar graph showing the quantification of the Cre-mediated recombination efficiency for each ROI. Recombination efficiency in ROI1=94% ± 0.66, in ROI2=89.6% ± 1.35, in ROI3=83% ± 1.44, and in ROI4=56.3% ± 4. Two Et(iCre)-tdTomato-cDKO mice were used. (E) Representative experiments of Cgtx inhibition of fEPSP amplitudes in WT (black) and in RIM1α KO (grey) mice. Time courses (WT, solid dots, and RIM1α KO, empty dots) and average traces before (a) and after (b) toxin application. (F) Representative recordings of Cgtx reduction of fEPSP amplitudes in WT (black) and in cDKO (red) mice. Time courses (WT, solid dots, and RIM1α KO, empty dots) and average traces prior to (a) and after (b) blocker application. (G) Summary of the degree of inhibition of fEPSP by Cgtx application. The values are for WT 44.5% ± 1.4 (n=33), for RIM1α KO 60% ± 2.9 (n=13), and for cDKO 50% ± 3.8 (n=8). The values for the conditional Cre-negative mice are 52.4 ± 6.48 (n=3). Data not shown. Statistical significance was evaluated by one-way ANOVA test and post-hoc Tukey test, p-value < 0.05.

3.7 Differential contribution of VGCC to Ca^{2+} entry in RIM1α KO mice

From the profound analysis of the Ca^{2+} signal mediating synaptic transmission, we concluded that Schaffer collateral synapses in RIM1α KO mice might show a larger contribution of P/Q-type VGCCs, lower contribution of N-type VGCCs, and additional contribution of Cgtx-Aga-insensitive VGCCs, to the $[Ca^{2+}]_{local}$ seen by the Ca^{2+} sensor during an AP, $[Ca^{2+}]_{local}$ which itself was reduced approximately by 20% compared to WT mice. Our approach provided us with a picture of the VGCC distribution within the AZ. We decided to enlarge upon this scenario by investigating the contribution of the different subtypes of VGCCs to the total I_{Ca} at the presynaptic terminal. We expected to get insight into the possibility that the situation observed in RIM1α KO release sites was extended to the total number of VGCCs in the presynaptic bouton, or if on the contrary, the ablation of RIM1α specifically tuned the VGCCs distribution and number only at the AZ, supporting the hypothesis of a functional role for RIM1α tethering VGCCs to SVs at the AZ.

We performed bulk loading of Ca^{2+} indicator into presynaptic terminals, used a photodiode to measure fluorescent responses to AP stimulation (presynaptic Ca^{2+} imaging), and quantified the contribution of the different subtypes of VGCCs to the presynaptic I_{Ca} upon the arrival of an AP. To monitor the Ca^{2+} transient at the CA3 presynaptic terminals, the Schaffer collateral fibers of WT and RIM1α KO mice were

loaded with the low-affinity membrane-permeable Ca^{2+} indicator, Mg-Green AM. The Schaffer collateral fibers were stimulated as for fEPSPs recordings, and the fluorescent transients, arisen from presynaptic Ca^{2+} influx, were detected from a region at the stratum radiatum of the CA1 region which contained loaded presynaptic terminals. We tested the pure presynaptic origin of the fluorescent signal by application of 10 µM CNQX and 50 µM APV, which as expected did not alter the Ca^{2+} transient (data not shown). The application of the specific VGCC blockers decreased presynaptic I_{Ca} measured in WT and RIM1α KO. In both genotypes, Agatx reduced Ca^{2+} entry more strongly than Cgtx, indicating a higher presence of P/Q-type VGCCs compared to N-type VGCCs at the presynaptic boutons of WT and RIM1α KO mice. In WT mice, Cgtx reduced fluorescent transients by a larger degree, 26.5% ± 3.34 (n=7), than in RIM1α KO mice, 16.2% ± 1.33 (n=6). Similarly, Agatx effect was more potent reducing presynaptic Ca^{2+} influx in WT mice 49.5% ± 4.27 (n=4), than in RIM1α KO mice, where the Ca^{2+} transients were reduced by 41.2% ± 1.58 (n=4). Both types of VGCCs involved in synaptic transmission at Sc-CA1 synapses, P/Q-type and N-type, contributed in a lesser degree to the I_{Ca} in RIM1α KO mice, suggesting that RIM1α deficient synapses may present other types of VGCCs which contribute to the Ca^{2+} entry upon the arrival of an AP. In order to elucidate the nature of these channels, we incubated the hippocampal slices in the presence of Cgtx and Agatx, prior to the imaging, in order to measure only Ca^{2+} entry through Cgtx-Agatx-insensitive VGCCs. During the experiment, we applied simultaneously Ni^{2+}, which blocked T-type and R-type VGCCs, and verapamil, a T-type and L-type VGCC blocker. As expected, the remaining fluorescent transients, after Cgtx-Agatx blocking, were reduced by 38% ± 7.4 (n=4) in WT mice, and by 46.5% ± 4.1 (n=4) in RIM1α KO mice. In the case of WT mice, the inhibition by Ni^{2+} and verapamil represented the 9% of the I_{Ca} (see 2.7.6), whereas, for RIM1α KO mice, the inhibition mediated by Ni^{2+} and verapamil amounted to 20% of the I_{Ca}. We tested next the effect of the specific R-type VGCC blocker, SNX-482, inhibiting presynaptic Ca^{2+} transients. Unexpectedly, the application of SNX-482 did not affect the magnitude of I_{Ca} nor in WT mice neither in RIM1α KO mice (Figure 3.14 H). Summing the inhibition by Cgtx, by Agatx, and

by Ni^{2+} and verapamil, arithmetically a small proportion of Ca^{2+} signal remained still unblocked, 15% in WT and 23% in RIM1α KO mice. When we applied simultaneously all the VGCC blockers, Ca^{2+} transients measured in WT mice were nearly abolished (Figure 3.14 I). Our Ca^{2+} imaging data revealed significant alterations in the Cgtx-sensitive fractions and in the Ni^{2+}/verapamil-sensitive fractions between WT and RIM1α KO mice. Compelling, this data pointed out a scenario wherein the absence of RIM1α less Ca^{2+} entry occurred through P/Q-type and N-type VGCCs, and more through, possibly, T-type or L-type VGCCs. The shift towards a neurotransmitter release mediated in a larger degree by P/Q-type VGCCs observed RIM1α KO mice was not due to a higher presence of these subtype of channels at the presynaptic terminal.

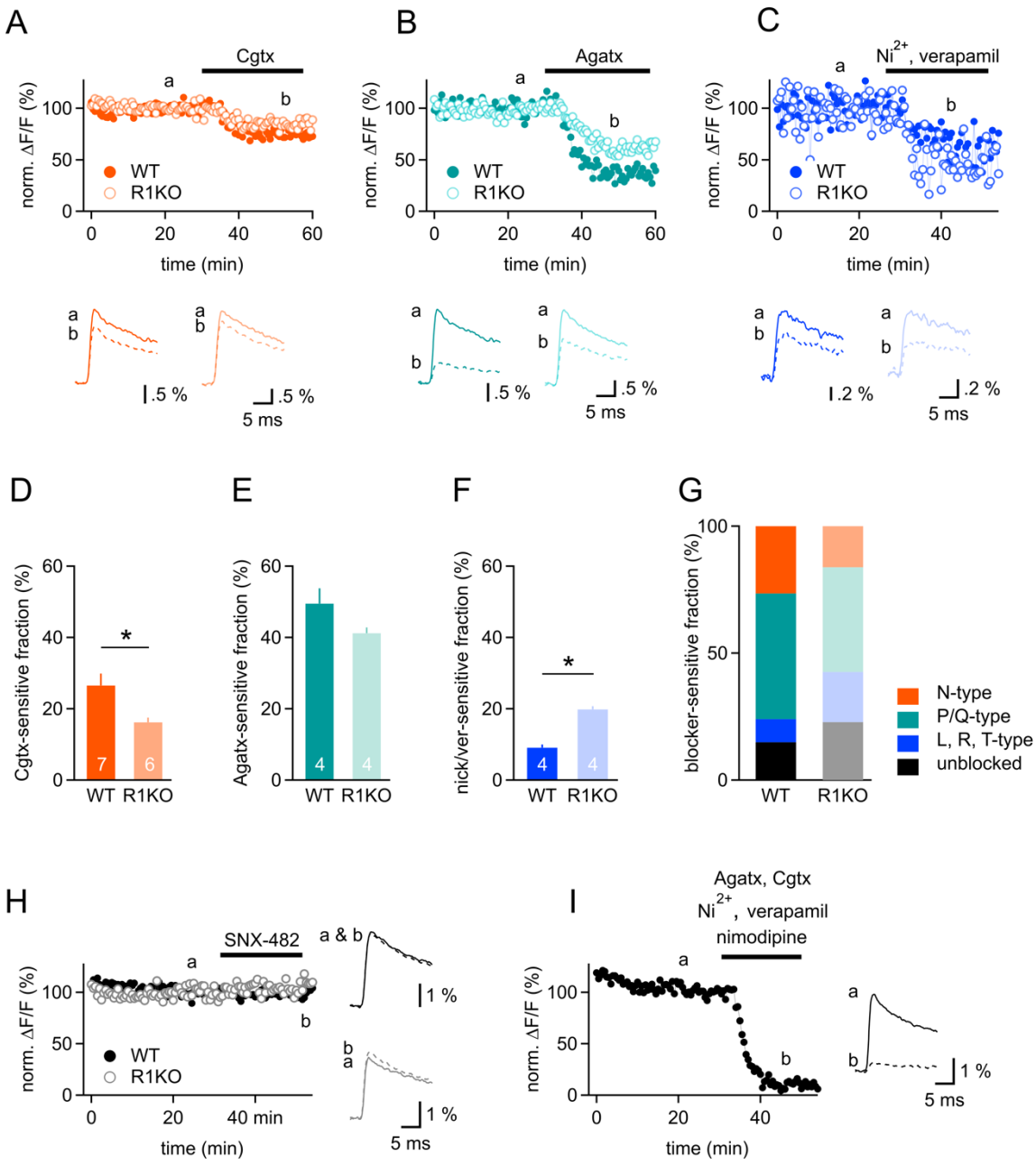

Figure 3.14 Slightly altered contribution of the different VGCC subtypes to the I_{Ca} in RIM1α KO mice. Representative Ca^{2+} imaging recordings in WT mice and in RIM1α KO mice for Cgtx (A), Agatx (B), and Ni^{2+}/verapamil inhibition (C). The upper panels show the time courses of the peak amplitude of fluorescence increases evoked by extracellular stimulation for WT (solid dots) and for RIM1α KO (empty dots). The lower panels show average traces from WT (dark color) and from RIM1α KO (light color) mice before blocker application (solid lines) and after application (dashed lines). (D) Summary bar graph of the fraction of I_{Ca} sensitive to Cgtx in WT (26.5% ± 3.34) and in RIM1α KO mice (16.2% ± 1.33). Statistical significance assessed by Student's t-test (p-value < 0.05). (E) Summary bar graph of the fraction of I_{Ca} sensitive to Agatx in WT (49.5% ± 4.27) and in RIM1α KO mice (41.2% ± 1.58). Statistical significance assessed by Student's t-test (p-value > 0.05). (F) Summary bar graph of the fraction of I_{Ca} sensitive to Ni^{2+} and verapamil in WT (9.1% ± 0.89)

and in RIM1α KO mice (19.8% ± 0.87). Statistical significance assessed by Student's t-test (p-value < 0.05). (G) Summary bar graph depicting the subtype contribution of VGCCs to the $I_{Ca.}$ Unblocked Ca^{2+} signal in WT 15%, and in RIM1α KO mice 23%. (H) Representative example of SNX-482 presynaptic Ca^{2+} transients' inhibition. Time courses for WT (solid dots) and for RIM1α KO (empty dots), and average traces from WT (black) and from RIM1α KO (grey) before (solid line) and after (dashed line) application of the specific R-type VGCC blocker. Three experiments were performed in WT mice with an average remaining Ca^{2+} signal equal to 104.6% ± 2.8, and one experiment in RIM1α KO mice with 108.7% remaining signal. (I) Ca^{2+} signal inhibition by simultaneous application of Cgtx, Agatx, Ni^{2+}, verapamil, and nimodipine, a specific L-type VGCC blocker. Time course and average traces before (solid line) and after (dashed line) cocktail blocker application for a representative experiment performed in WT mice.

3.8 Assessing release properties in cultured cells expressing RIM-GFP fusion protein

Our laboratory, in collaboration with Prof. Schoch's lab, aims to elucidate the role of the RIM protein family regulating neurotransmitter release from different perspectives. To do so, we take advantage of distinct experimental models depending on the specific research question. For instance, the experiments presented in this dissertation were performed in acute hippocampal slices, however, sometimes it is more suitable to use other types of model systems, such as cell cultures. In a shared project, we assessed the release properties of transduced hippocampal cell cultures in order to evaluate the impact of a GFP-labeled Cre-recombinase lentivirus on transmitter release.

The following part of the results is less complete and partly contains data being to some degree still preliminary. This subsection exemplifies and documents the establishment of techniques in the lab. In order to evaluate transmitter release in RIM1/2 cDKO cultured hippocampal neurons transduced with RIM1α-GFP fusion protein, we performed electrophysiological recordings in primary hippocampal neuronal cultures transduced with lentiviruses expressing a non-active Cre-recombinase, an active Cre-recombinase, or a GFP-tagged active Cre-recombinase. We attempted to evaluated neurotransmitter release properties by means of two different procedures. On one hand, estimation of P_r by the progressive block of NMDA synaptic currents; and, on the other hand, assessment of the time course of the release rate by the deconvolution of IPSCs.

3.8.1 Assessing P_r using pharmacological blockade of synaptically activated NMDARs by the use-dependent blocker MK-801

P_r can be qualitatively assessed by the blockade of synaptically activated NMDARs by the use-dependent antagonist MK-801 (Rosenmund et al., 1993) (Hessler et al., 1993). MK-801 is an irreversible NMDAR open channel blocker, therefore only those receptors on the synapses that bind glutamate will be blocked, preventing their participation in the subsequent transmission. An increase in P_r leads to more glutamate release and therefore, to more NMDARs activated, leading to a faster rate of the NMDARs blockade by MK-801. Therefore, the rate of progressive decrease is proportional to the P_r.

We recorded NMDAR-mediated EPSCs from single cultured hippocampal neurons and monitored the decline of the amplitude of the NMDAR-mediated synaptic currents as a function of repeated stimulations in the presence of 40 µM of MK-801 (Figure 3.15 A). The progressive block rate was measured by the fitting of a single exponential to the EPSC amplitude, normalized to the peak of the first EPSC peak (Figure 3.15 B). In the experiment shown, the time constant of the decay of the progressive MK-801 block was equal to 181 s.

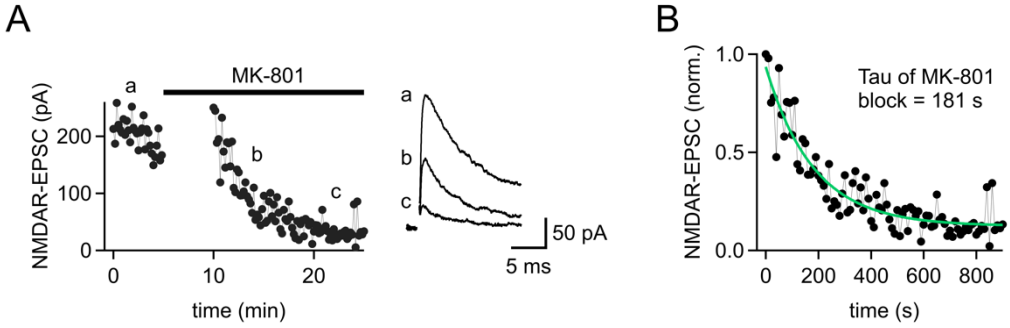

Figure 3.15 Qualitative assessment of P_r by MK-801 blockade of NMDAR-mediated EPSCs. A) Time course of a representative experiment. Stimulation elicited every 10 seconds. Average NMDAR-EPSCs (average response to 10 stimuli) recorded in a WT cultured hippocampal neuron before MK-801 application (a) and an early (b) and late (c) time point after MK-801 application. B) NMDAR-EPSC amplitudes are normalized to the peak of the first response after 40 µM of MK-801 bath application. Exponential fit shown (green). The decay constant (tau) derives from the exponential fit of the NMDAR-EPSCs blockade by MK-801.

3.8.2 IPSCs deconvolution approach

The rate of neurotransmitter release is expressed as the probability per second that a release will occur. After an AP arrives at the presynaptic terminal, the rate of release steeply increases and then drops back to baseline levels within a few milliseconds. The time course of the transmitter release rate can be determined by deconvolution of compound synaptic currents with quantal synaptic responses recorded in the same cell. The deconvolution approach assumes that the compound currents are signals composed of a linear summation of several quantal responses, which represent the postsynaptic response to the presynaptic release of a single quantum.

We performed the deconvolution approach on inhibitory currents recorded from cultured hippocampal neurons. Inhibitory currents are more precisely analyzed in cultured cells when compared to EPSCs, as excitatory currents are often contaminated by hyperexcitability. We recorded IPSCs, the compound currents, and mIPSCs (in the presence of TTX) from the same cultured cell (Figure 3.16 A).

The deconvolution approach was perform using the Fourier transform, which decomposes a signal recorded in time domain to frequency domain. The average IPSCs and the average mIPSCs were converted to a frequency domain by a discrete forward Fourier transformation computed by fast Fourier transform algorithm. The IPSC transform was divided by the mIPSC transform. The frequency domain result was converted to a time domain by an inverse Fourier transform. The result of the inverse transformation represented the time course of the neurotransmitter release rate (Kukley et al., 2007, Neher and Sakaba, 2001, Van der Kloot, 1988).

The deconvolution procedure showed that transmitter release after an AP (Figure 3.16 B and C) is highly synchronized, steeply increased and decreased with high speed, mimicking the velocity of the fast synaptic transmission.

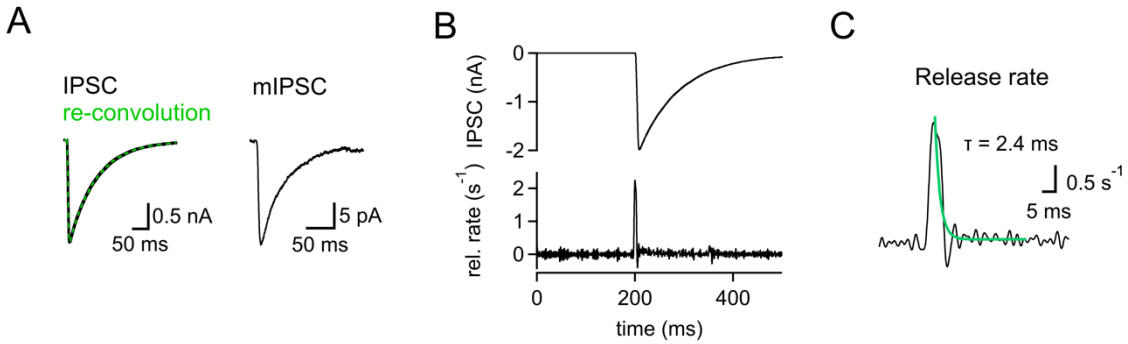

Figure 3.16 IPSCs deconvolution approach. A) Left, superposition of average IPSC trace from 20 traces, and re-convolution (green) of estimated release rate with mIPSC. Right, average mIPSC from 240 miniature events. B) Time course of the IPSC (upper panel) and of the estimated release rate (quanta per s) from experiment showed in A. C) Estimated release rate from panel B with single exponential fit to the decay phase (green).

4 Discussion

Synaptic transmission is extremely fast, tightly regulated, and, at the same time, incredibly plastic, due to, in part, the rapid and spatially restricted presynaptic Ca^{2+} signal at the release sites. The large members of the RIM protein family, α/β-RIMs, serve as multifunctional regulators of synaptic transmission by recruiting VGCCs and release-ready state SVs at the presynaptic AZ (Han et al., 2011, Kaeser et al., 2011). A putative role of the small RIM isoforms, γ-RIMs, controlling presynaptic neurotransmitter release has only begun to be addressed (Alvarez-Baron et al., 2013, Uriu et al., 2010). By means of a newly developed approach based on a Hill equation describing the cooperative Ca^{2+}-binding scheme, electrophysiological recordings, and Ca^{2+} imaging data, we investigated how the main large RIM protein, RIM1α, a known component of the presynaptic structural scaffold, and two small RIMs, RIM3 and RIM4, regulate the functionality of the SV-release machinery and its impact on synaptic transmission and short-term plasticity.

Our data not only are in accordance with previous findings regarding the functional role of α-RIMs but also challenge a previous assumption by showing that RIM proteins differentially control the VGCC subtypes driving synaptic transmission. Five different conclusions can be drawn from our data. First, RIM1α and RIM4 proteins are not essential for normal miniature release. Second, RIM1α is necessary for normal VGCC abundance and localization at the release site, and therefore essential for maintaining sufficient $[Ca^{2+}]_{local}$.Third, our study defined a key feature of RIM1α determining the presynaptic subtype VGCC contribution to the $[Ca^{2+}]_{local}$, and therefore to transmitter release, in a small model CNS synapse. The presence of RIM1α is required to maintain the prominent contribution of N-type VGCCs to synaptic transmission. Fourth, RIM1α is essential for a normal P_{ves}, and consequently, contributes to the regulation of short-term synaptic plasticity. Fifth, the results presented here suggested a possible small presynaptic role for γ-RIMs

regulating synaptic transmission by an antagonistic mechanism with the large RIM isoforms. Taken together, my study highlights a novel function of RIM1α tuning the VGCC subtype level at the presynaptic release site, and a putative role for the γ-RIMs regulating synaptic transmission.

RIM proteins are not essential for spontaneous release

As expected, our data showed an unaltered mEPSCs amplitude in RIM1α KO, and RIM4 KO mice indicating normal postsynaptic responsiveness to quantal release (Figure 3.1 and Figure 3.2). Conditional deletion of all the large RIM isoforms (Deng et al., 2011), deletion of RIM1α/β or RIM2α/β (Kaeser et al., 2012), single deletion of RIM1α (Calakos et al., 2004, Kaeser et al., 2008), and knockdown of RIM4 (Alvarez-Baron et al., 2013) on cultured hippocampal neurons also demonstrated an unchanged quantal size upon alteration of RIM proteins.

In the absence of RIM1α, although it did not reach level of significance, the mean mEPSCs frequency tended to be lower, as reported previously in autaptic cultured hippocampal neurons (Calakos et al., 2004). Our data suggested a specific loss of mEPSC events which occur with a shorter IEI distance (Figure 3.1). This observation could be explained by a decreased P_{ves} during miniature release, by a lower number of release-ready state vesicles, or by a decreased number of synaptic connections. Prior research suggested a slightly larger decrease in inhibitory miniature events upon ablation of RIM1α, emphasized by the removal of the other RIM1 isoform, RIM1β (Kaeser et al., 2008). Deletion of both isoforms encoded by the *Rims1* gene, RIM1α and RIM1β, dramatically decreased excitatory and inhibitory miniature currents suggesting redundancy in the function of RIM1 isoforms (Kaeser et al., 2012, Kaeser et al., 2008). The effect of RIM1α removal on excitatory spontaneous release at the hippocampal CA3-CA1 synapses has not been investigated before. Based on previous research, the weakness of the effect on mEPSCs frequency observed in RIM1α KO mice was likely due to a compensatory effect by other large RIM isoforms, such as RIM1β and RIM2α/β (Han et al., 2015, Kaeser et al., 2012, Kaeser et al., 2008). α/β-RIMs redundantly would regulate spontaneous release.

These data support the idea that the strong effect seen in synaptic strength in RIM1α KO mice is solely due to a decrease in P_r or a decreased number of SVs available for release.

In RIM4 KO deficient mice, mEPSC frequency was unchanged compared to WT. However, knockdown of RIM4 resulted in a markedly reduced mEPSC frequency in cultured hippocampal neurons, which was explained by a decrease in the number of functional synaptic contacts (Alvarez-Baron et al., 2013). The discrepancy between our results and those of the prior study may be due to the difference of the experimental model, and the expression pattern and expression level of RIM4 *in vitro* and *in vivo*. RIM4 may play different roles depending on the synapse type, as it has been reported for other AZ proteins, such as RIM1α (Mittelstaedt et al., 2010).

RIM1α controls the availability of VGCCs at the release site maintaining the release-inducing Ca^{2+} signal

Ca^{2+}-mediated neurotransmitter release upon the arrival of an AP happens in an extremely fast manner. The efficacy of release depends on the density, the positioning, and the modulation of the VGCCs. The molecular mechanisms for setting the levels of the VGCCs and their organization within the AZ are only partly understood. Proteins located at the presynaptic release sites, such as RIM1α, have been identified to recruit and modulate presynaptic VGCCs (Kaeser et al., 2011, Kiyonaka et al., 2007).

Estimates of the coupling distance between VGCCs and SVs are based on the inhibitory effect of exogenous Ca^{2+} chelators on neurotransmitter release. In general, fast synaptic transmission is slightly sensitive to kinetically slow intracellular Ca^{2+} chelators, such as EGTA, due to the great speed of the process and the short distance, on the nanoscale range, between the VGCCs and the vesicle fusion machinery. Thus, EGTA only interferes with the contribution of remote channels to release. The effect of the Ca^{2+} chelator EGTA-AM on Schaffer collaterals-evoked fEPSPs revealed an overall unchanged coupling distance between those remote VGCCs and the docked SVs in RIM1α KO mice compared to WT mice. Besides,

based on the profound analysis of the Ca^{2+} signal driving release, our results revealed a decrease of 20% in the $[Ca^{2+}]_{local}$ seen by the Ca^{2+} sensor of release.

The level of Ca^{2+} saturation of the release machinery influences the inhibitory degree of the Ca^{2+} buffer on neurotransmitter release. If there is low $[Ca^{2+}]_{local}$ at the Ca^{2+} sensor, release is more sensitive to further reduction in Ca^{2+}. During the EGTA-AM experiments, we recorded fEPSPs in 2 mM $[Ca^{2+}]_e$, i.e. control conditions, in WT and RIM1α KO mice. We did not compensate for the decreased $[Ca^{2+}]_{local}$ estimated for the RIM1α KO synapses. Due to the lower $[Ca^{2+}]_{local}$ at RIM1α KO terminals, we expected larger EGTA sensitivity compared to WT mice. However, in contrast, we observed a tendency to lower sensitivity to the Ca^{2+} chelator. The difference in EGTA sensitivity between WT and RIM1α KO would have been even larger after compensating for the decrease in $[Ca^{2+}]_{local}$ estimated for the RIM1α KO mice. In light of all this, we hypothesize that in the absence of RIM1α there is a loss of remote VGCCs normally contributing to release.

At first glance, our Ca^{2+} buffer data were unexpected, as prior research reported a stronger sensitivity of the Ca^{2+}-triggered release to EGTA-AM in RIM1/2 cDKO cultured hippocampal neurons compared to control (Kaeser et al., 2011). The authors proposed that the observed higher EGTA sensitivity in the RIM1/2 cDKO neurons was a consequence of a larger coupling distance between VGCCs and SVs. However, another explanation for these results would be a decreased number of VGCCs driving synaptic transmission, as explained above. Indeed, several studies indicated the decrease in the I_{Ca} after ablation of RIM proteins (Han et al., 2011, Kaeser et al., 2011, Kintscher et al., 2013).

The Ca^{2+} concentration built up around the Ca^{2+} sensor is defined by the number of VGCCs and their location. As aforementioned, we observed a reduction by 20% in the $[Ca^{2+}]_{local}$ in RIM1α KO mice. This result is consistent with a previous finding in the Calyx of Held. By comparison of synaptic data and Ca^{2+} uncaging data, this study estimated a decrease by 25% in the transient $[Ca^{2+}]_{local}$ at RIM1/2 cDKO synapses (Han et al., 2011). It seems plausible that after the removal of RIM proteins, other components of the presynaptic AZ, such as RIM-BPs, mediate Ca^{2+} entry. A direct interaction between RIM-BPs, whose expression levels were not altered upon

RIM1α deletion (Schoch et al., 2002), and different subtype of VGCCs, P/Q-type, N-type, and L-type, has been reported (Hibino et al., 2002). Taking together our results and the previous literature, the most plausible explanation for the RIM1α KO phenotype is the presence of fewer VGCCs located at the release site. Another possible mechanism for RIM1α in normally supporting sufficient $[Ca^{2+}]_{local}$ involves the direct modulation of the VGCCs. It has been hypothesized that the C_2B domain of RIM1α interacts with the β subunit of the VGCCs suppressing voltage-dependent inactivation, and therefore, sustaining Ca^{2+} influx (Kiyonaka et al., 2007). However, no further studies could prove that the loss of this modulation contributes to the impaired Ca^{2+} entry in RIM-deficient mice.

To prove a lower density of VGCCs at RIM1α KO synaptic terminals, we would need to measure the presynaptic I_{Ca}. The Ca^{2+} signal analyzed during our Ca^{2+} imaging experiments arose from an unknown and probably variable population of synapses. Therefore, this approach does not allow to quantify or compare absolute values of presynaptic Ca^{2+} entry. To do so, and therefore, to be able to state a reduced presynaptic Ca^{2+} influx in RIM1α KO mice, it would be necessary to quantify the AP-evoked Ca^{2+} transient at single presynaptic boutons as performed previously at cerebellar parallel fibers (Kintscher et al., 2013).

Shift towards P/Q-type VGCC contribution to the $[Ca^{2+}]_{local}$ in the absence of RIM1α

Preceding studies estimated the contribution of the different subtypes of VGCCs to the presynaptic Ca^{2+} entry that precedes synaptic transmission. The mathematical approach applied to investigate the Ca^{2+} signal mediating neurotransmitter release is beyond previous research, thus allowed us to estimate the contribution of the different subtypes of VGCCs, not to the presynaptic I_{Ca}, but to the $[Ca^{2+}]_{local}$ seen by the Ca^{2+} sensor, as we extensively explained during the results section. The relative contribution of the different VGCC subtypes to the I_{Ca} and to the $[Ca^{2+}]_{local}$ may differ. The relative contribution of the VGCC subtypes to the $[Ca^{2+}]_{local}$ is dependent on the number and the specific position of the VGCCs relative to the SVs, where the Ca^{2+} sensors for release are located.

In comparison to results of previous studies, the selective blockade of N-type VGCCs by Cgtx resulted in a wide range of inhibition potency of synaptic transmission at the Schaffer collateral synapses. The inhibition values by Cgtx, and therefore, the estimated relative contribution of the N-type VGCCs to release, ranged from reductions of synaptic transmission by 30% (Takahashi and Momiyama, 1993) to reductions by approximately 50% (Ahmed and Siegelbaum, 2009, Horne and Kemp, 1991, Wheeler et al., 1994), or even synaptic transmission inhibition by 70% (Luebke et al., 1993, Wu and Saggau, 1994). The contribution of N-type and P/Q-type VGCCs to synaptic transmission estimated from our approach, N_{WT}=52% and P_{WT}=48%, are consistent with previous reported values. The discrepancy observed in the literature could be attributed to the Ca^{2+}-dependence of the blocking potency of the toxin, which depends on the saturation level of the release machinery. Unfortunately, this idea is difficult to validate due to the lack of evidences in the reports to state different levels of occupancy of the Ca^{2+} sensor.

The former estimations of the contribution of the different VGCC subtypes to synaptic transmission were based on the inhibitory effect on the Ca^{2+} entry, but as explained above, the relative VGCC subtype contribution to total I_{Ca} may not reflect the relative contribution to the $[Ca^{2+}]_{local,}$ which ultimately drives neurotransmitter release.

In order to estimate more precisely the different VGCC subtype contribution to the synaptic transmission, an approach to estimate the relative contribution to the $[Ca^{2+}]_{local}$ was needed. Moreover, our experimental approach integrated the study of the release machinery at different levels of Ca^{2+} saturation, by altering $[Ca^{2+}]_e$, and took advantage of a global analysis, i.e. the combination of data from different scenarios of the release machinery in different genetic backgrounds.

Up to now, prior research suggested that the removal of the large RIM isoforms decreased I_{Ca}, however the relative contribution of the different VGCC subtypes has not been evaluated. We analyzed the subtype contribution at a small central synapse, the Schaffer collateral synapse, where release is mediated by the joint actions of P/Q- and N-type VGCCs. Our global analysis of the fractional release after Cgtx and Agatx application revealed that the presynaptic scaffolding protein RIM1α specifically tunes the contribution of N-type VGCCs to synaptic transmission. We

observed similar contribution of P/Q- and N-type VGCCs, 52% and 48%, respectively, to the $[Ca^{2+}]_{local}$ mediating neurotransmitter release at WT Schaffer collateral synapses. However, in RIM1α KO synapses, there was a shift to the P/Q-type population as the predominant Ca^{2+} source to the $[Ca^{2+}]_{local}$. The estimated relative contribution of P/Q-type VGCCs was 65%, whereas the N-type contribution was 29%.

The shifting of the reliance of neurotransmitter release towards P/Q-type VGCC in RIM1α KO mice suggests a preferential tethering of N-type VGCCs at the release site by RIM1α. On one hand, in a WT scenario, the density, and localization of both subtypes of VGCCs, N-type and P/Q-type, are regulated by several AZ proteins. It was reported that the presynaptic protein Bassoon, via its interaction with RIM-BP, functions in specifically localizing P/Q-type VGCCs at the AZ (Davydova et al., 2014). Moreover, another AZ protein, Munc13-3, was recently identified as a regulator of the positioning of P/Q-type VGCCs in the cerebellar parallel fiber to Purkinje neuron synapse (Kusch et al., 2018). On the other hand, in a RIM1α-deficient scenario, other presynaptic AZ proteins, such as RIM-BP, may play a larger role in controlling the VGCC subtype contribution. As we pointed out earlier, our results revealed that in the absence of RIM1α there may be fewer VGCCs at the release site. The removal of RIM1α may affects only N-type subtype, or P/Q- and N-types, thus RIM proteins interact directly with both VGCCs. In any case, the $[Ca^{2+}]_{local}$ is decreased, leading to a lower $[Ca^{2+}]_{local}$, and the relative contribution changes towards P/Q-type in the absence of RIM1α because, as mentioned earlier, other AZ proteins still present at the AZ, such as RIM-BP, would preferentially attach them. The scenario observed in RIM1α KO mice would be the result of a preferential tethering of N-type VGCCs by RIM1α, and the preference of other AZ proteins, which interact with both subtypes, recruiting P/Q-type VGCCs.

A potential molecular mechanism to explain the specific tethering of the N-type VGCCs by RIM1α involves a specific region of the $Ca_v2.2$ pore forming α_1 subunit known as the synaptic protein interaction (synprint) region. RIM1α interacts with the C-terminal of the α_1 subunit of P/Q-type and N-type VGCC, but moreover, RIM1α has been suggested to interact with the synprint region of the N-type VGCCs

(Coppola et al., 2001). This additional interaction between RIM1α and the N-type VGCCs could explain the preferential tethering of N-type VGCCs by RIM1α. Furthermore, it has been reported that the N-type VGCCs are a cyclin-dependent kinase 5 (Cdk5) substrate. Phosphorylation of the N-type VGCC by Cdk5, which modulates the interaction between the channel and RIM1α, increases Ca^{2+} influx, facilitating neurotransmitter release (Su et al., 2012). According to this, a specific modulation of N-type VGCCs can boost Ca^{2+} entry through this VGCC subtype, rendering N-type VGCCs more efficient triggering release even if they are not tighter coupled to the SVs. This idea opens the possibility for a scenario where the N-type VGCCs attached to RIM1α are more efficient in triggering release due to their regulation, and not because they are closer to the SVs. In the absence of RIM1α, the N-type VGCC loosely coupled to the release machinery would lose influence on the $[Ca^{2+}]_{local}$ and consequently the P/Q-type VGCC contribution to the $[Ca^{2+}]_{local}$, would increase, via interactions with other AZ proteins, which may tether preferentially P/Q-type VGCCs. Moreover, the remote N-type VGCCs would disappear from the release site changing the spatiotemporal profile of the presynaptic VGCC domain. The slightly lower EGTA-AM sensitivity observed in our recordings, although it seemed only a trend, it would be in agreement with the loss of the remote N-type VGCC in the absence of RIM1α.

In summary, our data strongly implies an important role of RIM1α specifically controlling the contribution of N-type VGCCs to synaptic transmission. RIM1α could shorten the distance between the N-type VGCC and the release site or specifically regulate the N-type channels, maybe via the interaction with the N-type VGCC synprint region. Future analysis will be needed to shed light on the postulated mechanism behind this specificity. Moreover, to support our findings it would be interesting to analyze the regulation of the expression of the different VGCC subtypes in the absence of RIM1α as well as the position of the different VGCC subtypes in the presynaptic terminals.

Restoration of normal VGCC subtype contribution to the $[Ca^{2+}]_{local}$ after α/β-RIMs removal

Why does the deletion of one RIM isoform, RIM1α, which has a partial effect on basic neurotransmitter release due to its redundancy with other RIM isoforms, tune the subtype VGCC contribution to $[Ca^{2+}]_{local}$? In an attempt to address this question, we analyzed the specific blockade of N-type VGCC by Cgtx in mice lacking all the large RIM isoforms, i.e. RIM1α/β and RIM2α/β, specifically at Schaffer collateral synapses. Unexpectedly, the decrease of release by Cgtx in the RIM1/2 cDKO mice was similar to the one observed in WT mice, suggesting a restoration of the RIM1α KO phenotype after the removal of all large RIM isoforms. The observed difference in the inhibitory effect cannot be explained only by the inability to virally transduce all CA3 pyramidal cells. With our recombination efficiency (80%), we expected a decrease by Cgtx to approximately 57%, but we observed a larger degree of inhibition, a reduction to 50%. Noteworthy to mention is that a more suitable approach than the extracellular stimulation applied in these experiments would increase the trust in this result. The use of adeno-associated virus driving bicistronic expression of both channelrhodopsin and RIM1/2 deletion would allow the optical stimulation of only those fibers where the large RIM proteins were not expressed.

RIM1 and RIM2 isoforms exhibit different degrees of redundancy for different processes during neurotransmitter release (Kaeser et al., 2012, Kaeser et al., 2008). While all large RIM proteins mainly present the same structural domains, it is possible that through several cellular mechanisms, such as phosphorylation and ubiquitination, they differentially mediate several aspects of neurotransmitter release, such as the novel role defined for RIM1α enhancing N-type VGCC contribution to synaptic transmission. In a RIM1α KO scenario, other RIM isoforms may not recruit N-type VGCC to the release site, decreasing their relative contribution to synaptic transmission, meantime they interact with other AZ proteins enhancing the contribution of P/Q-type VGCCs. In a cDKO scenario, the remaining AZ proteins are maybe differentially regulated and recruit VGCCs to the release site in a different manner, restoring control VGCC subtypes relative contribution.

Nevertheless, to give a larger power to our Sc-CA1 specific cDKO data we would need to improve the technical approach as well as perform a deeper analysis of the Ca^{2+} signal-mediating neurotransmitter release by means of our fractional release Ca^{2+} curve approach.

Ca^{2+} sensitivity of release in RIM1α KO mice

The distance between VGCCs and the vesicle fusion machinery, the magnitude of the $[Ca^{2+}]_{local}$, and the intrinsic Ca^{2+} sensitivity, i.e. intrinsic properties of the Ca^{2+} sensor of release, have a great impact on controlling the speed and efficacy of release.

The analysis of the release kinetics, although the data are not significantly different maybe due to small sample size, suggested a trend towards a decelerated fast neurotransmitter release in RIM1α KO mice. The slowdown of release could be explained by the decrease in $[Ca^{2+}]_{local}$, which would affect P_{ves} and the temporal pattern of transmitter release. The kinetics parameters, such as the synaptic delay, the rise time, or the decay, become faster upon increasing Ca^{2+} influx. Deficits on neurotransmitter release due to impaired Ca^{2+} entry can be overcome by increasing $[Ca^{2+}]_e$. If the kinetics deficits observed in RIM1α KO mice are solely due to alterations in the Ca^{2+} entry, increasing the $[Ca^{2+}]_e$ would restore the kinetics. The release kinetics in RIM1α KO mice in high $[Ca^{2+}]_e$ should behave as the kinetics in WT mice in control conditions, i.e. 2 mM $[Ca^{2+}]_e$. In RIM1α KO mice we observed a decrease by 20% in the Ca^{2+} entry, thus increasing $[Ca^{2+}]_e$ from 2 to 4 mM, which increases Ca^{2+} entry by practically 50%, should overcome the slower release observed in RIM1α KO mice. This would indicate that the neurotransmitter release deficits seen in RIM1α KO mice originate only from Ca^{2+} deficits. If the kinetics parameters are not completely restored by increasing Ca^{2+} entry, the release deficits in RIM1α KO are a consequence of a simultaneous deficit in Ca^{2+}, and alterations at the release machinery, as a decrease in the number of release-ready state SVs.

The synaptic delay becomes shorter when increasing $[Ca^{2+}]_e$ from 2 to 4 mM, but not from 4 to 20 mM. The rise time behaves similar in 2 and 4 mM $[Ca^{2+}]_e$, but

becomes faster in 20 mM. The tau of decay seems to be constant among the different $[Ca^{2+}]_e$ in RIM1α KO mice suggesting that the release does not accelerate correspondingly to an increase Ca^{2+} entry. Taken together, it seems that the kinetics parameters cannot be restored solely by increasing Ca^{2+} entry, which implies that the deficits in neurotransmitter release observed in RIM1α KO mice are due to an impaired Ca^{2+} entry together with an alteration in the RRP size.

RIM1α regulates release probability and short-term synaptic plasticity

Our findings indicate that the primary cause for the reduced P_{ves} in RIM1α KO mice estimated from the fractional release Ca^{2+} curves, similar to previously published values (Han et al., 2011), was the reduction in the $[Ca^{2+}]_{local}$. The stronger reduction in P_r and synaptic strength observed upon ablation of RIM proteins (Calakos et al., 2004, Han et al., 2011, Kaeser et al., 2011, Schoch et al., 2002) could be explained as a functional consequence of the reduced P_{ves} and a simultaneous reduced RRP size (Calakos et al., 2004, Fernandez-Busnadiego et al., 2013, Han et al., 2011, Kaeser et al., 2011). Up to now, the size of the RRP in RIM-deficient mice has been addressed by electrophysiological techniques and transmission electron tomography. The reports indicated a strong reduction in the RRP size upon the removal of RIM1α in autaptic neurons (Calakos et al., 2004), and in RIM1/2 cDKO cultured hippocampal neurons and at the Calyx of Held (Han et al., 2011, Kaeser et al., 2011). The estimated reduction in the $[Ca^{2+}]_{local}$ for RIM1α KO presynaptic terminals, calculated by the fractional release Ca^{2+} curves, and a decrease in the RRP size would account for the strong reduction in AP-mediated neurotransmitter release.

Short term synaptic plasticity, considered mainly a presynaptic phenomenon, implies the processing and integration of information into adaptable patterns of release. We observed an increased PPF upon ablation of RIM1α. The classical explanation for an increased PPF involves a decreased P_{ves} due to the reduction in the $[Ca^{2+}]_{local}$. However, another interesting idea arises after recently a specific Ca^{2+} sensor mediating facilitation, Syt7, was reported (Jackman et al., 2016). The deletion of

RIM1α could alter the function of Syt7 at the SVs, with an increased influence of Syt7 molecules, located on the plasma membrane, which would increase facilitation. This idea brings up new questions: How is the expression of the different Ca^{2+} sensors regulated? Is it possible that in the absence of RIM1α there is a decrease in the number of Syt1 molecules, altering fast synaptic transmission, and at the same time, an increase in the number of Syt7 molecules, increasing facilitation? A more detailed evaluation of the nature of the Ca^{2+} sensors after removal of RIM1α would be needed to get a deeper understanding of the functional importance of RIM1α regulating basic neurotransmitter release and the temporal pattern of release upon repetitive stimulations.

The impact of the larger P/Q-type VGCC contribution to the $[Ca^{2+}]_{local}$ on P_r and synaptic transmission is difficult to resolve, as the magnitude and the time course of the Ca^{2+} influx through different VGCC subtypes is similar. Previous studies have shown the influence of differential VGCC subtype recruitment on P_r by expressing N-type VGCC in P/Q-type-mediated synaptic transmission synapses, like the mature Calyx of Held (Inchauspe et al., 2007) . Further studies are warranted to elucidate a functional outcome of the shift towards P/Q-type VGCCs observed in RIM1α KO mice. In summary, the decrease of P_r and the enhanced PPF observed in RIM1α KO mice are likely to be the consequence of a decrease $[Ca^{2+}]_{local}$ in combination with a decreased number of docked SVs at the presynaptic AZ.

Functional antagonism of α/β-RIMs by γ-RIMs

It has been suggested that γ-RIMs, as well as α-RIMs, bind directly to the β subunit of the VGCCs and modulate their opening times, although in a much less efficient manner than α-RIMs. Moreover, a competition between α-RIMs and γ-RIMs in binding to the β subunit of the VGCCs was shown to impact SVs docking (Uriu et al., 2010). Based on previous literature, the broader subcellular localization pattern of the γ-RIMs (Alvarez-Baron et al., 2013), the high homology of the RIM C_2B domain present in all RIM isoforms, and the partial overlap of known binding partners of γ-RIMs with those of α-RIMs (Wang and Südhof, 2002), we initially hypothesized that

γ-RIMs modulate synaptic release by competing with α-RIMs and impact α-RIMs' role in synaptic transmission. The results from the RIM4 KO fractional release Ca^{2+} curve suggests an opposite scenario to the one observed in RIM1α KO mice. After the removal of RIM4, the estimated Ca^{2+} entry and P_{ves} were increased, and the N-type VGCCs contributed to a larger extent to the $[Ca^{2+}]_{local}$ compared to control conditions. The effect on release after RIM3 ablation follows the same tendency as the RIM4 effect but in a less pronounced manner.

Several mechanisms could explain a functional antagonism between RIM1α and γ-RIMs. γ-RIMs could block slots of RIM1α at the presynaptic AZ and thereby interfere with the interaction of RIM1α and other AZ proteins altering the proper functionality of RIM1α mediating neurotransmitter release. γ-RIMs could act as quenchers, sequestering RIM1α binding partners. They could compete with RIM1α binding to the β subunit of the VGCC and lower the precise localization of SVs at the release site. Another mechanism would involve the heterodimerization between the C_2B domains of RIM1α and γ-RIMs (Guan et al., 2007). In this last situation, the dimerization would change the structure of RIM1α rendering the protein less efficient to interact with other AZ proteins, like Munc13 or RIM-BP, directly to the VGCCs or to Rab3, located at the SVs.

In all of the above-mentioned scenarios, the function of RIM1α in regulating SV exocytosis at the AZ would be affected, thus hampering neurotransmitter release. The removal of γ-RIMs would give RIM1α more control over presynaptic function. In the absence of γ-RIMs we would expect a larger I_{Ca}, a shift towards N-type VGCC contribution to the $[Ca^{2+}]_{local}$, increased $[Ca^{2+}]_{local}$ and P_{ves}, increased RRP size, and decreased PPF. Our results from the RIM3 KO and RIM4 KO fractional release Ca^{2+} curves, and the PPF analysis partly reflected this scenario, suggesting a putative functional antagonism of the large RIM isoforms, such as RIM1α, by the small RIM isoforms. Nevertheless, the γ-RIM KO fractional release Ca^{2+} curves data should be treated with care, as they would require to be verified by the application of the specific P/Q-type VGCC as well as a global analysis of the data. Further studies to investigate the Ca^{2+} entry, the P_r, the arrangement of SVs at the release site, and

the implications in different synaptic plasticity mechanisms, would be warranted to elucidate the possible role of the small RIM isoforms regulating presynaptic neurotransmitter release.

Outlook

The current study identified a novel function for the presynaptic AZ protein RIM1α namely enhancing the contribution of the N-type VGCCs to synaptic transmission, and a possible antagonistic mechanism between RIM1α and the small RIM isoforms, RIM3 and RIM4.

What are the mechanisms through which RIM1α enhances specifically the N-type VGCC contribution to neurotransmitter release? Is it due to an emphasized physical interaction or through a direct regulatory mechanisms of the N-type VGCCs? And, in any of both possibilities, what would be the underlying molecular mechanisms? Is the expression or trafficking of N-type VGCC to the release sites regulated by RIM1α? Would an additional insertion of N-type VGCCs in the absence of RIM1α restore normal synaptic transmission? This last idea is difficult to test because the overexpression of the pore-forming α subunit, although not the specific N-type, failed to change synaptic VGCC abundance or function at the release site (Hoppa et al., 2012).

Are the Ca^{2+} sensors triggering neurotransmitter release altered in the absence of RIM proteins? How does RIM1α regulate short-term synaptic plasticity? And, how would alterations in the temporal pattern of release upon ablation of RIM1α affect information processing and presynaptic computation? What are the molecular mechanisms behind the possible functional antagonism of RIM1α function by γ-RIMs?

5 Abstract

Synaptic transmission is extremely fast and tightly regulated due to the rapid and spatially restricted Ca^{2+} signal at the presynaptic AZ. At the AZ, VGCCs are kept in close proximity to SVs allowing fast and reliable neurotransmitter release. The composition and state of the presynaptic AZ determine P_r, by influencing P_{ves} and the availability of SVs for release, determinants of the synaptic strength. The large RIM proteins, such as RIM1α, are considered the main scaffolding components of the AZ due to their multiple interactions with other AZ proteins as well as with VGCCs and SVs. RIM1α plays a crucial role in the regulation of synaptic transmission by maintaining sufficient and localized Ca^{2+} entry and by maintaining SVs in a release-ready state. The ablation of RIM1α leads to a strong reduction of synaptic output (~40%). The mechanisms by which RIM1α regulates synaptic strength are still not precisely known. It remains unclear whether the alterations in release observed in RIM1α KO mice are caused by a lack of docked SVs or by a decrease in the $[Ca^{2+}]_{local}$ operating the Ca^{2+} sensor, which would impact directly P_{ves}. To evaluate the role of RIM1α in synaptic transmission is essential to get a better understanding on its function regulating different aspects of the release-inducing Ca^{2+} signal, such as VGCC trafficking, tethering, or VGCC subtype specificity. Apart from the large RIM isoforms, the small RIM isoforms RIM3 and RIM4, which consist only of the RIM C-terminal C_2B domain, may play a role in synaptic transmission due to their broader subcellular localization pattern, the high homology of the RIM C_2B domain, and the partial overlap of binding partners with those of RIM1α.

Through electrophysiological recordings and Ca^{2+} imaging data, we investigated the role of RIM1α, RIM3, and RIM4 regulating neurotransmitter release properties and its impact on short-term synaptic plasticity. We developed a mathematical approach, based on a Hill equation describing the cooperative Ca^{2+}-binding scheme, to quantitatively analyze the Ca^{2+}-dependence of the inhibitory effect on Schaffer-

collateral fEPSPs caused by specific VGCC blockers, Cgtx and Agatx, and infer the degree of Ca^{2+} binding to the sensor in the presence and absence of the RIM proteins. This analysis revealed for the first time that the $[Ca^{2+}]_{local}$ and the P_{ves} are reduced by ~20% in RIM1α KO mice indicating that the remaining reduction in synaptic output is caused by a lack of releasable vesicles. Interestingly, the subtype contribution of the VGCCs to activate the Ca^{2+} sensor also differed: while N- and P/Q-type VGCCs equally contributed to the activation of the Ca^{2+} sensor (52%, 48%) in WT mice, the fractional contribution was strongly shifted towards P/Q-type VGCCs in KO mice (65%, 29%). This scenario favor the view that RIM1α deletion decreases synaptic strength by reducing the number of releasable SVs and altering the release-inducing Ca^{2+} signal by a distorted channel-vesicle geometry or by an altered specific N-type VGCC regulation, which causes a decrease in P_r, affecting synaptic strength. The removal of the γ-RIMs affected release properties in a lesser extent as RIM1α ablation. We observed in RIM4 KO data a tendency towards an opposite scenario to the one observed in RIM1α KO mice. The $[Ca^{2+}]_{local}$ and the P_{ves} were slightly increased in concert with a shift towards N-type VGCC contribution to the $[Ca^{2+}]_{local}$. Our data pointed out to a novel function for RIM1α specifically enhancing the contribution of N-type VGCC to synaptic transmission, and a possible small presynaptic role for RIM4 regulating synaptic transmission by an antagonistic mechanism with RIM1α.

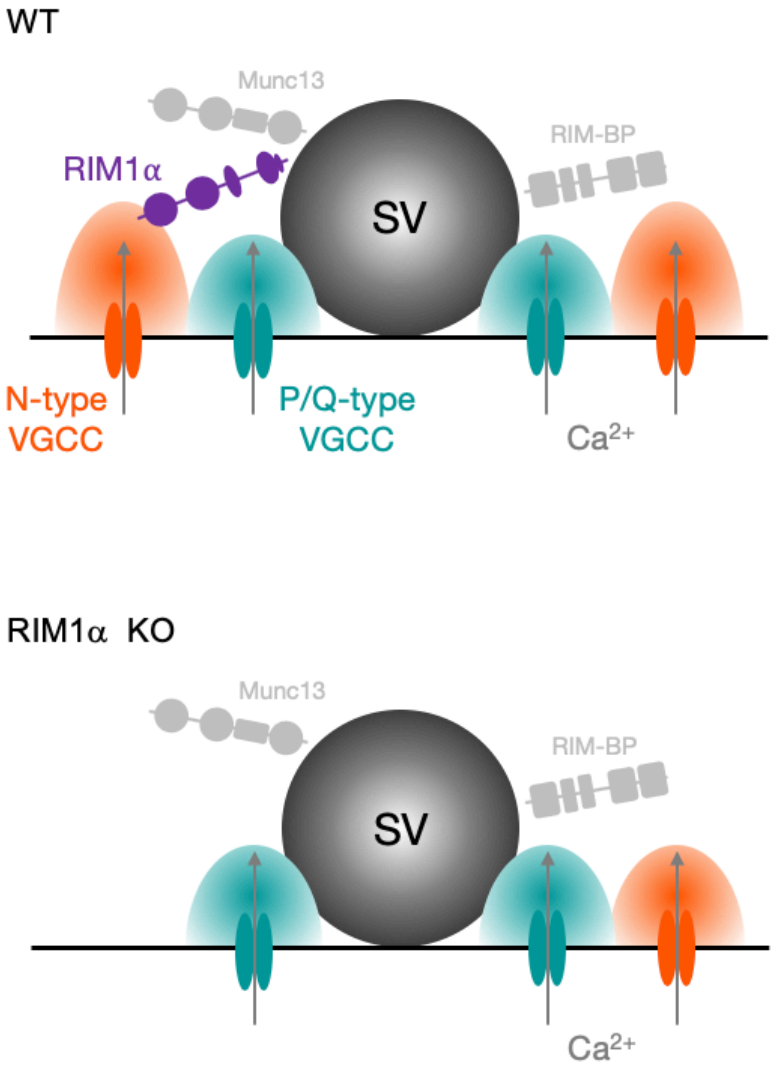

Figure 5.1 Graphical abstract. In the absence of RIM1α there is a shift towards P/Q-type VGCC contribution to the local Ca^{2+} concentration seen by the sensor after an AP. Our data suggest a loss of remote N-type VGCCs which in normal conditions are specifically regulated by RIM1α. The loss of presynaptic VGCC, likely the remote N-type, reduces the $[Ca^{2+}]_{local}$ and P_{ves} by approximately 20%. The decrease in $[Ca^{2+}]_{local}$ together with a decrease in the number of SVs ready for release could explain the strong reduction in synaptic strength observed in RIM1α KO mice.

6 List of figures

7 Bibliography

Abbott L F, Regehr W G. *Synaptic computation*. Nature 2004; 431: 796-803

Acuna C, Liu X, Su T C, Acuna C, Liu X, Gonzalez A, Su T C. *RIM-BPs Mediate Tight Coupling of Action Potentials Article RIM-BPs Mediate Tight Coupling of Action Potentials to Ca2+ -Triggered Neurotransmitter Release*. Neuron 2015; 87: 1234-1247

Ahmed M S, Siegelbaum S A. *Recruitment of N-Type Ca2+ channels during LTP enhances low release efficacy of hippocampal CA1 perforant path synapses*. Neuron 2009; 63: 372-385

Alvarez-Baron E, Michel K, Mittelstaedt T, Opitz T, Schmitz F, Beck H, Dietrich D, Becker A J, Schoch S. *RIM3 and RIM4 are key regulators of neuronal arborization*. The Journal of Neuroscience 2013; 33: 824-839

Andersen P, Morris R, Amaral D, Bliss T, O'Keefe J. The hippocampus book. New York, Oxford University Press. 2007

Augustin I, Rosenmund C, Sudhof T C, Brose N. *Munc13-1 is essential for fusion competence of glutamatergic synaptic vesicles*. Nature 1999; 400: 457-561

Augustine G J, Charlton M P, Smith S J. *Calcium entry and transmitter release at voltage-clamped nerve terminals of squid*. Journal of Physiology 1985; 367: 163-181

Bean B P. *Classes of calcium channels in vertebrate cells*. Annual review of physiology 1989; 51: 367-384

Bliss T V, Collingridge G L. *A synaptic model of memory: long-term potentiation in the hippocampus*. Nature 1993; 361: 31-39

Borst J G G, Sakmann B. *Calcium influx and transmitter release in a fast CNS synapse*. Nature 1996; 383: 431-434

Brose N, Petrenko A G, Sudhof T C, Jahn R. *Synaptotagmin: a calcium sensor on the synaptic vesicle surface*. Science 1992; 256: 1021-1025

Calakos N, Schoch S, Südhof T C, Malenka R C. *Multiple roles for the active zone protein RIM1alpha in late stages of neurotransmitter release*. Neuron 2004; 42: 889-896

Carbone E, Lux H D. *Kinetics and selectivity of a low-voltage-activated calcium current in chick and rat sensory neurons*. Journal of Physiology 1987; 386: 547-570

Castillo J, Katz B. *Quantal components of the end-plate potential*. Journal of Physiology 1954; 124: 560-573

Castillo P E, Schoch S, Schmitz F, Sudhof T C, Malenka R C. *RIM1alpha is required for presynaptic long-term potentiation*. Nature 2002; 415: 327-330

Catterall W A. *Structure and regulation of voltage-gated Ca2+ channels*. Annu Rev Cell Dev Biol 2000; 16: 521-555

Choi S, Yu E, Lee S, Llinas R R. *Altered thalamocortical rhythmicity and connectivity in mice lacking Cav3.1 T-type Ca2+ channels in unconsciousness*. Proceedings of the National Academy of Sciences 2015; 112: 7839-7844

Christie J M, Jahr C E. *Multivesicular Release at Schaffer Collateral–CA1 Hippocampal Synapses*. The Journal of Neuroscience 2006; 26: 210-216

Clements J D, Bekkers J M. *Detection of spontaneous synaptic events with an optimally scaled template*. Biophysical Journal 1997; 73: 220-229

Coppola T, Magnin-Lüthi S, Perret-Menoud V, Gattesco S, Schiavo G, Regazzi R. *Direct Interaction of the Rab3 Effector RIM with Ca2+ Channels, SNAP-25, and Synaptotagmin*. Journal of Biological Chemistry 2001; 276: 32756-32762

Davydova D, Marini C, King C, Klueva J, Bischof F, Romorini S, Montenegro-Venegas C, Heine M, Schneider R, Schroder M S, Altrock W D, Henneberger C, Rusakov D A, Gundelfinger E D, Fejtova A. *Bassoon specifically controls presynaptic P/Q-type Ca2+ channels via RIM-binding protein*. Neuron 2014; 82: 181-194

De Jong A, Roggero M, Ho R, Wong Y, Brautigam A, Rizo J, Kaeser P S. *RIM C2B Domains Target Presynaptic Active Zone Functions to PIP2-Containing Membranes*. Neuron 2018; 98: 335-349

Deng L, Kaeser P S, Xu W, Südhof T C. *RIM proteins activate vesicle priming by reversing autoinhibitory homodimerization of Munc13*. Neuron 2011; 69: 317-331

Dodge F A, Rahamimoff R. *Co-operative action of calcium ions in transmitter release at the neuromuscular junction*. Journal of Physiology 1967; 193: 419-432

Dong W, Radulovic T, Goral R O, Thomas C, Suarez Montesinos M, Guerrero-Given D, Hagiwara A, Putzke T, Hida Y, Abe M, Sakimura K, Kamasawa N, Ohtsuka T, Young S M. *CAST/ELKS Proteins Control Voltage-Gated Ca2+ Channel Density and Synaptic Release Probability at a Mammalian Central Synapse* Cell Reports 2018; 24: 284-293

Dunlap K, Luebke J I, Turner T J. *Exocytotic Ca2+ channels in mammalian central neurons*. Trends in Neurosciences 1995; 18: 89-98

Eggermann E, Bucurenciu I, Goswami S P, Jonas P. *Nanodomain coupling between Ca2+ channels and sensors of exocytosis at fast mammalian synapses*. Nature Review Neuroscience 2011; 13: 7-21

Erdmann E, Rupprecht V, Matthews E, Kukley M, Schoch S, Dietrich D. *Depression of release by mGluR8 alters Ca2+ dependence of release machinery*. Cerebral Cortex 2012; 22: 1498-1509

Fernandez-Busnadiego R, Asano S, Oprisoreanu A M, Sakata E, Doengi M, Kochovski Z, Zurner M, Stein V, Schoch S, Baumeister W, Lucic V. *Cryo-electron tomography reveals a critical role of RIM1alpha in synaptic vesicle tethering*. Journal of Cell Biology 2013; 201: 725-740

Fernandez-Chacon R, Konigstorfer A, Gerber S H, Garcia J, Matos M F, Stevens C F, Brose N, Rizo J, Rosenmund C, Sudhof T C. *Synaptotagmin I functions as a calcium regulator of release probability*. Nature 2001; 410: 41-49

Geppert M, Goda Y, Hammer R E, Li C, Rosahi T W, Stevens C F, Südhof T C. *Synaptotagmin I: A Major Ca2+ Sensor for Transmitter Release at a Central Synapse*. Cell 1994; 79: 717-727

Gracheva E O, Hadwiger G, Nonet M L, Richmond J E. *Direct interactions between C. elegans RAB-3 and Rim provide a mechanism to target vesicles to the presynaptic density*. Neuroscience Letters 2008; 444: 137-142

Guan R, Dai H, Tomchick D R, Dulubova I, Machius M, Sudhof T C, Rizo J. *Crystal structure of the RIM1alpha C2B domain at 1.7 A resolution*. Biochemistry 2007; 46: 8988-8998

Haas H L, Schaerer B, Vosmansky M. *A simple perfusion chamber for the study of nervous tissue slices in vitro*. Journal of Neuroscience Methods 1979; 1: 323-325

Han Y, Babai N, Kaeser P S, Südhof T C, Schneggenburger R. *RIM1 and RIM2 redundantly determine Ca2+ channel density and readily releasable pool size at a large hindbrain synapse*. Journal of Neurophysiology 2015; 113: 255-263

Han Y, Kaeser P S, Südhof T C, Schneggenburger R. *RIM Determines Ca2+ Channel Density and Vesicle Docking at the Presynaptic Active Zone*. Neuron 2011; 69: 304-316

Held R G, Liu C, Kaeser P S. *ELKS controls the pool of readily releasable vesicles at excitatory synapses through its N-terminal coiled-coil domains*. eLife 2016; 5: 1-20

Hessler N a, Shirke a M, Malinow R. *The probability of transmitter release at a mammalian central synapse*. Nature 1993; 366: 569-572

Hibino H, Pironkova R, Onwumere O, Vologodskaia M, Hudspeth A J, Lesage F. *RIM binding proteins (RBPs) couple Rab3-interacting molecules (RIMs) to voltage-gated Ca2+ channels*. Neuron 2002; 34: 411-423

Hille B. *Modulation of ion-channel function by G-protein-coupled receptors*. Trends in Neurosciences 1994; 17: 531-536

Holderith N, Lorincz A, Katona G, Rózsa B, Kulik A, Watanabe M, Nusser Z. *Release probability of hippocampal glutamatergic terminals scales with the size of the active zone*. Nature Neuroscience 2012; 15: 988-997

Hoppa M B, Lana B, Margas W, Dolphin A C, Ryan T A. *alpha2delta expression sets presynaptic calcium channel abundance and release probability*. Nature 2012; 486: 122-125

Horne A L, Kemp J A. *The effect of w-conotoxin GVIA on synaptic transmission within the nucleus accumbens and hippocampus of the rat in vitro*. British Journal of Pharmacology 1991; 103: 1733-1739

Huang Y Y, Zakharenko S S, Schoch S, Kaeser P S, Janz R, Sudhof T C, Siegelbaum S A, Kandel E R. *Genetic evidence for a protein-kinase-A-mediated presynaptic component in NMDA-receptor-dependent forms of long-term synaptic potentiation*. Proceedings of the National Academy of Sciences 2005; 102: 9365-9370

Inchauspe C G, Forsythe I D, Uchitel O D. *Changes in synaptic transmission properties due to the expression of N-type calcium channels at the calyx of Held*

synapse of mice lacking P/Q-type calcium channels. Journal of Physiology 2007; 584: 835-851

Jackman S L, Turecek J, Belinsky J E, Regehr W G. *The calcium sensor synaptotagmin 7 is required for synaptic facilitation*. Nature 2016; 529: 88-91

Johnston D, Wu S. Foundations of cellular neurophysiology. Cambridge, Massachusetts, The MIT Press. 1995

Kaeser P S, Deng L, Fan M, Sudhof T C. *RIM genes differentially contribute to organizing presynaptic release sites*. Proceedings of the National Academy of Sciences 2012; 109: 11830-11835

Kaeser P S, Deng L, Wang Y, Dulubova I, Liu X, Rizo J, Südhof T C. *RIM proteins tether Ca2+ channels to presynaptic active zones via a direct PDZ-domain interaction*. Cell 2011; 144: 282-295

Kaeser P S, Kwon H B, Chiu C Q, Deng L, Castillo P E, Sudhof T C. *RIM1alpha and RIM1beta are synthesized from distinct promoters of the RIM1 gene to mediate differential but overlapping synaptic functions*. The Journal of Neuroscience 2008; 28: 13435-13447

Kamiya H, Sawada S, Yamamoto C. *Synthetic o-conotoxin blocks synaptic transmission in the hippocampus in vitro*. Neuroscience Letters 1988; 91: 84-88

Katz B, Miledi R. *The effects of calcium on acetylcholine release from motor nerve terminals*. Proceedings of the Royal Society B 1965; 161: 496-503

Katz B, Miledi R. *The role of calcium in neuromuscular facilitation*. Journal of Physiology 1968; 195: 481-492

Kintscher M, Wozny C, Johenning F W, Schmitz D, Breustedt J. *Role of RIM1alpha in short- and long-term synaptic plasticity at cerebellar parallel fibres*. Nature Communications 2013; 4

Kiyonaka S, Wakamori M, Miki T, Uriu Y, Nonaka M, Bito H, Beedle A M, Mori E, Hara Y, De Waard M, Kanagawa M, Itakura M, Takahashi M, Campbell K P, Mori Y. *RIM1 confers sustained activity and neurotransmitter vesicle anchoring to presynaptic Ca2+ channels*. Nature Neuroscience 2007; 10: 691-701

Knierim J J. *The hippocampus*. Current Biology 2015; 25: 1116-1121

Körber C, Kuner T. *Molecular Machines Regulating the Release Probability of Synaptic Vesicles at the Active Zone*. Frontiers Synaptic Neuroscience 2016; 8

Kukley M, Capetillo-Zarate E, Dietrich D. *Vesicular glutamate release from axons in white matter*. Nature Neuroscience 2007; 10: 311-320

Kusch V, Bornschein G, Loreth D, Bank J, Jordan J, Baur D, Watanabe M, Kulik A, Heckmann M, Eilers J, Schmidt H. *Munc13-3 Is Required for the Developmental Localization of Ca2+ Channels to Active Zones and the Nanopositioning of Cav2.1 Near Release Sensors*. Cell Reports 2018; 22: 1965-1973

Lee A, Wong S T, Gallagher D, Li B, Storm D R, Scheuer T, Catterall W A. *Ca2+/calmodulin binds to and modulates P/Q-type calcium channels*. Nature 1999; 399: 155-159

Liaw J-s, Berger T W. *Dynamic Synapse: A New Concept of Neural Representation and Computation*. Hippocampus 1996; 6: 591-600

Llinas R, Nicholson C. *Calcium Role in Depolarization-Secretion Coupling : An Aequorin Study in Squid Giant Synapse*. Proceedings of the National Academy of Sciences 1975; 72: 187-190

Llinas R, Sugimori M, Silver R B. *Microdomains of High Calcium Concentration in a Presynaptic Terminal*. Science 1992; 256: 677-680

Luebke J I, Dunlap K, Turner T J. *Multiple calcium channel types control glutamatergic synaptic transmission in the hippocampus*. Neuron 1993; 11: 895-902

Mackler J M, Drummond J A, Loewen C A, Robinson I M, Reist N E. *The C2B Ca2+-binding motif of synaptotagmin is required for synaptic transmission in vivo*. Nature 2002; 418: 340-344

Martin S J, Clark R E. *The rodent hippocampus and spatial memory: from synapses to systems*. Cell Molecular Life Science 2007; 64: 401-431

Mayford M, Siegelbaum S A, Kandel E R. Synapses and Memory Storage. Cold Spring Harbor Laboratory Press. 2012

Meinrenken C J, Borst J G, Sakmann B. *Calcium secretion coupling at calyx of Held governed by nonuniform channel-vesicle topography*. The Journal of Neuroscience 2002; 22: 1648-16467

Miki T, Kaufmann W A, Malagon G, Gomez L, Tabuchi K, Watanabe M, Shigemoto R, Marty A. *Numbers of presynaptic Ca2+ channel clusters match those of functionally defined vesicular docking sites in single central synapses*. Proceedings of the National Academy of Sciences 2017; 114: E5246-E5255

Milovanovic D, De Camilli P. *Synaptic Vesicle Clusters at Synapses: A Distinct Liquid Phase?* Neuron 2017; 93: 995-1002

Mintz I M, Sabatini B L, Regehr W G. *Calcium Control of Transmitter Release at a Cerebellar Synapse*. Neuron 1995; 15: 675-688

Mintz I M, Venema V J, Swiderek K M, Lee T D, Bean B P, Adams M E. *P-type calcium channels blocked by the spider toxin omega-Aga-IVA*. Nature 1992; 355: 827-829

Mittelstaedt T, Alvarez-Baron E, Schoch S. *RIM proteins and their role in synapse function*. Biological Chemistry 2010; 391: 599-606

Mochida S, Few A P, Scheuer T, Catterall W A. *Regulation of Presynaptic Cav2.1 Channels by Ca2+ Sensor Proteins Mediates Short-Term Synaptic Plasticity*. Neuron 2008; 57: 210-216

Müller M, Yin Liu K S, Sigrist S J, Davis G W. *RIM Controls Homeostatic Plasticity through Modulation of the Readily-Releasable Vesicle Pool*. The Journal of Neuroscience 2012; 32: 16574-16585

Neher E, Sakaba T. *Combining Deconvolution and Noise Analysis for the Estimation of Transmitter Release Rates at the Calyx of Held*. The Journal of Neuroscience 2001; 21

Nicoll R A, Schmitz D. *Synaptic plasticity at hippocampal mossy fibre synapses*. Nature Review Neuroscience 2005; 6: 863-876

Palay S L, Palade G E. *The fine structure of neurons*. Public Health 1955; 1

Picher M M, Opris A-m, Martina M. *Rab Interacting Molecules 2 and 3 Directly Interact with the Pore-Forming CaV1.3 Ca2+ Channel Subunit and Promote Its Membrane Expression*. Frontiers Cell Neuroscience 2017; 11: 1-11

Powell C M, Schoch S, Monteggia L, Barrot M, Matos M F, Feldmann N, Sudhof T C, Nestler E J. *The presynaptic active zone protein RIM1alpha is critical for normal learning and memory*. Neuron 2004; 42: 143-153

Qian J, Noebels J L. *Presynaptic Ca2+ influx at a mouse central synapse with Ca2+ channel subunit mutations*. The Journal of Neuroscience 2000; 20: 163-170

Ramón y Cajal S. *Sobre las fibras nerviosas de la capa molecular del cerebelo*. Revista trimestral de Histología Normal y Patológica 1888: 32-63

Ramón y Cajal S. *Textura del sistema nervioso del hombre y de los vertebrados*. Revista trimestral de Histología Normal y Patológica 1899; 35: 1-20

Reid C A, Bekkers J M, Clements J D. *N- and P/Q-type Ca2+ channels mediate transmitter release with a similar cooperativity at rat hippocampal autapses*. The Journal of Neuroscience 1998; 18: 2849-2855

Reuter H. *Calcium channel modulation by neurotransmitters, enzymes and drugs*. Nature 1983; 301: 569-574

Ricci-Tersenghi F, Minneci F, Sola E, Cherubini E, Maggi L. *Multivesicular release at developing Schaffer collateral-CA1 synapses: an analytic approach to describe experimental data*. Journal of Neurophysiology 2006; 96: 15-26

Rosenmund C, Clements J D, Westbrook G L. *Nonuniform probability of glutamate release at a hippocampal synapse*. Science 1993; 262: 754-757

Schikorski T, Stevens C F. *Quantitative Ultrastructural Analysis of Hippocampal Excitatory Synapses*. The Journal of Neuroscience 1997; 17: 5858-5867

Schneggenburger R, Neher E. *Intracellular calcium dependence of transmitter release rates at a fast central synapse*. Nature 2000; 406: 889-893

Schoch S, Castillo P E, Jo T, Mukherjee K, Geppert M, Wang Y, Schmitz F, Malenka R C, Südhof T C. *RIM1α forms a protein scaffold for regulating neurotransmitter release at the active zone*. Nature 2002; 415: 321-326

Schoch S, Mittelstaedt T, Kaeser P S, Padgett D, Feldmann N, Chevaleyre V, Castillo P E, Hammer R E, Han W, Schmitz F, Lin W, Südhof T C. *Redundant functions of RIM1alpha and RIM2alpha in Ca2+-triggered neurotransmitter release*. The EMBO journal 2006; 25: 5852-5863

Scimemi A, Diamond J S. *The number and organization of Ca2+ channels in the active zone shapes neurotransmitter release from Schaffer collateral synapses*. The Journal of Neuroscience 2012; 32: 18157-18176

Serra-Pages C, Medley Q G, Tang M, Hart A, Streuli M. *Liprins, a family of LAR transmembrane protein-tyrosine phosphatase-interacting proteins*. Journal of Biological Chemistry 1998; 273: 15611-15620

Simsek-Duran F, Linden D J, Lonart G. *Adapter protein 14-3-3 is required for a presynaptic form of LTP in the cerebellum*. Nature Neuroscience 2004; 7: 1296-1298

Su S C, Seo J, Pan J Q, Samuels B A, Rudenko A, Ericsson M, Neve R L, Yue D T, Tsai L H. *Regulation of N-type Voltage-Gated Calcium Channels and Presynaptic Function by Cyclin-Dependent Kinase 5*. Neuron 2012; 75: 675-687

Südhof T C. *The presynaptic active zone*. Neuron 2012; 75: 11-25

Südhof T C. *A molecular machine for neurotransmitter release: synaptotagmin and beyond*. Nature Medicine 2013; 19: 1227-1231

Takahashi T, Momiyama A. *Different types of calcium channels mediate central synaptic transmission*. Nature 1993; 366: 156-158

Thomson A M. *Facilitation, augmentation and potentiation at central synapses*. Trends Neuroscience 2000; 23: 305-312

Turrigiano G G, Nelson S B. *Homeostatic plasticity in the developing nervous system*. Nature Review Neuroscience 2004; 5: 97-107

Uriu Y, Kiyonaka S, Miki T, Yagi M, Akiyama S, Mori E, Nakao A, Beedle A M, Campbell K P, Wakamori M, Mori Y. *Rab3-interacting molecule gamma isoforms lacking the Rab3-binding domain induce long lasting currents but block neurotransmitter vesicle anchoring in voltage-dependent P/Q-type Ca2+ channels*. The Journal of biological chemistry 2010; 285: 21750-21767

Van der Kloot W. *Estimating the timing of quantal releases during end-plate currents at the frog neuromuscular junction*. The Journal of Physiology 1988; 402: 595-603

Wang Y, Okamoto M, Schmitz F, Hofmann K, Südhof T C. *Rim is a putative Rab3 effector in regulating synaptic-vesicle fusion*. Nature 1997; 388: 593-598

Wang Y, Südhof T C. *Genomic definition of RIM proteins: Evolutionary amplification of a family of synaptic regulatory proteins*. Genomics 2002; 81: 126-137

Wang Y, Sugita S, Südhof T C. *The RIM/NIM family of neuronal C2domain proteins: Interactions with Rab3 and a new class of Src homology 3 domain proteins*. Journal of Biological Chemistry 2000; 275: 20033-20044

Wheeler D, Randall A, Tsien R. *Roles of N-type and Q-type Ca2+ channels in supporting hippocampal synaptic transmission*. Science 1994;

Wu L G, Saggau P. *Pharmacological identification of two types of presynaptic voltage-dependent calcium channels at CA3-CA1 synapses of the hippocampus*. The Journal of Neuroscience 1994; 14: 5613-5622

Wu L G, Westenbroek R E, Borst J G, Catterall W a, Sakmann B. *Calcium channel types with distinct presynaptic localization couple differentially to transmitter release in single calyx-type synapses*. The Journal of Neuroscience 1999; 19: 726-736

Xu J, Mashimo T, Sudhof T C. *Synaptotagmin-1, -2, and -9: Ca2+ sensors for fast release that specify distinct presynaptic properties in subsets of neurons*. Neuron 2007; 54: 567-581

Zhao M, Hollingworth S, Baylor S M. *Properties of tri- and tetracarboxylate Ca2+indicators in frog skeletal muscle fibers*. Biophysical Journal 1996; 70: 896-916

Zürner M, Mittelstaedt T, tom Dieck S, Becker A, Schoch S. *Analyses of the spatiotemporal expression and subcellular localization of liprin-α proteins*. Journal of Comparative Neurology 2011; 519: 3019-3039

8 Acknowledgement

I would like to extend great gratitude towards my supervisors Prof. Dirk Dietrich and Prof. Susanne Schoch for the constant guidance, support, and encouragement. Thank you for the interesting discussions and advice, which gave me the opportunity for continuously learning.

I especially would like to thank my second supervisor Prof. Maria Luz Montesinos for her invaluable and selfless collaboration. Thank you for showing me that there are many different ways of being a great scientist.

I cordially thank Prof. Christian Henneberger for kindly agreeing to be part of my PhD committee thesis.

Finally, I would like to thank everyone in the lab, past and present members, for helping me grow as a scientist, but even more importantly, as a person.

And to the rest of the people I am thankful to (many…!), I will tell them with spoken words and beer in hand. There are not enough pages in any thesis to express my most sincere gratitude to them.